Experimental Investigation of Particle Lag behind a Shock Wave using a Novel Laser Doppler Accelerometer

Tobias Ecker

Thesis submitted to the Faculty of the
Virginia Polytechnic Institute and State University
in partial fulfillment of the requirements for the degree of

Master of Science
in
Aerospace Engineering

Roger L. Simpson, Chair
Joseph A. Schetz
Pavlos P. Vlachos
Kevin T. Lowe

August 3, 2011
Blacksburg, Virginia

Keywords: Multiphase Flow, Particle Drag, Laser Doppler, Supersonic, Slip Flow, Non-Continuum Flow

Experimental Investigation of Particle Lag behind a Shock Wave using a Novel Laser Doppler Accelerometer

Tobias Ecker

(Abstract)

Determination of particle slip is a major concern for particle based measurements in unheated supersonic facilities, as it is a limiting factor for the instruments' frequency response. For the purpose of determining the particle deceleration through a stationary shock wave in a super sonic windtunnel, a novel 1-D Laser Doppler probe with an unique spatial range (~1.5 mm) is presented. The study first gives a short review of the physics of particle motion with respect to different drag models and flow regime encountered in super sonic flows. In the second part, the focus lies on the development of a new Laser Doppler probe using non Gaussian beams to obtain a prolonged measurement volume. This volume covers a major part of the particle lag after a shock wave. An experimental investigation on particle acceleration and drag, using different types and sizes of seeding material, including standardized microspheres is carried out in the $M_\infty = 2.0$ super sonic facility. Three different types of particles with four different sizes are experimentally investigated. The experimental data provides mean velocity as a function of distance from the shock and reveals significant agglomeration and evaporation problems with Titanium Oxide and Polystyrene Latex spheres. Particle acceleration measurements are presented, proving the unique concept of the new Laser Doppler probe. Mean and instantaneous acceleration data is extracted from high SNR signals. The acceleration data obtained is consistent in magnitude and trend with the physical phenomena expected and shows the feasibility of the new instrument.

Acknowledgements

I would like to thank everybody who helped, pushed and contributed to the successful outcome of my Masters thesis. I would like to acknowledge my advisor Dr. Simpson for the guidance he constantly provided throughout my research. Also my other committee members, Dr. Lowe, Dr. Vlachos and Dr. Schetz gave priceless advice and contributed in many ways to my development as a researcher. I would like to acknowledge the help of Dr. Byun who kept me sane in my windtunnel experiments. Also I would like to thank the researchers and staff at NASA Langley and NASA Ames, especially Ms. Tiemsen, Mr. Bartram, Dr. Meyers and Dr. Brown for the help and experience they supplied.

I would like to thank Dr. Simon and Dr. Will at my undergraduate university who encouraged me early on and supported me through my Fulbright journey and beyond. I would like to acknowledge the support by the Fulbright Commission and express the gratitude for the existence of such a wonderful program, the opportunities it provides and the higher goal it serves. It was an invaluable experience and will imprint me forever.

Finally I would like to thank my family and friends, the ones far away and the ones really close for their love and support that gave me the strength to pull through and succeed.

Contents

List of Figures

List of Tables

Nomenclature

The nomenclature for this thesis is given in the list below. As far as possible it was tried to use different symbols for different parameters and functions trough the work while abiding to the established nomenclature. If not given below, changes will be adressed in the context of its use.

Roman Symbols

A	Magnitude
a	Schlieren image height
b	beam vector
C	characteristic frequency of the particle motion
C_D	drag coefficent
D	steepness of the shock
d	diameter
d_{fr}	fringe spacing
$E(\omega)$	energy spectral density
f	fringe vector
f	non dimensional turbulence frequency
f_D	Doppler frequency
Gr	Grashof number
i	index
K	Gladstone-Dale constant
Kn	Knudsen number
L	characterstic length
M	Mach number
m	mass
N_{fr}	number of fringes
Pr	Prandtl number
R	general gas constant
Re	Reynolds number
S	molecular speed ratio
s	ratio of particle to fluid density
s(t)	Signal
T	temperature
t	time
u	velocity
x	tunnel coordiante parallel to the flow direction
y	vertical streamwise tunnel coordinate
z	horizontal streamwise tunnel coordinate
z(t)	Complex signal

Abbreviations

LDA	Laser Doppler Anemometry
LDV	Laser Doppler Velocimetry
LTA	Laser Transit Anemometry
NA	Information not available
PIV	Particle Image Velocimetry
SNR	Signal to Noise Ratio
SNR_{dB1}	Alternative Signal to Noise Ratio in dB
SNR_{dB}	Signal to Noise Ratio in dB

Greek Symbols

β	shock angle
Δ	total uncertainty
δ	uncertainity of a single parameter
γ	ratio of specific heat
κ	isentropic coefficient
λ	mean free path
λ_b	wave length of the beam
μ	dynamic viscosity
ω	$(= 2\pi f)$ turbulence frequency

ω_c	highest turbulence Eigenfrequency of interest
ρ	density
σ^2	variance
τ	time constant
θ	intersection angle
ξ	coordinate of the trajectories of the light

Sub and Superscripts

∞	reference
*	dimensionless
$_f$	fluid
$_p$	particle
$_r$	relative value
n	noise
sig	signal

Mathematical Symbols/Operators

$\mathcal{H}$	Hilbert transform
J	Fisher Information matrix
p(x,a)	joint probability density function

Preface

The seeding or particle generation for Laser Doppler or Particle Image Velocimetry was, when I arrived at Virginia Tech in 2009, a topic I was a only slightly aware of, if at all. Many thesis's, dissertations, journal articles and conference presentations do not spend more than a short paragraph on this topic and most people not working in the area are unaware that the optical "nonintrusive" Laser based measurement is intrusive in so far, as that tracer particles are introduced into the flow, changing the fluid's properties. This is especially true for air where common tracer particles usually have a specific gravity two orders of magnitude higher than the surrounding gas. For compressible flows with typically low temperatures the interesting aspect of non continuum flows is added.

I spend the major part of my first year reading and inquiring about the topic of seeding and experienced its challenges first hand when I accompanied the first LDV measurements by Dr. Beyun and Dr. Lowe in the super sonic facility at Virginia Tech. This is also a main reason why I decided to not banish my review of windtunnel seeding methods in the Appendix, as it is important to understand the limitations they impose on the experimental process at hand. In the first part of my second year, Dr. Simpson and I decided on an experimental investigation on particle lag which completes the work I have done to a whole. My primary work has thus been in the analysis of high speed particle motion, the generation of flow tracer particles and the experimental investigation of their flow following properties. These topics are the core and the central theme around which this thesis has been constructed. The task of preparing this thesis has thus been to extract from these activities a coherent body of work.

1 Introduction

The motivation of this work is a coherent study on particle lag in non continuum flows. For this purpose a comprehensive and fundamental review on particle drag in continuum and non continuum flows was undertaken, including numerical application for particle lag behind a shock wave. An extensive review on windtunnel seeding interconnects this theoretical part with the real world problem of windtunnel application and gives valuable references for PIV and LDV users. To conclude the study a novel 1 component Laser Doppler probe with unique spatial resolution and extend was designed and fabricated. This system was then used in particle lag experiments in a M=2.0 windtunnel. Additionally, estimation uncertainties were analyzed using a nonlinear chirped model signal.

New data from this study will allow researchers to improve particle drag predictions, enable the analysis of the flow tracking capabilities of particles for LDV or PIV measurements in shock-dominated supersonic flows, and provide a means for *in situ* measurements of particle size in flow experiments containing shocks.

This work is not only centered in the evaluation of uncertainties of particle based measurement methods, but also offers the possibility of measuring various flows often encountered in industrial applications. Especially flows with a strong one dimensional character, like sprays, dense sprays, channel and pipe flows with big velocity gradients are predestined for application.

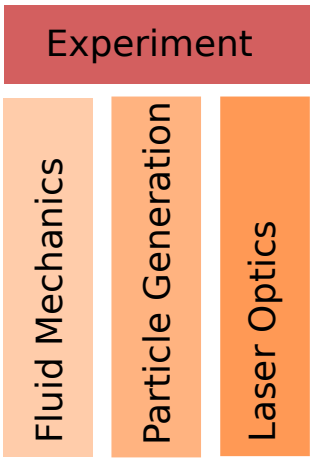

Figure 1: Structure

This thesis is split into four major parts. In the first part (chapter 2) the high speed particulate flows, particle drag and related flow analysis analysis are summarized, and simple results and pre-calculations of particle movement through shock waves are presented. The

second part (chapter 3) reviews common windtunnel seeding approaches in detail and tries to give helpful data-basis for seeding selection and application for particle based laser measurements. The third part (chapter 4) explores the foundations of Laser Doppler Accelerometry, a relatively new LDV variant applied to the problem of high speed particulate flows. The uncertainties of this kind of measurement method as well as model signals characteristic for the experiment are covered in order to give a foundation to understand the experimental difficulties arising from the novel probe and its spatial range. In the last part (chapter 5 and chapter 6) the instrumentation, the experimental facilities, the instrument calibration and the main experiments are described and the experimental data is compared to analytical models.

1.1 Related Experimental Work

Several related measurement methods and experimental setups that can be used to measure particle drag exist and are reviewed here in short. Many combinations and derivatives of these approaches are used in science and can be found in literature. A short overview, methodically split up is given here:

Rapid camera shadowgraphy (e.g. Devals et al. [25]) or **double exposure holography** (e.g. Igra and Takayama [45]) in shock tubes can be used to determine drag coefficients indirectly from the particle trajectory for high relative Reynolds number flows. Usually a particle is injected or held in place by a very fine support structure and then moved by a shock wave. Steady effects can be observed while the initial shock accelerates the particle, whereas unsteady phenomena are present when the shock reflects at the tube end. The experiment in a shock tube typically results in very high relative Reynolds numbers of the order of 500 to 50,000 and relative Mach numbers in transonic and supersonic ranges [25]. Therefore this experiment is typically used for continuum and slip flows.

Laser Based particle measurement methods are widely used in industry and academic research applications. **Particle Image Velocimetry (PIV)** and **Particle Tracking Velocimetry (PTV)** allow determination of acceleration and particle sizes from a series of images. Correlation based PIV splits the measurement volume in interrogation spots to allow correlation based analysis of the average particle displacement, which makes the method more robust and improves the signal to noise ratio compared to the particle tracking approach. Uncertainties may arise from diffraction [77] and out of plane measurement location. Therefore the particle sizes are not determined from

the recorded images but usually from an additional experimental setup or from light scattering correlations. Measurements in high speed windtunnels make high demands of the instrumentation used, especially to the speed of the CCD cameras [80]. **Phase Doppler Velocimetry (PDV)** is a laser Doppler technique that allows the determination of particle sizes by a temporal correlation of two signals (phase Doppler or time shift technique). A basic condition for this measurement method is that the particles are of a significantly larger dimension than the laser wavelength [4]. Onofri et al. [73] introduced a Phase Doppler technique that allows simultaneous measurement of refractive index, absorption coefficient, particle size and velocity. They reported good agreement for particle sizes above 50 μm. Similarly **Laser Doppler Velocimetry (LDV)** has been used in supersonic facilities to estimate relaxation time constant and drag coefficients by spatial velocity measurements across an oblique shock wave [94, 95]. These measurements were intended to determine if the particles used for the measurement setup are significantly small enough to follow the flow and to estimate the Stokes equivalent particle size by applying Stokes' drag [83, 14, 15].

Force measurements in wind tunnels, tow tanks, aeroballistic ranges [7], of aircraft mounted spheres or in the form of a free fall/settling experiment [40, 64], were mostly performed until the late 1970s for continuum and free molecule flows. Bailey [6] gives a good overview of force measurements and tries to reevaluate and compare the experimental data derived from such measurements. From this study he assembled a new standard drag curve, taking into account uncertainties affecting the drag data basis. As this study showed it is always of concern to estimate the influence of supporting structures and measurement methods by performing additional experiments to determine such bias (e.g.. Wegener and Ashkenas [105] or Vlajinac and Covert [101]).

2 High Speed Particle Motion

Determination of the particle's response to the flow field is a very important matter for many applications, be it for analytical solutions, computational fluid dynamics or for selecting the right particles for optical measurement in experimental fluid mechanics. Some excellent publications in this field giving a structured approach to the behavior of particles are the review paper by Melling[66], a paper focusing on high speed applications by Tedeschi et al. [95] as well as a recent paper by Ragni et al. [80] to mention a few. From these reviews it crystallizes that the case of a particle crossing a shock wave is of special interest as it is a well researched flow phenomena and easy to describe as a discontinuity in the flow field. Especially Ragni et al. [80] continued the work to give a systematic description of tracer particle properties for application in PIV in the test case of an oblique shock wave on the basis of work done by Scarano and van Oudheusden [85].

2.1 Particle Motion

2.1.1 Equations of Motion

The equation for the unsteady motion of a sphere was first derived by Basset. The first two terms in Basset's expression describe the acceleration force and viscous resistance as introduced by Stokes. The pressure gradient due to the acceleration of the sphere is reflected by the third term. The last term, also known as the Basset history integral takes the unsteady effects of the flow field on the sphere into account [66, 39, 68].

$$\rho_p \frac{d_p^3}{6}\frac{du_p}{dt} = -3\mu d_p(u_p - u_v) + \rho_f \frac{\pi d_p^3}{6}\frac{du_f}{dt} - \rho\frac{\pi d_p^3}{12}\frac{d(u_p - u_v)}{dt} - \frac{3}{2}d_p^2(\pi\mu\rho_f)^{\frac{1}{2}}\int_{t_0}^{t}\frac{d(u_p - u_v)}{d\xi}\frac{d\xi}{(t-\xi)^{\frac{1}{2}}} \quad (2.1)$$

It follows that, neglecting lift and buoyancy forces, the movement of a particle in a fluid, assuming high particle to fluid density ratio can be described by the following approximate equation.

$$\frac{du_p}{dt} = \frac{3}{4}\frac{C_D Re_r \mu}{\varrho_p d_p^2}(u_f - u_p) \quad (2.2)$$

The relative Reynolds number is defined as follows:

$$Re_r = \frac{((u_f - u_p)\varrho_f L)}{\mu} \tag{2.3}$$

The influential parameters are the drag coefficient, a characteristic length, the fluid density as well as the viscosity of the carrier fluid and the relative Reynolds number with respect to the particle diameter. The fluid forces exerted on the sphere, typically called drag, result from a combination of pressure distribution, normal shear forces and skin friction [8, 6] and dependent on the evolution of the boundary layer along the surface of the sphere and its possible separation [6]. Because of this, the drag forces are dependent on the flow conditions around the particle and change with the local Reynolds number. The drag suddenly decreases when the flow around the sphere changes from laminar to turbulent at a Reynolds number of around 10^5 [6]. To simplify the problem most analytical and semi-empirical models assume the particle to be a non distorted rigid sphere, however drag models for non spherical particles exist in literature [40].

Typically the diameter is used for the characteristic length, but sometimes for Reynolds numbers above unity expressions involving the boundary layer thickness are employed [95]. In the case of free molecule flow, no boundary layer in the classical sense exists, therefore the diameter is used as the characteristic length.

From the equation of motion, a characteristic frequency of the particle [66] C can be defined. The inverse of C is also known as the particle relaxation time constant τ_p.

$$C = \frac{3}{4} C_d Re_r \frac{\mu}{\rho_p d_p^2} \tag{2.4}$$

2.1.2 Flow Regimes

The relative Mach number is a dimensionless number used to determine if there are significant compressible effects influencing the particle's motion. It is defined as the difference between the Mach number based on the particle velocity and the fluid Mach number:

$$M_r = M_p - M_f \tag{2.5}$$

Another problem especially in high speed flow for very small particles is the validity of the continuity assumption which is dependent on the Knudsen number. The Knudsen number is defined as the ratio of the molecular mean free path to the characteristic length.

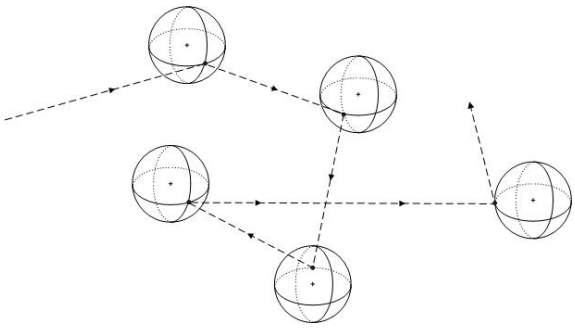

Figure 2: Mean free path between collisions

$$Kn = \frac{\lambda}{L} \tag{2.6}$$

The molecular mean free path is defined as the distance molecules travel between collisions.

$$\lambda = \frac{\mu}{\varrho_f}\sqrt{\frac{\pi}{2RT}} \tag{2.7}$$

From these definitions the interconnection between the relative Reynolds number, the Knudsen number and the relative Mach number can be seen:

$$Re_r = \frac{M_r}{Kn}\sqrt{\frac{\kappa\pi}{2}} \tag{2.8}$$

Tedeschi et al. [95], Crowe et al. [18] and Michaelides [16] give a systematic distinction into four main regions, summarized in table 1.

$0 < \mathrm{Kn} \leq 0.001$ and $M_r < 0.1Re_r^{1/2}$	**Continuum Flow**
$0.001 < \mathrm{Kn} < 0.25$ and $0.01\ Re_r^{1/2} < M_r < 0.1Re_r^{1/2}$	**Slip Flow**
$0.25 < \mathrm{Kn} < 10$ and $0.1Re_r^{1/2} < M_r < 3Re_r$	**Transition flow**
$\mathrm{Kn} \geq 10$ and $M_r > 3Re_r$	**Free molecule flow**

Table 1: Flow regimes

Continuum flow is present if the properties of the flow field can be obtained by analytical or numerical solution of the Navier-Stokes equations, independently of variation in length scale. Therefore single molecule movement is negligible. This is the fundamental condition for performing CFD calculations. Slip flow is a regime in which, because of rarefaction effects, the no slip condition on the particle surface is no longer valid. In this case, a slip velocity between the particle surface and the surrounding molecules of the carrier fluid is present and has to be accounted for. Transition flow classifies a flow region in which the molecular mean

free path is of about the same order as the diameter of the particle. Free molecule flow is present if there are no interactions among the molecules and flow is dominated by collisions of single molecules with particles.

2.1.3 Drag Equations

In order to model the particle trajectory, the drag coefficient needs to be determined. Various models exist for different flow regimes and some selected ones are reviewed here in short.

For Re$\ll$1 Stokes equation (eq. 2.9) for the drag coefficient can be used. The equation of motion (eq. 2.2) then is only dependent on constant parameters, the fluid viscosity, the particle density, the relative velocity and the particle diameter as the most dominant term.

$$C_D = \frac{24}{Re_r} \tag{2.9}$$

Schiller and Naumann (here quoted from Tedeschi et al. [95]) found a different expression valid for a larger range of relative particle Reynolds numbers ($1 \leq Re_r \leq 800$ and $M_r \leq 0.25$), which, for very small Re numbers simplifies to the Stokes expression.

$$C_D = \frac{24}{Re_r}(1 + 0.15Re_R)^{0.687} \tag{2.10}$$

As Tedeschi and other authors point out, Stokes' expression, as well as the expressions [95] developed by Oseen (Re<1), Proudman and Pearson (Re<0.7) and the expression proposed by Schiller and Naumann (Re=<800, M=<0.25) are only of limited use for high speed flows when non-continuum effects are present [95] .

For the case of slip flow, as it occurs in supersonic windtunnels due to rising Knudsen numbers, Cunningham [19] proposed a correction factor of the Stokes drag law to account for slip on the particle surface, valid for very low relative Reynolds number flows. In its general form it is written as follows:

$$C_D = \frac{24}{Re_r}K \tag{2.11}$$

A proposed correction factor ($Re_r \ll 1$ and $M_r \ll 1$) is:

$$K = \left(1 + \frac{9}{2}Kn\right)^{-1} \tag{2.12}$$

Depending on the magnitude of the Knudsen number, the correction factor can be a constant for small Kn numbers or a nonlinear function for large Kn numbers. Jennings [47] gives an overview of new proposed calculations of the Cunningham slip correction factors. The equa-

tions and parameters used are dependent on the boundary conditions and not freely available for all conditions encountered in a wind tunnel environment, especially with pressure and temperature changes as present in compressible flow applications. Kim et al.[53] give some more insight about the development of the slip factor, especially over a long range of Kn numbers directly applicable to Polystyrene Latex spheres.

Henderson [37] in 1976 presented a correlation equation valid for all subsonic and another equation specific for all supersonic flow regimes. The expression for all subsonic regimes (M<1) , incorporating corrections and fitting for subsonic continuum flow, subsonic slip and transition flow – both incompressible and compressible, is as follows and described in detail in the author's initial publication:

$$C_D = 24\left[Re_r + S\left\{4.33 + \left(\frac{3.65 - 1.53\frac{T_w}{T}}{1 + 0.353\frac{T_w}{T}}\right)e^{-0.247\frac{Re_r}{S}}\right\}\right]^{-1} + e^{-0.5\frac{M_r}{\sqrt{Re_r}}}\left[\frac{4.5 + 0.38(0.03Re_r + 0.48\sqrt{Re_r})}{1 + 0.03Re_r + 0.48\sqrt{Re_r}} + 0.1M_r^2 + 0.2M_r^8\right] + 0.6S\left[1 - e^{\frac{M_r}{Re_r}}\right] \quad (2.13)$$

Here S is the the molecular speed ratio and defined as:

$$S = \frac{u_f - u_p}{\sqrt{2RT}} = \sqrt{\frac{\kappa}{2}}M_r \quad (2.14)$$

For relative Mach numbers greater than 1.75 Henderson gives another expression. Also, the region between the subsonic expression and the supersonic expression is covered by a linear interpolation equation and can be found in the original paper.

In a comparable recent development Tedeschi et al. [95, 94] developed a more analytical expression[1] for a multi regime drag equation ($Re_r \lesssim 200$ and $M_r \lesssim 1$).

$$C_D = \frac{24}{Re_p}K(1 + 0.15(KRe)^{0.687})\xi(Kn) \quad (2.15)$$

where

$$\xi(Kn) = 1.177 + 0.177\frac{0.851Kn^{116} - 1}{0.851Kn^{1.16} + 1}$$

For $Re_p \lesssim 1$, $Kn \lesssim 10$ and $M_p \lesssim 0.25$ Tedeschi gives a simplified expression:

[1] here shown without correction for compressibility

$$C_D = \frac{24}{Re_p} K\xi(Kn) \tag{2.16}$$

Other drag models for multi flow regime calculations proposed by Walsh [102, 103] and Crowe et al.[17, 16] [2]. All these popular models are valid for steady state drag and are usually used with the steady state term of the Basset equation but do not any history or unsteady effects. Michaelides [68] gives a good review of hydrodynamic forces and heat transfer effects including the history terms in his Freeman Scholar lecture. For very high particle Reynolds numbers, Igra and Takayama [45] report a significant contribution of flow dynamics to the drag coefficient compared to steady state flows. For application in supersonic windtunnels this is only of importance if the particles are injected in the supersonic part, whereas the relative Reynolds numbers of particles injected downstream in the subsonic part of the nozzle are the highest when they move through a shock. The Reynolds number in the present case for seeding particles usually lays below 20. For shock-tubes where high Reynolds numbers can be reached Devals et al. [25] show a comparison of some drag models with experimental data.

For rarefied particulate flows (Kn $\geq$ 10 and $M_r > 3Re_r$), Patterson, Schaaf and Chambre [86] as well as Tedeschi [95] give expressions for the drag coefficient. These expressions stem in part from kinematic theory and incorporate moment accommodation coefficients around 0.9-0.95 to account for semi-elastic molecule and particle collisions[3] . These expressions have more applications for rocket propulsion and satellite trajectory design than for wind tunnel flows.

2.2 Analysis of Particle Response to Instantaneous Deceleration through a Shock - Simplified Modeling

As Melling [66], Tedeschi et al. [95], Ragni et al. [80] and other authors have concluded, the movement of a particle through a shock wave is an excellent way to analyze its flow following capabilities. The shock wave as a discontinuity is well studied and for practical applications, the one dimensional relationships as given by the Hugoniot equations [92] are sufficient to describe the flow field. Mathematically, for the case of a steady shock, it can be approximately described as a step function. Since the particles are more inert and about three

[2] for application in combustive rocket nozzle flows

[3] The accommodation coefficient is 0 if all energy would be lost by a collision, and 1.0 if all energy would be conserved.

times an order of magnitude bigger than fluid molecules[4] it will take a certain time/distance after the shock until the particles reach terminal velocity (Figure 3).

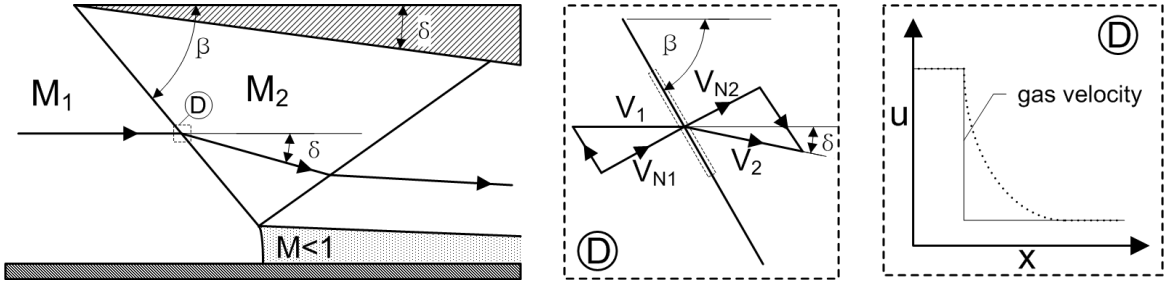

(a) Schematic of oblique shock with reflection and boundary layer separation

(b) Detail of velocity components at the oblique shock

(c) Detail of particle velocity through the shock

Figure 3: Schematic of shock generation

2.2.1 Supersonic Flow and Oblique Shock Wave

The flow conditions after the shock can be obtained by the isentropic oblique shock wave relations (Hugoniot equations). The ones important for the geometric relations of the shock wave and reflection are listed below and can be found in the NACA report 1135 [92] or in any other textbook covering compressible flow.

The nonlinear relationship between deflection angle and shock angle based on upstream Mach number and specific heat ratio is given as an implicit equation and can only be solved iteratively. Strong and weak shock solutions exist to this equation, but usually the weak shock solution is dominant in technical application and nature. Figure 4 plots the nonlinear relationship between deflection and shock angle and also shows weak and strong solutions.

$$tan^2(\delta) = \frac{2\,cot(\beta_1)\,(M_1^2 sin^2(\beta) - 1)}{(2 + M_1^2(\gamma + cos(2\,\beta_1))} \tag{2.17}$$

[4] e.g air molecules have an average diameter of $9.69 * 10^{-10} m$ [60]

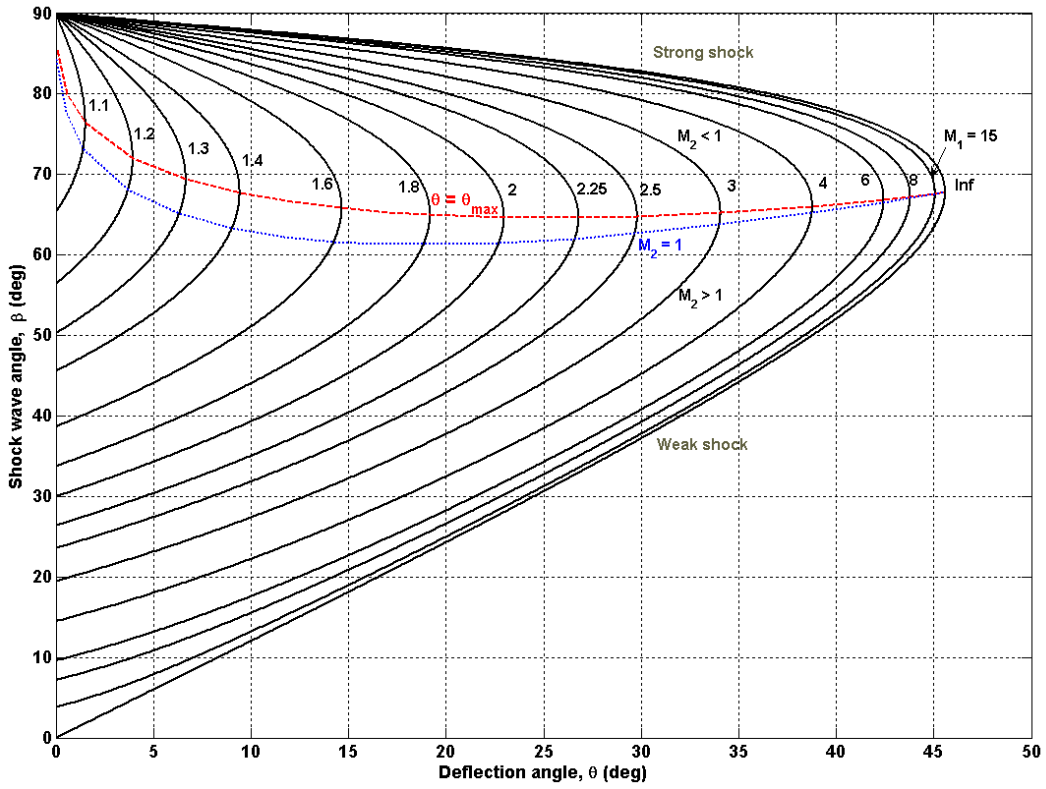

Figure 4: Relationship between shock and deflection angle (free use, [2])

The Mach number of the flow normal to the shock wave can be found from the geometrical relationships as displayed in Figure 3b.

$$M_{1n} = M_1 sin(\beta_1)$$

$$M_{2n} = \sqrt{\frac{(M_1^2(\gamma - 1) + 2)}{(2\,\gamma\,M_1^2 - (\gamma - 1))}}$$

$$M_2 = \frac{M_{2n}}{sin(\beta_1 - \delta)}$$

Due to the strong (irreversible) thermodynamic changes across the shock, the change in viscosity needs to be considered. The dynamic viscosity of a gaseous fluid for different temperatures and pressures can either be read from tables or be calculated using an empirical correlation e.g. Sutherland's law [72, 92], which in its dimensionless form is written as:

$$\mu^* = T^{*3/2}\frac{1 + S^*}{T^* + S^*},\ S^* = \frac{110.4K}{T_\infty},\ T^* = \frac{T}{T_\infty},\ \mu^*\frac{\mu}{\mu_\infty} \tag{2.18}$$

Or in its dimensional form more applicable for numerical calculations:

$$\mu = \mu_\infty \left(\frac{T}{T_\infty}\right)^{3/2} \frac{273.15K + 110.4K}{T + 110.4K} \tag{2.19}$$

For air the equation is written as:

$$\mu = 1.716\,10^{-5} \frac{kg}{ms} \left(\frac{T}{273.15K}\right)^{3/2} \frac{273.15K + 110.4K}{T + 110.4K} \tag{2.20}$$

Experiments and calculation performed by Kenney et al. [51] have shown that Sutherland's law, which is an empirical corrected interpolation, is quite accurate for a large range of temperatures. In Figure 5 experimental data from Kenney et al. [51] and Kestin and Whitelaw [52] for atmospheric pressure are compared to results obtained using Sutherland's law.

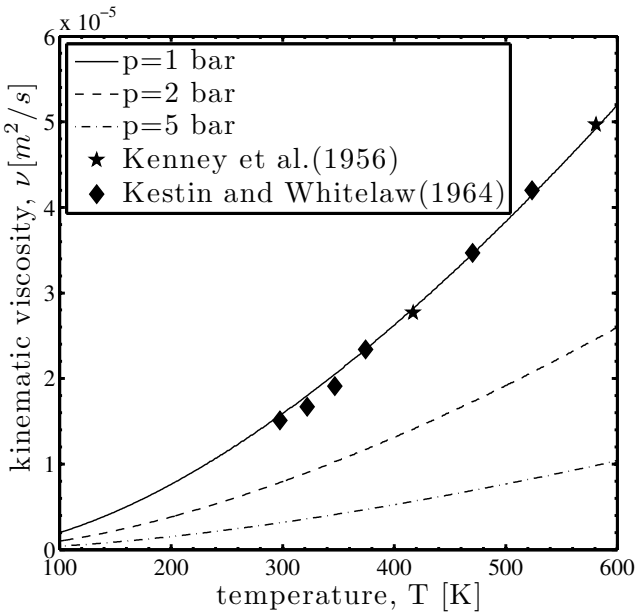

Figure 5: Comparison of Sutherland's law with some experimental data

Beside Sutherland's law, the semi empirical equations of Hirschberger or Chapman and Enskog have also successfully been used to calculate the dynamic viscosity of a gaseous fluid and were also found to represent the change of viscosity over temperature very well. Hirschberger's equation is based on the solution of the Bolzman equation as presented by Chapman and Enskog:

$$\mu = \frac{5\sqrt{\pi\, m\, k_b\, T}}{16\,\pi\,\sigma^2\,\Omega^{2.2*}} \tag{2.21}$$

The shock thickness is usually of the order of magnitude of several mean free path lengths and can be coarsely estimated from some simple mechanics. For this order of magnitude estimate it is assumed a linear velocity profile through the shock and the shear stresses are derived from the normal stresses. Boundary conditions are obtained from isentropic shock relations, even though the shock it self is not isentropic. Details about this derivation can be found in a textbook by Granger [35]. The resulting equation is shown as eq. 2.22.

$$s = \frac{\mu}{\rho_f a_1 M_{1n}} \tag{2.22}$$

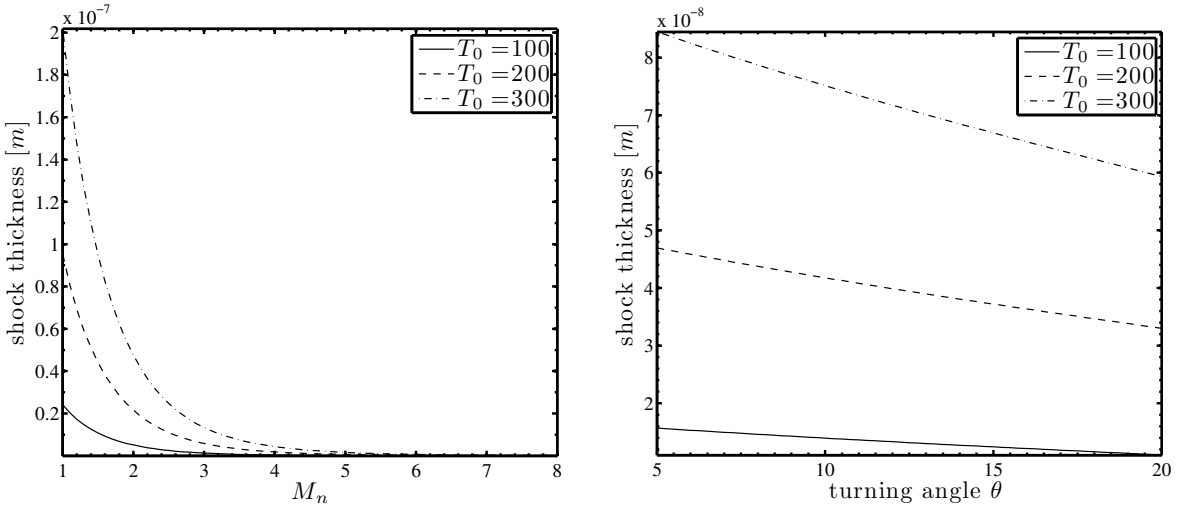

(a) Shock thickness dependent on the normal Mach number

(b) shock thickness for a oblique shock (M=2) in dependence of the turning angle

Figure 6: Shock thickness

Several things can be learned from this simple approximation: the shock thickness is not constant but dependent on the normal Mach number as well as on the initial temperature and pressure conditions. Also it is dependent on the gas properties. As the plot (Figure 6a) shows, the shock thickness reduces with increasing Mach numbers. For the case of an oblique shock, in dependance of the turning angle, an almost linear relationship of turning angle and shock thickness is obtained.

2.2.2 Test Cases

Examples of application of the previously reviewed steady state drag equations are shown for subsonic slip flow and subsonic transition flow cases. These cases are most common

in supersonic wind tunnel facilities and serve as a benchmark. Important flow parameters are summarized in table 2. The Reynolds and Mach numbers given refer to the situation immediately after the shock where they are the highest. Similar calculations have been performed by the authors of the initial publications and were repeated in order to ensure consistency and comparison of several different cases. The change in viscosity was taken into account by the use of Sutherland's law (eq. (2.19)) which is described more in detail in section 2.2.1. Such simple one dimensional calculations are also a valuable approach for determining applicable drag models for more complex numerical simulations [30].

2.2.3 Results

The first two test cases are shown in Figure 7a and Figure 7b. The experimental data was obtained by Chesnakas [14] in a transonic cascade windtunnel for Polystyrene Latex (PSL) spheres. In contrast to measurements using metal particles (e.g TiO_2 or Al_2O_3), where agglomeration is a problem, or any kind of droplet generators, where the droplet sizes depend on many parameters, the sizes of the PSL spheres are well known, assuming the carrier fluid evaporated completely. Since the diameter of the PSL spheres is constant and the gas velocities up- and downstream are known, the drag equations can be used to calculate particle relaxation through the shock. Sabroske [83] measured the relaxation of PSL spheres and compared them to glycerin particles. Scattering of the experimental data complicated the determination of the shock wave position. Therefore a data point shortly before a steep drop in velocity was chosen as the position of the shock wave. However, the trend is clearly visible from the measurements and shown here for completeness (Figure 7c). Case T is based on experimental data by Tedeschi et al. [95] for a subsonic transition flow. Tedeschi used this case for comparison of his proposed model.

No	Case	d[µm]	Re_p	M_p	Kn	Regime
C I	Chesnakas[14]	0.6	3.25	0.1955	0.089	Subsonic slip flow
C II		1.5	8.13	0.1955	0.036	Subsonic slip flow
S	Sabroske[83]	0.8	10	0.216	0.032	Subsonic slip flow
T	Tedeschi [95]	0.523	0.27	0.162	0.89	Subsonic transition flow

(a) Particle parameters

M	δ
2.46	10°
2.46	10°
2.00	10°
2.3	8°

(b) Windtunnel setup parameters

Table 2: Overview of test cases

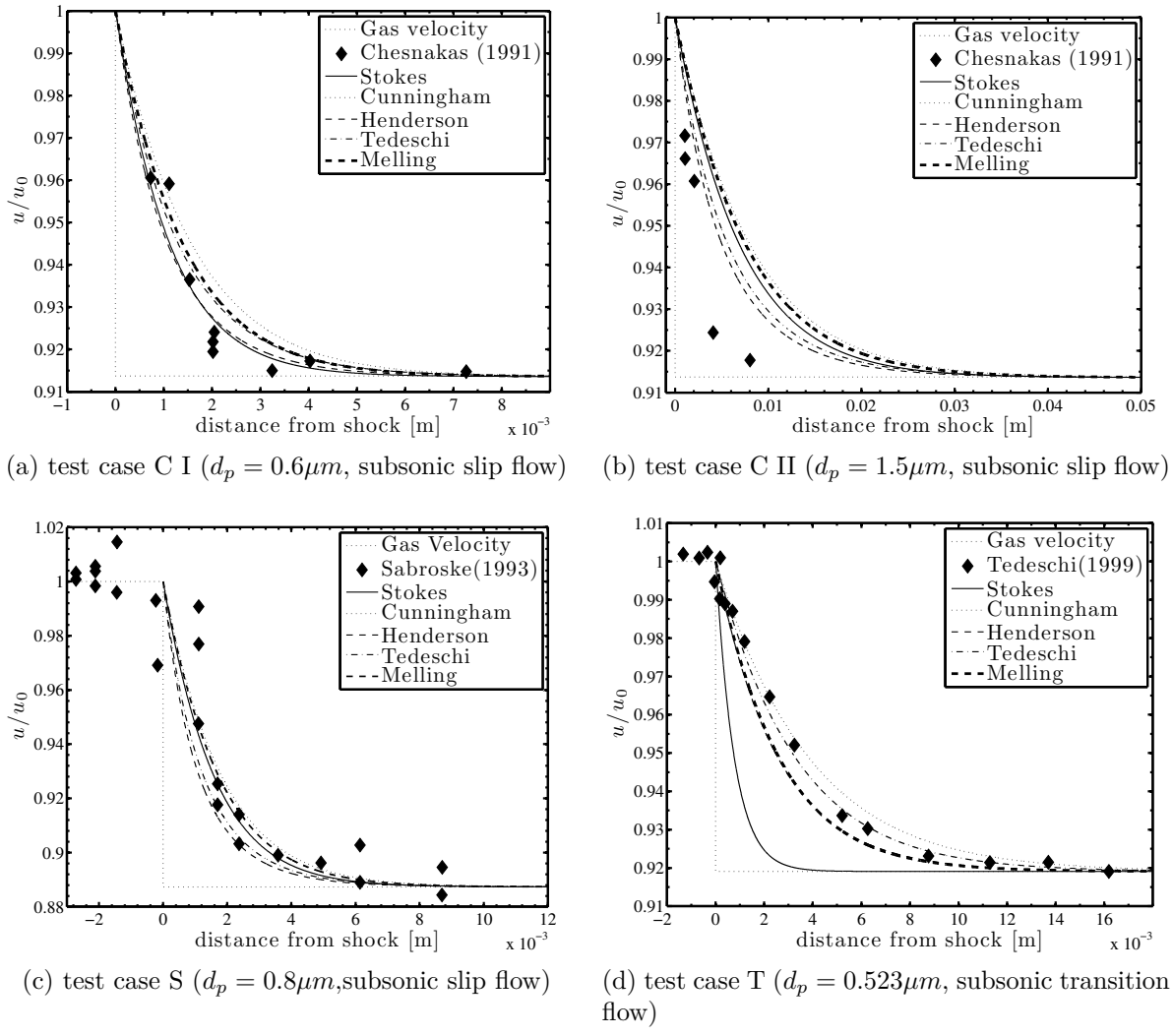

(a) test case C I ($d_p = 0.6\mu m$, subsonic slip flow)

(b) test case C II ($d_p = 1.5\mu m$, subsonic slip flow)

(c) test case S ($d_p = 0.8\mu m$,subsonic slip flow)

(d) test case T ($d_p = 0.523\mu m$, subsonic transition flow)

Figure 7: Calculations of particle movement through an oblique shock using different drag laws

As can be seen in Figures 7a to 7d, it is very complicated to determine which model is best for describing the particle motion across a shock wave. The deviation in data points is very broad so that many models could be sufficient to describe the problem in slip flow, however the Stokes model completely fails in the transition regime (Figure 7d) and is by definition not applicable for any slip flow problems shown since the relative Reynolds number is well above unity. The Henderson model, as well as the Tedeschi model are better suited in describing the particle motion in all regimes, but from Figure 7b is evident that all models seem to fail for large particle sizes.

These observations indicate that more experimental data for this kind of problem are needed.

2.3 Analysis of Particle Response to Instantaneous Deceleration - Computational Fluid Dynamics Modeling

2.3.1 Model and Boundary Conditions

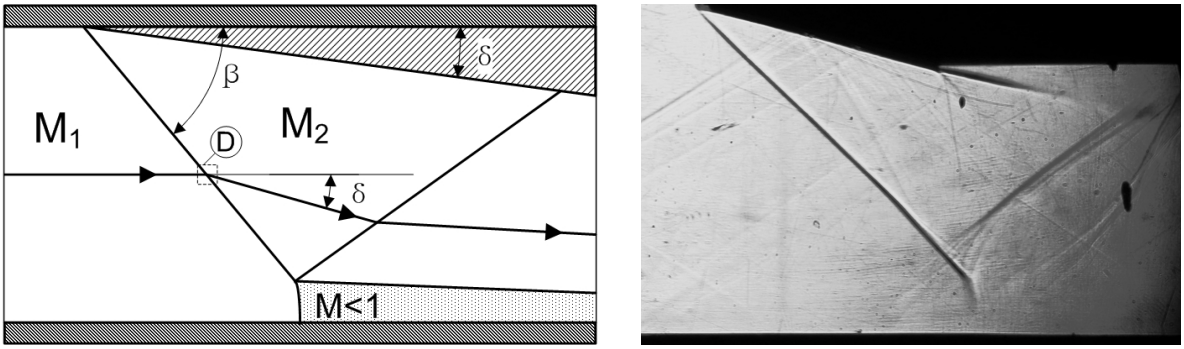

(a) Schematic of particle trajectory through a shock

(b) Schlieren photograph of one half of a shock generator in the SSWT at Virginia Tech

Figure 8: Schematic of the physical problem

The computational investigation was carried out using the commercial Finite Volume solver Fluent 12.1 distributed by Ansys Inc. As this problem involves highly compressible effects with Mach numbers ranging from 2.0 to 2.46, the density based solver was used. Fluent 12.1 offers several models for multiphase problems. These include the Mixture model, the Eulerian model, the Steam model, the Dense Discrete Phase model and the Discrete Phase model. The Steam and Discrete Phase model are the only multiphase models that can be used with a density based solver [3]. Whereas most other models only allow statistical information, the Discrete Phase model allows calculation of explicit particle trajectories - similar to the one dimensional computations shown before. As such the modeling approach can be described as a Euler-Lagrange approach, the flow field is solved as a continuum and unidirectional coupled with the single particles. This means that the statistical information of the flow field are imposed as boundary conditions on the particle trajectory and the flow field is assumed not to be influenced by the particle motion[5]. Taking into account the relatively low particle mass and count (the simulation was carried out with a line of particles) this is a valid assumption. The aim of this study is to investigate the 2D flow and the influence of the velocity profile, which must be very steep but cannot be an exact step function as there are no infinite small shock thicknesses. Due to the supersonic flow there is no upstream information transport [6].

[5] one-way coupling

[6] not considering information transport in the subsonic part of the boundary layer, which has an especially strong influence on the location of the reflected shock

Related validation cases can be found in the NPARC Alliance database for the WIND code as well as in recent literature [34]. Details of the test cases, also previously reviewed in the 1 D investigation can be found in table 2 on page 14.

2.3.2 Grid Independence and Turbulence Modeling

First modeling approaches employed the Spalart Allmaras model, a one equation turbulence model first introduced by Spalart and Allmaras [91] in 1992. Despite its vast usage for aerospace applications, the Spalart Allmaras seems to over-predict the shock thickness and produce an unphysical velocity profile.

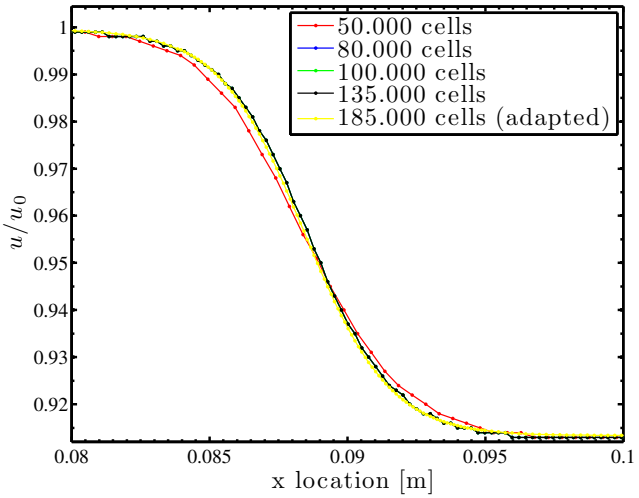

Figure 9: Grid dependence

A grid dependence study (see Figure 9) is carried out in order to rule out grid spacing effects resulting in an enlarged shock thickness. The mesh is adapted by pressure gradient, to refine critical regions around the shock and expansion waves. The resulting final grid is used for all future computations and is shown in Figure 10. All equations are solved with at least formal second order accuracy.

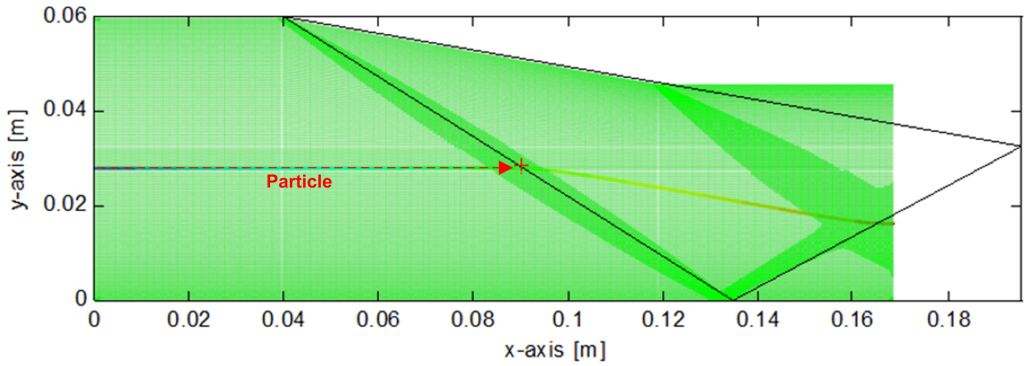

Figure 10: Computational mesh (final) with shock location and particle trajectory overlay

The overlay of prefect gas solution (Mach number and shock wave location) is created with MATLAB using the Hugoniot equations given in chapter 2.2.1 on page 10.

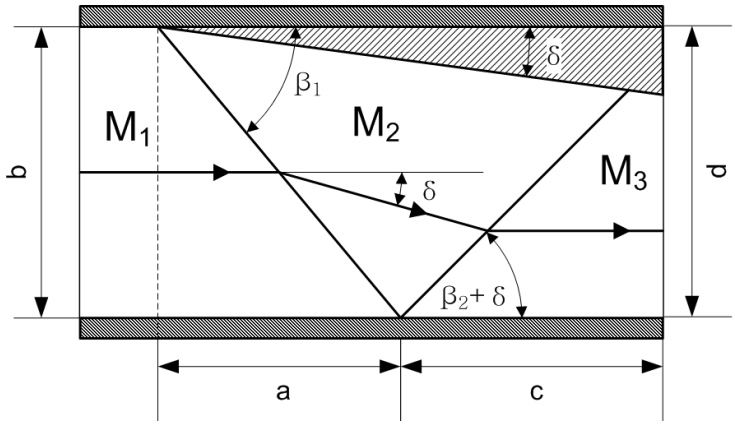

Figure 11: Geometrical parameters of the shock location

The computational domain has a pressure far field inlet on the left-hand side and a pressure outlet on the right hand side. All other surfaces are treated as walls with a hydraulic smooth surface condition. The fluid is air and the density is determined by the the ideal-gas law. From the geometric boundary conditions and the oblique shock wave relations the following geometrical relationships can be determined. The position of the shock is given in equation 2.23.

$$a = \frac{b}{tan(\beta_1)} \tag{2.23}$$

Other useful geometrical parameters for a direct comparison of the ideal gas solution and the computational solution are given as equations 2.24 and 2.25. The meaning of these parameters are pictured in Figure 11.

$$c = b\,\frac{1 - \dfrac{tan(\delta)}{tan(\beta_1)}}{tan(\beta_2 - \delta) + tan(\delta)} \tag{2.24}$$

$$d = c\,tan(\beta_2 - \delta) \tag{2.25}$$

In Figure 13 an inviscid solution, the Spalart Allmaras model and the $K\Omega$ Shear Stress Transport (SST) model are compared with the 1D Hugoniot solution for test case S While, as expected the inviscid solution predicts the same shock and reflected shock wave location as the analytical solution, the other models slightly underpredict due to boundary layer separation. The $K\Omega - SST$ model predicts some more separation, this influences especially the location of the reflected shock. In general the results are qualitatively reflecting the physics when compared to experimental results [43, 44, 80, 85].

As can be seen from Figure 12, the Spalart Allmaras model predicted a very thick shock, which is in no relation to theory or experimental results and is thus not used for any further investigation. The shock thickness predicted by the SA model is independent of mesh refinement.

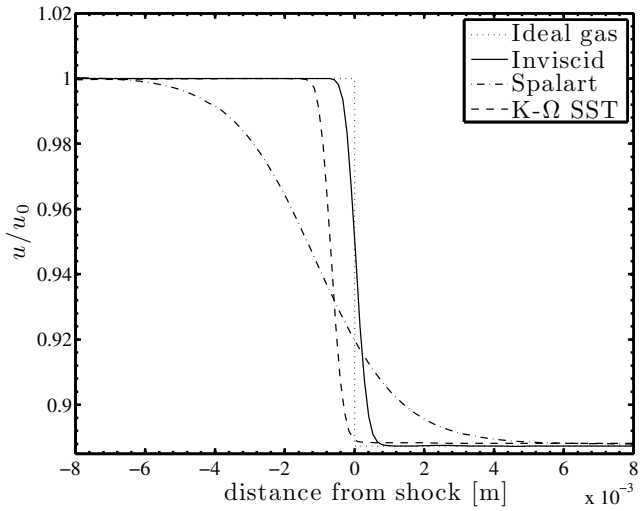

Figure 12: Comparison of velocity profiles

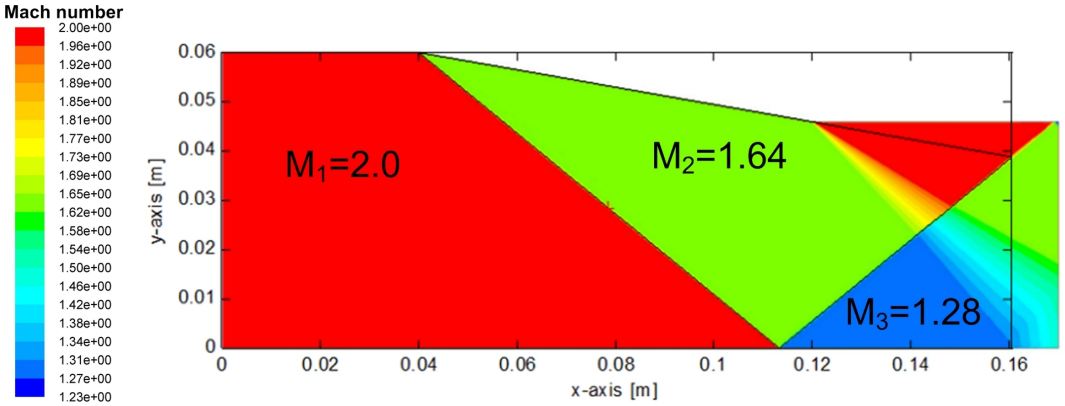

(a) inviscid model

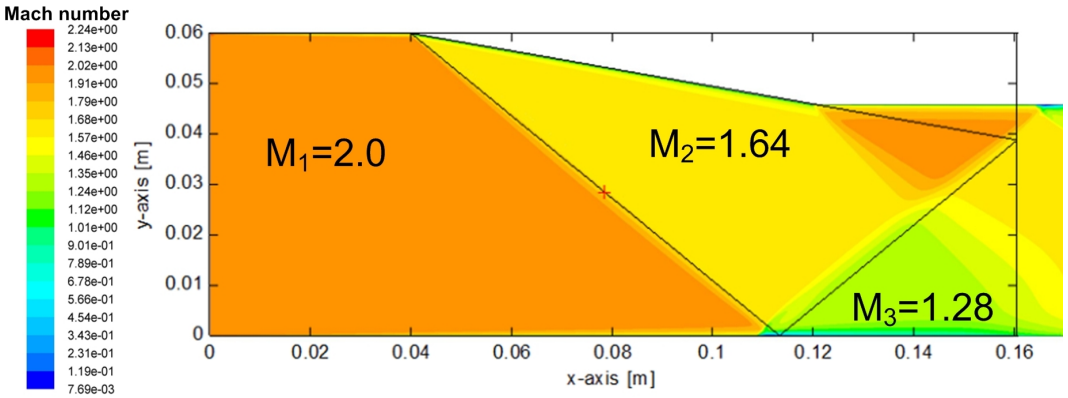

(b) Spalart Allmaras model

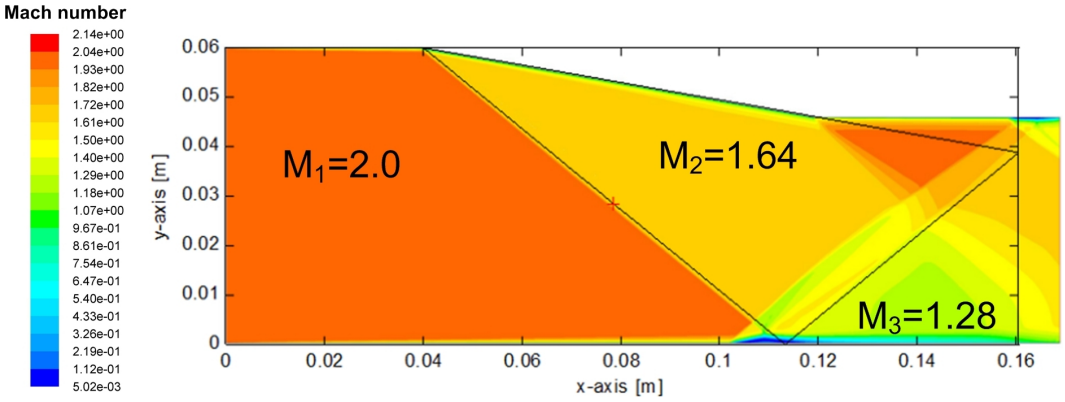

(c) $K\Omega - SST$ model

Figure 13: Comparison of different turbulence models at the test case III

2.3.3 Results

The results are very similar to the ones obtained by the one dimensional modeling, which is expected as Fluent only uses a underlying, relatively simple Runge Kutta algorithm to solve

for particle trajtories. The simple drag equations implemented by default are the “Spherical drag law”, “Non spherical drag law”, “Stokes-Cunningham drag law”[7], “High Mach number drag law” or a user defined script. The difference is a more realistic inclusion of the velocity profile across the shock. The User Defined Function code used to implement the Henderson model into the solver is given in Appendix A User Defined Function Fluent.

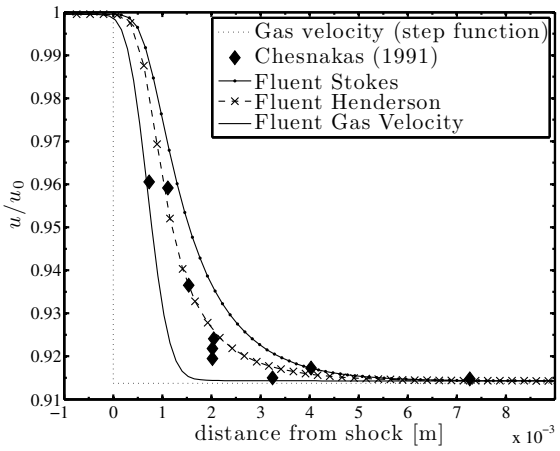

(a) test case C I ($d_p = 0.6\mu m$, subsonic slip flow)

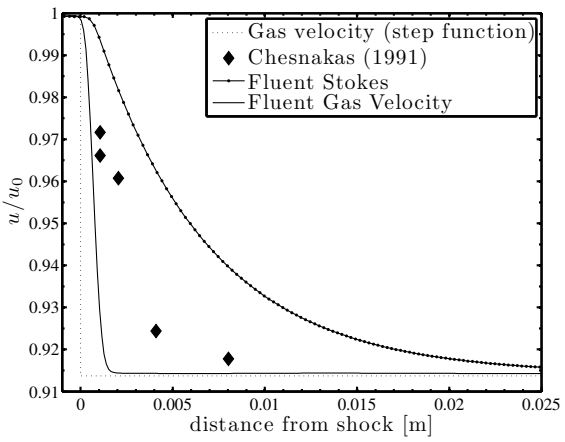

(b) test case C II ($d_p = 1.5\mu m$, subsonic slip flow)

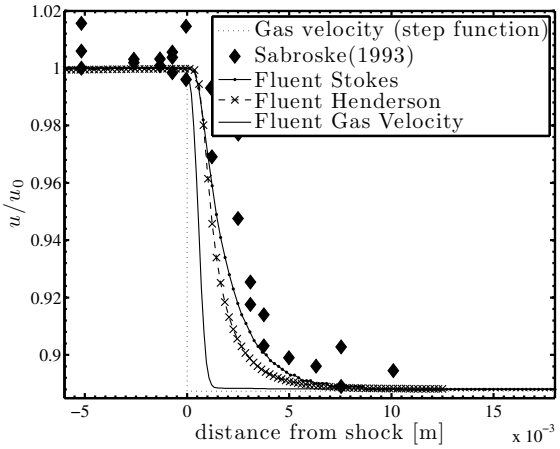

(c) test case S ($d_p = 0.8\mu m$,subsonic slip flow)

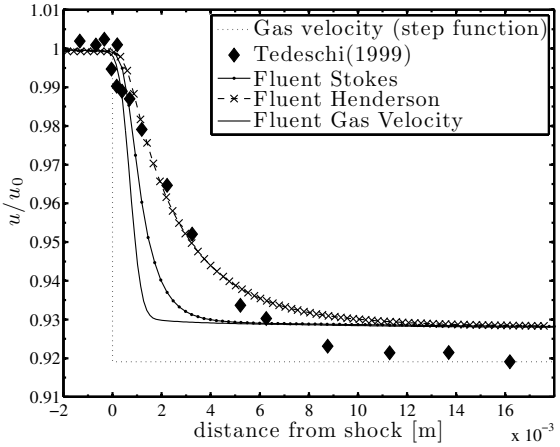

(d) test case T ($d_p = 0.523\mu m$, subsonic transition flow)

Figure 14: Calculations of particle movement through an oblique shock using different drag laws

[7] no correction factor is implemented as standard, simplifying to Stokes expression

2.4 Analysis of Particle Response to Turbulent Fluctuation

Melling [66] showed in his review paper a thorough analysis of particle motion of tracer particles in turbulent flows. He presented a solution by Chao [13] who did a Fourier transform of the equations of motion.

$$\Omega^{(1)} = 1 + f + \frac{f^2}{2} + \frac{f^3}{6} + \frac{f^4}{36}$$
$$\Omega^{(2)} = 1 + f + \frac{f^2}{2} + \left(\frac{2s+1}{3}\right)\frac{f^3}{6} + \left(\frac{2s+1}{3}\right)^2\frac{f^4}{36} \tag{2.26}$$

From these equations a relationship between the kinetic energy of the particle velocity fluctuations $\overline{u_p^2}$ and the fluid velocity fluctuations $\overline{u_f^2}$ is derived. This relationship is as follows:

$$\frac{\overline{u_p^2}}{\overline{u_f^2}} = \int_0^\infty \frac{\Omega^{(1)}}{\Omega^{(2)}} E(\omega) d\omega \tag{2.27}$$

Using these transformations and the characteristic frequency of the particle motion[8], Melling [66] derived approximate equation 2.28 for high particle to fluid density ratios.

$$\frac{\Omega^{(1)}}{\Omega^{(2)}} = \left(1 + \frac{\omega^2}{C^2}\right)^{-1} \tag{2.28}$$

$$E(\omega) = \frac{2}{\pi\omega_c}\left(1 + \frac{\omega^2}{\omega_c^2}\right) \tag{2.29}$$

Inserting the expression (2.29) for the energy spectrum for fully developed turbulent pipe flow as developed by Haertig and equation (2.28) into equation (2.27) Melling was able to integrate the equation for the velocity fluctuations and to come to an analytical solution for the dependency of the ratio of velocity fluctuations and the highest turbulence frequencies of interest.

$$\frac{\overline{u_p^2}}{\overline{u_f^2}} = \left(1 + \frac{\omega_c}{C}\right)^{-1} \tag{2.30}$$

Following the analysis Melling [66] has shown for continuum flow, non continuum drag models can be applied to the problem. The relative velocity between the particle and fluid is obtained from the RMS value of the ratio of velocity fluctuations as shown in eq. 2.31.

[8] based on the Stokes drag coefficient as given in equation(2.9)

$$u_f - u_p = u_f \left(1 - \left(\frac{\overline{u_p^2}}{\overline{u_f^2}} \right)^{1/2} \right) \tag{2.31}$$

This is necessary in order to obtain a relative particle Reynolds number which is a required parameter for most extended drag equations, but also the relative Mach number requires the velocity difference.

$$Re_r = u_f \left(1 - \left(\frac{\overline{u_p^2}}{\overline{u_f^2}} \right)^{1/2} \right) \frac{\varrho_f d_p}{\mu} \tag{2.32}$$

Even though equation (2.30) is derived based on the assumption of Stokes drag, it can be justifiable to use different drag models in order to estimate a frequency response for non continuum flow. Especially for the Cunningham drag model (2.11) and Tedeschi's simplified multi regime expression (2.16) this is possible as they only differ from the Stokes expression by a factor. This factor is a function of the Knudsen number and can be assumed constant if the temperature is not changing at a given position in a flow. Also Tedeschi's non simplified equation (2.15) is valid for amplitude ratios close to unity as the Reynolds number is very low in these regions.

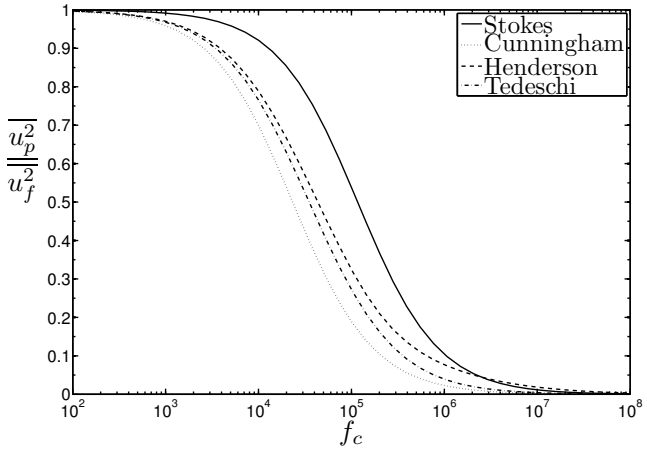

Figure 15: Comparison of the frequency response of different drag models for water particles (d=0.5 μm) in supersonic flow (M=2.0, T=163K ,p=6.5x10³ N/m²)

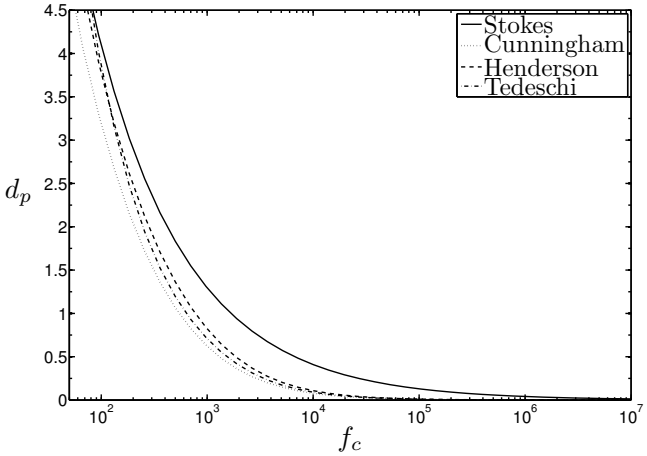

Figure 16: Comparison of the critical diameter in μm for different drag models for supersonic turbulent (η=0.99) flow (M=2.0, T=163K ,p=6.5x10³ N/m²)

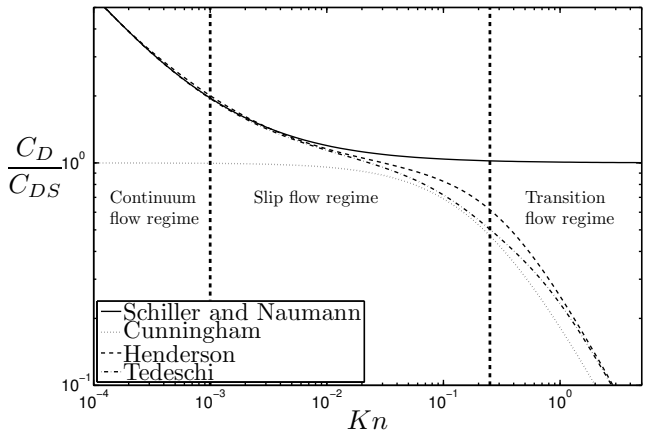

Figure 17: Dependency of the drag coefficient on the Knudsen number, with an amplitude ratio of η=0.99 - normalized by the Stokes drag C_{DS} for water particles in air

The computed values using the Stokes, Cunningham, Henderson and Tedeschi drag models can be seen in figure 15 for the example of a water particle in subsonic slip flow. From the figure the relative fluctuation intensities of the particle and fluid velocities in a turbulent flow field as a function of the cut off turbulence frequency for the given particle parameters can be estimated. It becomes clear that for the given case of slip flow, the predicted cut off frequencies are considerably smaller when using the more suitable drag models. Physically this can be explained by the lower drag coefficients due to slip effects on the particle surfaces. Therefore the particles cannot follow the flow as well as it would be the case in continuum flow.

Using smaller particles is a possibility for improving the frequency response of the mea-

surement. However in optical measurements particle sizes are also limited by their optical characteristics, such that bigger particles provide an improvement in the signal to noise ratio at the cost of a worse frequency response. One way to encounter this is to improve the optic characteristics by using a reflecting dye on the particle surface.

In order to quantify his results Melling used the solution of Hjelmfelt and Mockros [39] for high density ratios and showed that $\overline{u_p^2}/\overline{u_f^2} = 0.95$ is equal to the amplitude ratio of η=0.99. This can be shown from manipulation of equations (2.30) and (2.33). The amplitude ratio indicates how well the particle follows the fluid - $0 \leq \eta \leq 1$ means that the particle is slower than the fluid, $\eta > 1$ means that the particle is moving faster than the fluid. So for η=0.99 the particle follows the flow within 1% of deviation, which is acceptable as the overall measurement error is usually higher.

$$\eta = \left(1 + \frac{\omega_c^2}{C^2}\right)^{-1/2} \tag{2.33}$$

From equation (2.33) the necessary particle size for a certain cut off frequency limiting the dynamic range of the measurement can be determined. The computed graphs for an example slip flow are shown in Figure 16. The curve for the Stokes flow is valid for all continuum regime type flows (at low Re) but again shows a considerable deviation from the other drag models in the range of about one order for smaller particles that are more likely to encounter slip flow effects due to the influence of the particle size. This also result into the merging of the curve of the Stokes model and the Henderson and Tedeschi model for large particle sizes which correspond to smaller Kn numbers. The Cunningham model is only valid for slip flow and does therefore under-predict the cut off frequency in continuum flow regime.

However, as can be seen from Figure 17, the applicable drag models for slip flow do not always predict higher values for the drag compared to Stokes law. Therefore drag laws can predict higher or lower cut off frequencies in this regime ($0.001 < Kn < 0.25$). This is for the first part due to additional high Reynolds numbers correction that the Stokes law is missing, but is accounted for by the Schiller and Naumann drag law (1<Re<800) . In the second part of this regime the slip effects grow stronger and lead to a drop in the drag coefficient. Most applicable drag models do account for rarefaction by incorporating the Knudsen number in the expression.

The same observation can be made when reviewing the before introduced test cases. In Figure 18a to 18d the particle response to turbulent fluctuation is shown for each respective case for the flow situation before and after the shock. The first three cases all happen to be in

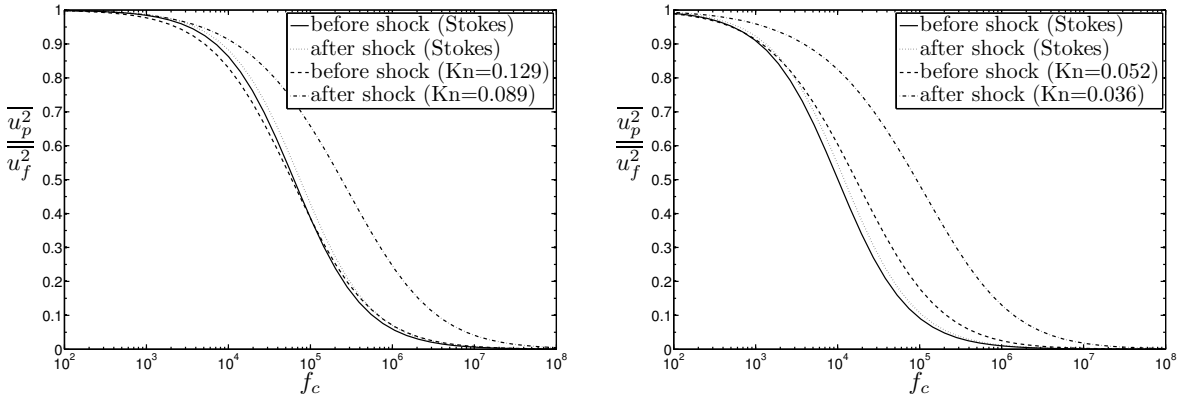

(a) test case C I ($d_p = 0.6\mu m$, subsonic slip flow)

(b) test case C II ($d_p = 1.5\mu m$, subsonic slip flow)

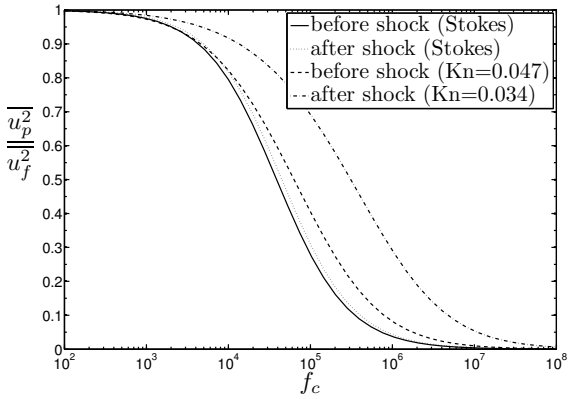

(c) test case S ($d_p = 0.8\mu m$, subsonic slip flow)

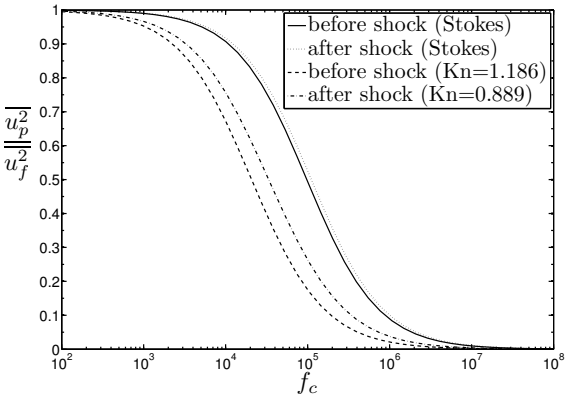

(d) test case T ($d_p = 0.523\mu m$, subsonic transition flow)

Figure 18: Calculations of of the frequency response for different cases using the Tedeschi drag law

the slip flow regime and can be used to picture this trend. The curves using Stokes drag for before and after the shock are shown for reference - they are slightly different due to changes of the viscosity with temperature. In Figure 18a it becomes visible that the thermodynamic changes caused by the shock have a strong influence on the drag coefficient. The Tedeschi model predicts higher drag for the low Kn number flow before the shock and lower drag for the high Kn number flow after the shock, so this case centers around the inflection point of the drag model in the slip flow regime. The same phenomena can be seen for cases C II and S. In the transition case pictured in Figure 18d the predicted drag due to slip and rarefaction effects is always lower than the Stokes drag and therefore the cut off frequencies will be lower, too.

3 Windtunnel Seeding

Seeding conditions important for Laser Doppler applications are described by F.L.Crosswy [32]. Based on these, but extended for the application in supersonic windtunnels, the conditions desired for high speed windtunnel measurements are: (1) sub-micron particle size, (2) uniform mono-dispersed particle size distribution, (3) high mass flow rate for good data rates, (4) high refractive index, (5) applicable for high back pressure condition, (6) cost efficient, and (7) easy to include in the wind tunnel setup.

In addition to the above requirements Keane and Adrian [50] suggest a minimum particle per volume density of at least 15 particles per interrogation volume for PIV measurements. To further render the seeding issue more difficult, the particles have to be small enough to follow the flow, but big enough to back scatter enough light to allow measurement [84] with good signal to noise ratio. It is also desirable to take into account the health and safety related features that are described by Melling [66]. Particles therefore should ideally be non-toxic, non-corrosive, non-abrasive, non-volatile and chemically inert. Nichols [70] suggested the possibility to account for particle response with a correction method for Laser Doppler Velocimetry measurements given a mono-dispersed particle size distribution. For these corrections it is assumed that all influences except the drag can be neglected. From the comparison of experimental data with analytical and semi-empirical relationships for the drag coefficient it can be seen, that this would only be reasonable for very small particles, and even then one might add more uncertainties by doing so.

In general wind tunnel seeding methods can be split up in fluid and solid particle generation. Some sample values (adapted from TSI [98], Budwig [11], Mazumder et al. [65]) for commonly used LDV and PIV seeding materials are given in table 3. The following sections will elaborate on how these particles are distributed or generated as an aerosol. Some topics are overlapping and split up the most systematic way possible.

Particle substance	Type	Refractive Index	Density $[10^3 kg/m^3]$
Polystyrene Latex Sphere (PSL)	Solid	1.55-1.6	1.05
Titanium dioxide	Solid	2.6	3.5-4.2
Dioctyl Phthalate (DOP)	Fluid	1.4	0.98
Olive Oil	Fluid	1.47-1.48	0.92
Water	Fluid	1.33	1.0

Table 3: Seeding particle properties

3.1 Solid Particle Seeding

3.1.1 Metal and Ceramic Particles

The use of metal and ceramic particles for windtunnel seeding is especially preferred for high temperature[36, 106] and combustive flows where other seeding materials would not be possible. The particle can be introduced into the flow by a Fluidized Bed Seeder. In this type of seeder solid particles are continuously stirred and carried away by a carrier gas like air or nitrogen into the wind tunnel. Other types of seeders are brush powder generators[97]) and cyclone aerosol generators.

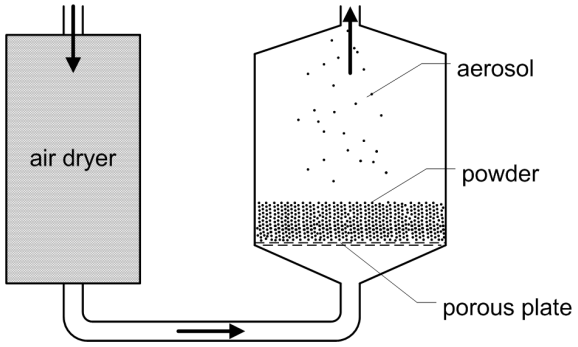

Figure 19: Fluidized bed seeder (adapted from Melling [66])

The study by F.L.Crosswy [32] on seeding methods for LDV showed, that none of the commercial powders used had a narrow particle size distribution. Also the influence of agglomeration on the particle size distribution is shown. Similar experiences have been made by Patrick and Paterson [74] and Humble et al. [44]. They reported highly poly-dispersed particle distributions due to agglomeration. Therefore a filter device may be necessary to prevent agglomerated particles from entering the facility. Possible improvements for solid particle seeding are the use of flow agents and additional steps to reduce moisture entering the seeding material. Specific filtered metal seed can have a very narrow bandwidth of particle diameters if agglomeration is prevented. Most particles have an abrasive nature and are of irregular shape and size. This often does not allow its use in closed loop wind tunnels because of possible damage to the compressor or fan [83]. Figure[9] 20 shows a cyclone type of seeder currently used in the SSWT facility. The aerosol is generated by a tangential high speed air jet and distributed in the flow with a row of copper turrets. Particle agglomeration and particle distribution on the optical access windows were observed and led to discontinuation of this seeding methods for the current applications.

[9]the type currently used in the SSWT, design by Dr. Byun and Dr. Lowe

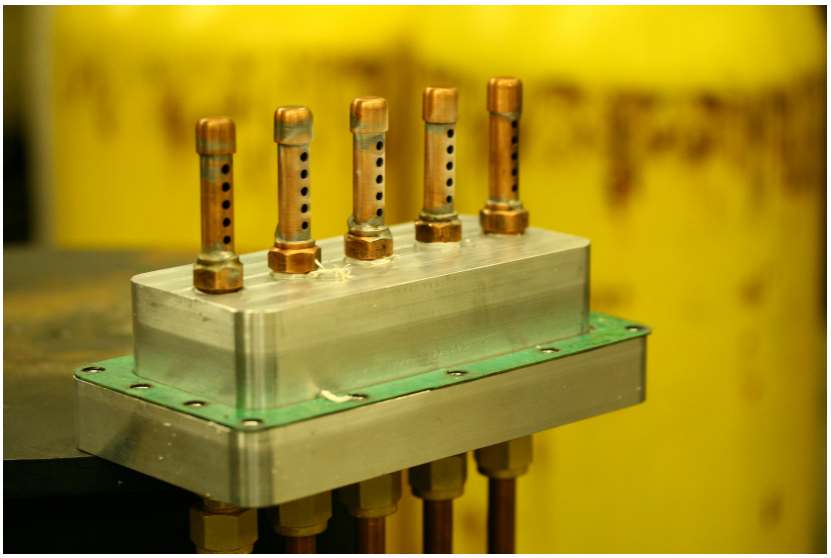

(a) Nozzle assembly

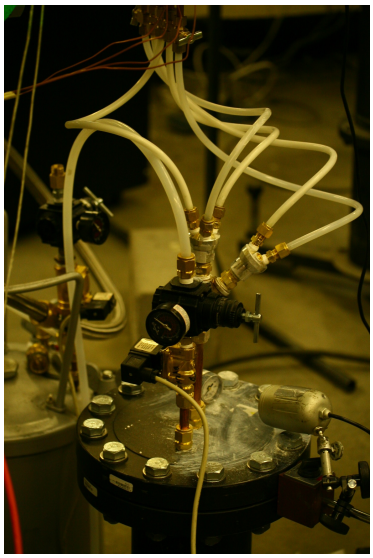

(b) Cyclone/fluidized bed seeder

Figure 20: TiO2 seeder

Reference	Flow Conditions	Measurement setup	Generator	Material	Particle size [μm]
Havermann et al. [36]	Supersonic	PIV	Fluidized bed seeder	TiO_2 and Al_2O_3	0.3
F.L.Crosswy [32]	NA	LDV	NA	MgO, Al, TiO_2	0.05-1.0
Wernet et al. [106]	Supersonic	PIV	Ethanol suspended spay	Al_2O_3	0.7
Humble et al. [44]	Supersonic	PIV	Fluidized bed seeder	TiO_2	0.4
Urban and Mungal [99, 100]	Supersonic	PIV	Fluidized bed seeder	TiO_2 and Al_2O_3	0.015, 0.23 and 0.3
Current study	Supersonic	LDV	Cyclone seeder	TiO_2	0.2

Table 4: Overview of metal particle seeding references

Using metal or ceramic powders as seeding materials has been a common practice for many wind tunnels (compare list of references in table 4). Application seems to be dominant for PIV measurements in supersonic facilities. Given the right powder is chosen, the advantages of this seeding are the narrow particle size distribution, small particle diameters and the high refractive index. But because of its abrasive nature and the tendency to agglom-

erate during seeding or storage it may not be recommended for every application. Also the weight of metal and ceramic powders are often much higher (factor 3-4) than other types of seeding materials, increasing its velocity lag due to inertia. Additionally particle distribution on optical access windows may emerge as a problem.

3.1.2 Fluidized CO_2 Seeding

Reeder et al. [81] describe a new clean seeding concept of using liquid carbon dioxide particles in a large supersonic wind tunnel facility. Within this approach gaseous CO_2 is injected upstream of a supersonic M=8.0 nozzle. As the gas accelerates through the converging diverging nozzle it cools down and nucleates to CO_2 particles – also known as dry ice. The solid ice particles sublimate from solid directly to gas, so that no liquid or solid particles will be present further downstream of the measurement volume[23]. The particle size was controlled by a two step expansion process, similar to the process proposed in the US Patent 4,806,171 from 1989 [107]. After the second expansion particles agglomerate and form large particles (larger than the particle sizes after the first expansion, compare to Figure 21). The smallest CO_2 particles Reeder generated were of 7 µm in diameter, which compared to other seeding methods is very large. Also the size distribution was not uniform.

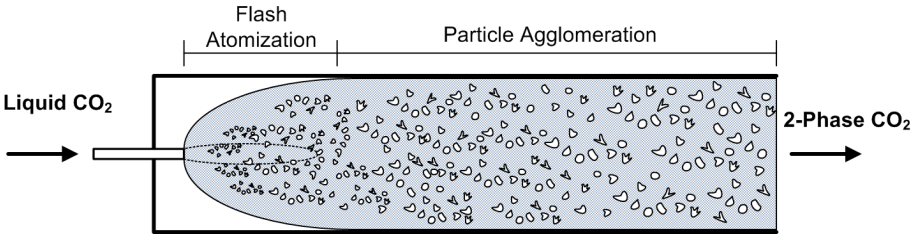

Figure 21: Flash atomization of fluid CO_2 (adapted from Reeder et al. [81])

The paper enforces the need for sufficient particle size control in order to use it for wind tunnel seeding applications. Poggie et al. [76] was able to generate CO_2 particles in a range from 10 to 100 nm for quantitative flow visualization in supersonic and hypersonic flows. This seeding is used for Condensate enhanced Rayleigh scattering, which is a flow visualization technique for recording densities of transparent gas flows[90]. Dry ice seeding seems to be a very promising method for seeding wind tunnels. Especially in large scale facilities, where contamination of other instruments has to be avoided at any cost, it could open new possibilities. Experiments have shown that very small particles can be obtained, and by control or adjustment of evaporation a very mono-dispersed and low inertial particle could be generated. However, in the current stage of development considering the problems

of particle sizing and the more expensive setup, it is still not a common alternative to typical seeding methods.

Reference	Flow Conditions	Measurement setup	Generator	Material	Particle size [μm]
Reeder et al. [81]	Supersonic	LDV, PIV	Custom	Solid CO_2	5-10
DeLapp and Reeder [23]	Supersonic	PIV	Custom	Solid CO_2	1-20
Poggie et al. [76]	Supersonic, hypersonic	Condensate enhanced Rayleigh scattering	Custom	Solid CO_2	0.01-0.1

Table 5: Overview of solid CO_2 seeding references

3.1.3 Polystyrene Latex Spheres (PSL)

Injection of Polystyrene Latex (PSL) spheres is an established and reliable approach for subsonic LDV and PIV seeding. The PSL spheres are dispersed in the carrier fluid, usually a mixture of alcohol and water. Typical sizes for these purchasable particles range from 0.25 to 1.0 µm. Since PSL spheres are manufactured in specified sizes verified by optical measurement they are considered a primary standard for particle sizing applications.

Seegmiller et al. [88], Seegmiller [87] describes several PSL seeding procedures used for subsonic, transonic and supersonic wind tunnel facilities. Several different atomizing nozzles for injection of the PSL/carrier fluid mixture are discussed. Seegmiller et al. [88], Seegmiller [87] successfully used 0.4 µm Polystyrene spheres for the experimental investigation of unsteady compressible sub/transonic flows over airfoils at the Ames Research Center[88, 87]. The particle lag was reported to be very small, and a 99% velocity adjustment was obtained after 1 mm. Chesnakas [14] used an injection design based on a design originally proposed by Seegmiller. It uses two air holes per fluid hole at a 20° angle to the flow direction, taking advantage of the Venturi effect to inject the seed. The author reports excellent mono-dispersed particle distribution and only little agglomeration of the 0.6 µm PSL spheres used. He also tested 0.24 and 1.5 µm to determine particle lag times. The 0.24 µm spheres were not used for final measurements due to the low levels of light scattering which made them unusable for his LDV measurements. Rabe and Dancey [79] used PSL spheres dispersed in isopropanol injected by a TSI six jet atomizer for boundary layer measurement. The reported PSL sphere size was 0.48 µm. They also compared a range of particle sizes from 0.48 to 2.95 µm at a free-stream velocity of 30 m/s and concluded that the measured mean velocity is not very

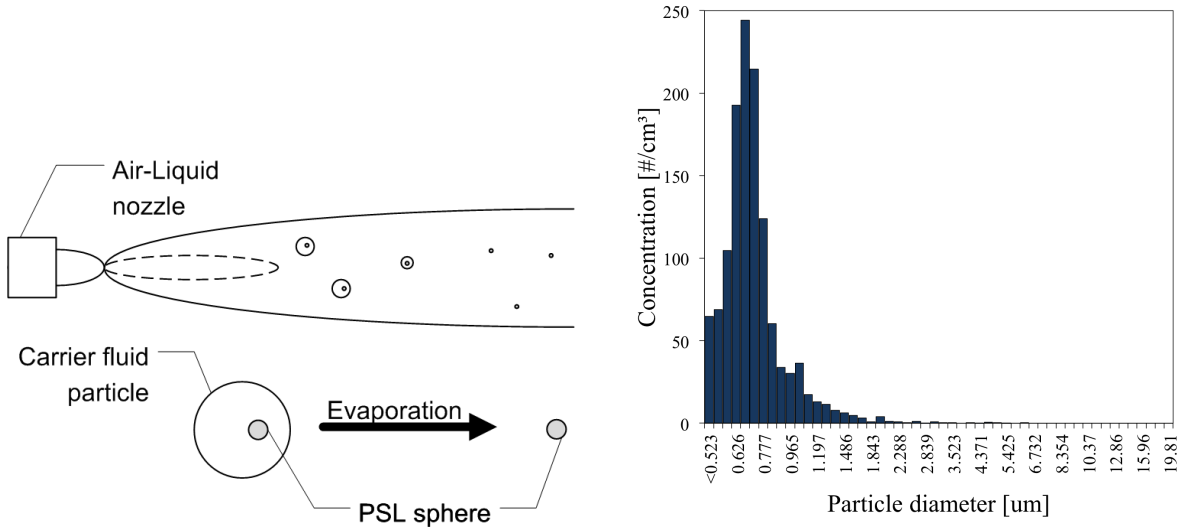

(a) PSL evaporation

(b) Particle size measurement of 0.7μm PSLs in the SSWT using a TSI particle sizer

Figure 22: Properties PSL seeding

much dependent on the particle size. However, turbulence statistics and data rate are very dependent on the diameter. Some examples of application of PSL seeding for various wind tunnel conditions can be found in table 6.

Sabroske [83] used 0.8 µm PSL seeding for the Compressor Research Facility at Wright-Patterson Air Force base in 1989 but ruled this type of seed as unusable for this certain facility because of the high maintenance caused by instrument clogging. F.L.Crosswy [32] used a Collision atomizer to atomize the carrier fluid for the PSL spheres but reported an unsatisfactory poly-dispersed particle distribution. Most likely the carrier fluid did not evaporate completely and big fluid particles contributed to the particle distribution. This underlines the importance of atomizing and evaporation adjustment of the whole setup for the specific wind tunnel application. Wasserbauer and Hathaway [104] used 0.85 µm PSL seeding for the NASA Low-Speed Centrifugal Compressor flow field. Some problems of PSL agglomeration due to storage are reported. The authors suggest a device to mechanically remove clogged PSL from the nozzle and give practical advice for blending PSL with different carrier fluids. They also underline the need for adjustable seeding nozzles to seed the regions in focus. Adjustment of the setup is necessary to reach a seeding state where the carrier fluid is evaporated and only the PSL spheres are left in the flow. Agglomeration of PSL particles can be reduced by using a ultra sonic cleaning device as reported by Tedeschi et al. [94]. The extensive study on supersonic windtunnel seeding done by J.Lepicovsky and R.J.Bruckner

[48]concluded that difficulties in evaporating the carrier fluid can outrule PSL seeding for certain facilities. Even if the exact size of the particles is known, the measured droplets might be much larger. Also re-condensation due to the step temperature gradient emerges as a special problem. Meyers [67]'s lecture about seeding techniques for wind tunnels concludes that the PSL spheres with their spherical and low inertial features, their mono-dispersed particle distribution and their low cost are superior to seeding with liquid or metal powder particles. The report underlines the optical features and the high index of refraction as advantageous for optical measurement. Meyers gives a detailed view of the manufacturing process and proposes a 1:1 water ethanol mixture as the carrier fluid to ensure complete evaporation and avoid agglomeration.

The experiences with PSL seeding in the Virginia Tech Supersonic Windtunnel are various. At first an agriculture style nozzle[10] was used to produce the aerosol, but complete evaporation could not be obtained. Also low seeding rates, high background noise due to re-condensation and fluid streaks contaminating the optical access were observed. To overcome the evaporation problem a heated tube was inserted between the seeding insert and the nozzle, but this effort did not lead to any improvement. In a second trial a Laskin nozzle[11] , usually used with DOP, was filled with a 0.5 μm diameter PSL mixture, but also this test proved unsuccessful.

To fix these issues an ultrasonic nozzle[12], type sonicom (H035) made by JD Ultrasonics[13] as currently used by NASA Langley is mounted directly in the windtunnel plenum. Figure 23a shows the Ultrasonic nozzle mounted on the windtunnel seeding insert. Figure 23b shows the vey fine mist generated during a subsonic nozzle test.

However, particle clogging the ultrasonic nozzle even after a short period of time made it difficult to operate effectively. In order to stop the nozzle from clogging, several methods of particle treatment were employed. First the PSL solution is treated with a Ultrasonic Cleaning device to break up agglomerated particle structures. Afterwards the complete solution is filtered through a 50 μm pore size filter[14] to remove sediment and agglomerations from the mixture. After treatment the nozzle clogging did no occur, even after several days of mixture storage, which indicates the problem to be caused by long time storage rather than the short time during windtunnel runs.

[10]more on this type of atomization can be found under section 3.2.3 on page 39
[11]more on this type of atomization can be found under section 3.2.1 on page 36
[12]more on this type of atomization can be found under section 3.2.4 on page 41
[13](http://www.jdultrasonics.co.uk), distributed by Sealpump Engineering Limited (http://www.sealpump.com) through Conveyor Specialities (http://www.conveyorspecialties.com) in the US
[14]Alternatively an inline filter or an inline static mixer as it is used in chemical industry could improve the mixture of the solution and break up agglomeration.

Surplus fluid discharging from the nozzle during the air valve shut down process caused light fluid streaks on the optical access windows. This problem was solved by closing both the fluid and air line with a delay. The fluid line is closed first and the air line left open till the fluid in the open part of the fluid line is emptied. Later measurements of the particle velocity in the lag region after a shock revealed incomplete evaporation and big particles sizes in the flow.

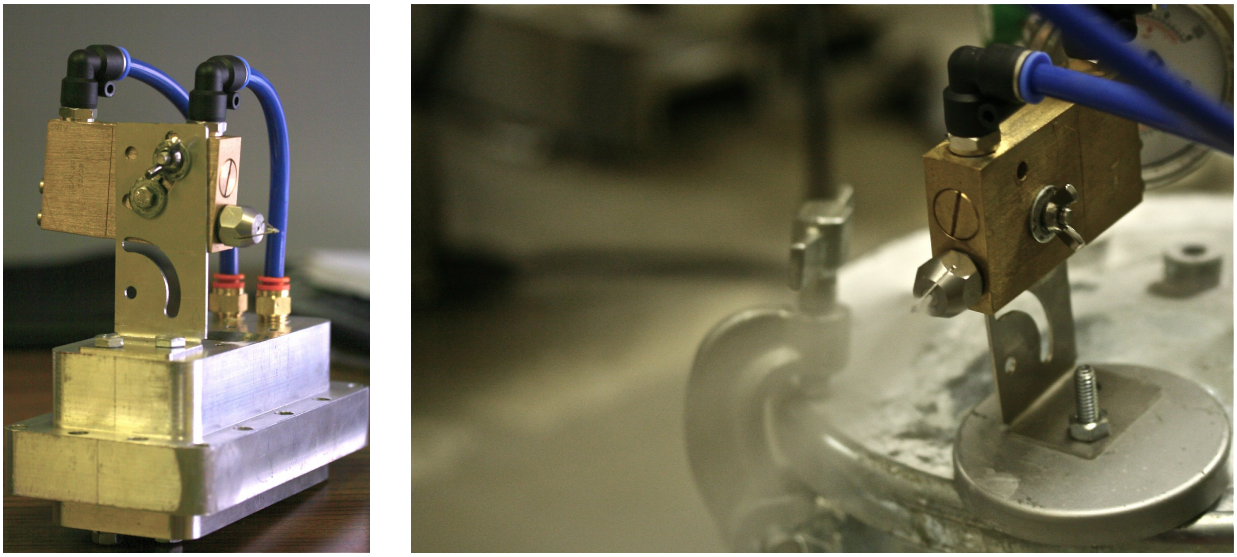

(a) Nozzle assembly (b) Spraying cone

Figure 23: Ultrasonic Nozzle

It can be concluded from reported experiences that PSL spheres can be a very good solution for windtunnel seeding. The mono-dispersed particle size distribution, the completely spherical shape and the small particle sizes possible, render it as a good tracer particles for LDV or PIV applications in non combustive flows in open loop wind tunnels. To obtain the mono-dispersed particle distribution, it has to be ensured that the carrier fluid atomizes properly and evaporates before the mixture reaches the measurement volume. Influencing factors are the atomizing nozzles used, the flow rates of the carrier fluid, atomizing gas and the mixture of the carrier fluid itself.

Another important aspect is the avoidance of particle agglomeration during atomization and storage of the PSLs. If these critical points are considered it is a reliable way of seeding mono-dispersed particles and allows obtaining qualitative good velocity and turbulence measurements in wind tunnels.

Reference	Flow Conditions	Measurement setup	Generator	Material	Particle size [μm]
F.L.Crosswy [32]	NA	NA	Collusion nebulizer	PSL, water, methanol	0.35-0.55
Seegmiller [87]	Subsonic, transonic, supersonic	NA	Custom	PSL	0.35-0.55
Seegmiller et al. [88]	Subsonic M=0.76-0.79	LDV	NA	PSL	0.4
Rabe and Dancey [79]	Subsonic, transonic	LTA, LDV	TSI Model 9306 six jet atomizer	PSL, iso-propanol	0.48
Sabroske [83]	NA	LDV	Six jet atomizer, Laskin nozzle	PSL	0.8
Wasserbauer and Hathaway [104]	Subsonic	LV	Commercial atomizing nozzle	PSL, water, Ethyl alcohol	0.85-1.10
Chesnakas [14]	Transonic, supersonic	LDV	Seegmiller Design [87]	PSL, Ethanol	0.6
Meyers [67]	Subsonic, transonic	LDV	Array of agriculture spray nozzles	PSL, Ethanol	0.6
Tedeschi et al. [95]	Supersonic	LDV	Dantec 5L17 atomizer	PSL	0.523
Mazumder et al. [65]	Subsonic	LDV	Laskin nozzle type	PSL	0.1-1.0
J.Lepicovsky and R.J.Bruckner [48]	Supersonic	LDV	Spray nozzle	PSL, Ethanol	1.1
Lepicovsky et al. [58]	Supersonic	LDV	Atomizer-based aerosol generator	Water, Ethyl alcohol	1.18
Current study	Supersonic	LDV	Agricultural, Laskin and Ultrasonic nozzle	PSL, water, Ethyl alcohol	0.5, 0.833

Table 6: Overview of PSL seeding references

3.2 Fluid Particles Seeding

3.2.1 Laskin Nozzle

The working principle of the Laskin nozzle is simple. A high velocity air jet shears off particles from a fluid column and bubbles containing the aerosol move up towards the output of the apparatus. Often an impactor is placed after the Laskin nozzle in order to remove bigger particles. Big particles that cannot follow the abrupt change in flow direction, imapct on the wall and therefore get "filtered" out.

The designs proposed by Echols and Young [29] feature a flow rate ranging from 32 liter per minute to about 90 liters per minute and particle sizes peaking a little below than 1 micro meter.They conclude, that the final size distribution is mainly dependent on the jet impactor and its flow velocity. The average light scattering diameter of the DOP particles in the designs reached from 0.70 to 0.89 µm. Also high concentrations of particles below 0.69 µm are reported. It is observed that increasing working pressures for all designs resulted in smaller mean diameters.

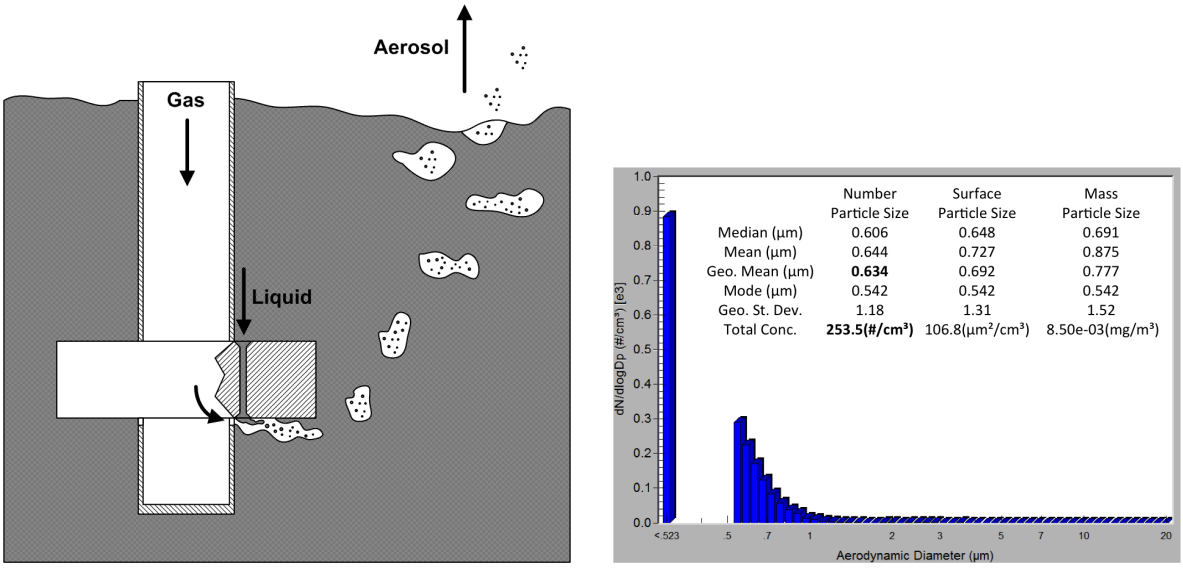

(a) Aerosol generation in a Laskin nozzle

(b) Particle size measurement of DOP in the SSWT using a TSI particle sizer

Figure 24: Properties Laskin nozzle seeding

Willert et al. [108] used an array of Laskin nozzles for PIV and LDV measurements in large scale industrial wind tunnels at the German Dutch Wind Tunnel facility operated by the DLR and NLR; the reported particle diameter was about 1 µm. A particle size distribution was not included. Rabe and Sabroske [78] used a Laskin nozzle with a 2 or 4

hole setup. The hole diameter was 2.2 mm. Variation between a 2 or 4 hole setup showed a better seeding efficiency for the 2 hole setup. They noted a temperature dependency of the particle diameters produced. Therefore the authors suggest performing seed generation under stable temperature conditions.

Reference	Flow Conditions	Measurement setup	Generator	Material	Particle size [μm]
F.L.Crosswy [32]	NA	NA	Laskin nozzle	DOP	0.5-0.7
Echols and Young [29]	NA	NA	Custom design	DOP	0.70-0.89
Willert et al. [108]	Subsonic, transonic	PIV	Array of Laskin nozzles	Oil	~1
Rabe and Sabroske [78]	Subsonic, transonic	LDV, PIV	Laskin nozzle	Propylene, Glycol, Silicon Oil	1<
Klaas et al. [54]	Supersonic	LDV, PIV	Laskin nozzle	Di-Ethyl-Hexyl-Sebacat	1.0-1.5
Fey et al. [31]	Transonic	PIV	Laskin nozzle	Oil	NA
Tanna and Morris [93]	Subsonic	PIV	Laskin nozzle	Hydraulic Oil	~1
Jun et al. [49]	Subsonic, Supersonic	PIV	Laskin nozzle	Di-Ethyl-Hexyl-Sebacat	~1
Köhler et al. [55]	NA	NA	Simple nozzle, Laskin nozzle, suction nozzle	Vegetable Oil, Di-Ethyl-Hexyl-Sebacat	1<
Li et al. [59]	Subsonic	PIV	Laskin nozzle	Olive Oil	3
Current study	Supersonic	LDV	Laskin nozzle	DOP	0.65

Table 7: Overview of Laskin nozzle seeding references

Laskin nozzles are a reliable way of seeding wind tunnels but do not reach the monodispersed particle size distribution Poystrene spheres feature. Particle size and particle size distribution can be significantly enhanced by aerosol conditioning using a vaporiza-

tion/condensation unit (VAP/CON). From particle size measurements it is found that the concentration is a function of the pressure at the nozzle only, the mean particle size is almost constant.

3.2.2 Vaporization Condensation Seeder

The Vaporization Condensation Seeder (VAPCON) vaporizes the injected fluid particles (fed by either by a the Laskin nozzle, Collision Nebulizer or any other kind of atomizing nozzle) and condenses them in a more uniform particle size distribution which was found to be more mono-dispersed [32]. Japuntich et al. [46] analyzed 17 different vaporization condensation units of different design, which all are very similar with respect to the condensation unit which is basically a heat exchange tube in which the previously produced steam condenses to fluid particles. This process of condensation can be described by the heat and mass transfer equations and is mostly influenced by the flow velocity, the heat transfer coefficient and therefore by the ratio of free to convective forces. The authors conclude that the optimum conditions are reached when there is a balance of free to convective forces in the condensation unit. From the data analyzed the authors reasoned that the general conditions for a mono-dispersed particle distribution were met in the mixed convection laminar flow condition. This can be concluded from the equation[46] obtained by linear regression of the condensation unit data available:

$$Re = 0.369 \left[Gr\, Pr \left(\frac{2\, r}{L} \right) \right]^{0.78} \tag{3.1}$$

Where Re is the Reynolds number, Gr is the Grashof number, Pr is the Prandtl number, r is the radius of the condensation pipe and L is the length of the condensation pipe.

The units analyzed by Japuntich et al. [46] produced particle diameters in a very mono-dispersed fashion ranging from 0.4 to 2.5 µm, using different organic fluids and air, nitrogen and helium as carrier gases.

Mazumder et al. [65] used a Rapaport-Weinstock aerosol generator with a heating unit and achieved a more mono-dispersed particle distribution. It was reported that the particle size could be varied from 0.1-1.5 µm by varying nozzle sizes and the alcohol content of the DOP – alcohol mixture. The authors reported good improvement compared to a Laskin nozzle without conditioning.

F.L.Crosswy [32] reports the use of a dilution nitrogen gas flow which led to a better mono-dispersed particle distribution with a higher concentration of smaller particles compared to the undiluted flow. Also mixing DOP/anthracene and ethanol (1/99) resulted in an almost

perfect distribution centering on 0.4 µm and resembling the experience Mazumder et al. [65] made before.

Reference	Flow Conditions	Measurement setup	Generator	Material	Particle size [μm]
F.L.Crosswy [32]	NA	NA	Custom VAP/CON	DOP/ anthracene, ethanol and nitrogen	0.4
Mazumder et al. [65]	NA	LDV	Rapaport-Weinstock aerosol generator	DOP – alcohol	0.1-1.5
Roth et al. [82]	NA	NA	Rapaport-Weinstock aerosol generator	Di(2-ethylhexyl) sebacate	0.2-2.0
Japuntich et al. [46]	NA	NA	Aerosol condensation collector	DOP	0.76
				DOP	0.6
				DOS	0.7
Hopkins [41]	Subsonic	LDV	Yanta type of VAP/CON	DOP	0.7

Table 8: Overview of VAP/CON seeding references

3.2.3 Pressure Atomizer

Pressure atomizers utilize a coaxial high velocity gas jet to shear of fluid particles from a fluid jet. Several designs of atomization nozzles with different shearing geometries exist [16]. F.L.Crosswy [32] points out that the particles generated by a Collision nebulizer are in general larger than the ones produced by the Laskin nozzle. Durox et al. [27] uses an air nebulizer with a similar working principle. It was found that there is no influence of viscosity, vapor pressure or surface tension on particle diameter created by this type of seeding. The particle diameter only depends on the geometric features of the atomizing nozzle itself and the ratio of inertial gas and fluid forces.

The capillary forces in the fluid pipe are necessary for the working principle of some types of nebulizers. The flow rate of the nebulizer used by Durox et al. [27] was not very high

and the concentration of seeding fluid particles decreases slightly with rising carrier fluid pressure.

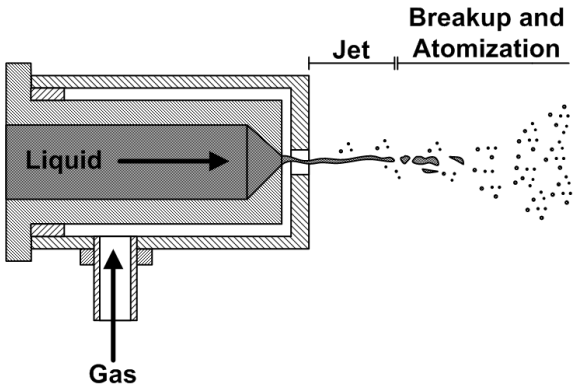

Figure 25: Atomizer

Reference	Flow Conditions	Measurement setup	Generator	Material	Particle size [μm]
Sabroske [83]	Supersonic	LDV	TSI six jet atomizer	Glycerin, Alcohol	0.9
Durox et al. [27]	NA	PDA	Air Nebulizer	Edwards Oil, Olive Oil, Ethanol, Water, etc.	3<
Tillery et al. [96]	NA	NA	Various	Dioctyl sebacate, Water, Fluores-cent dye	1.4-5.4
Pilacinski et al. [75]	NA	NA	Double Orifice nebulizer, modified Wright Nebulizer	Corn Oil	0.8-8
DeOtte et al. [24]	Subsonic	LDV	six jet atomizer	Fog Oil	0.76

Table 9: Overview of Pressure Atomizers seeding references

The mean diameter for the nozzle used was about 3 µm. Other reports mention a

dependence of the particle diameter on the flow rate and geometry, but because of the variety of generators available, no general relationship can be expressed by a simple analytical or empirical equation [96].

Pressure atomizers, like the collision and air nebulizer are a often used method of seeding wind tunnels. They have a more poly-dispersed particle size distribution and particle sizes around 1 µm. Pressure atomizers are successfully used as a feeding device for VAP/CON seeding, which significantly improves the particle size and particle size distribution.

3.2.4 Vibration Assisted Atomizer

The Vibrating Orifice Aerosol Generator VOAG or Ultrasonic atomizer generates particles from a fluid jet by inducing a flow instability. A high speed gas jet is then usually used to transport the generated mono-dispersed droplets. There are two principal types of ultrasonic atomizers, the more expensive variant employs a generator units that drives a piezo crystal in the nozzle, whereas the air assisted type uses a resonator cone in front of the nozzle to break up the droplets.

The advantage of the piezo driven vibrating orifice aerosol generator as described by Berglund and Liu [10] is the possibility to easily calculate the particle sizes from the generator properties. Because of this the authors classify this method as primary standard for particle measurement. The study reports a useful range from 0.5-50 µm. Even though a mono-dispersed particle size distribution is a very important feature for wind tunnel seeding and can be easily achieved with the features the VOAG aerosol generation provides, the low particle mass flow for this aerosol generator may make it impractical to use for experiments in high speed flow.

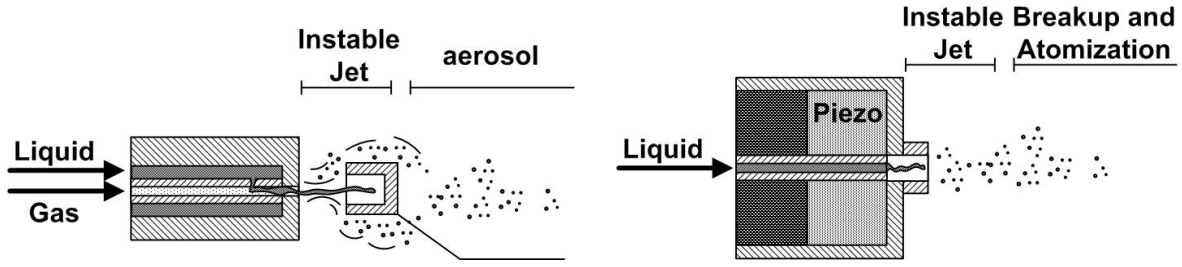

(a) Air Assisted Ultrasonic nozzle (b) Piezo Driven Ultrasonic nozzle

Figure 26: Vibration Assisted Atomizer

The air assisted type does not have an as mono-dispersed particle size distribution as the electric driven nozzle, but is much cheaper in application and installation. It produces

a very fine mist of particles. This type is often used in dust suppression and humidification applications. An example of application for the distribution of PSL spheres is shown in figure 23 on page 34.

4 Laser Doppler Accelerometry for Particulate Flows

The first Laser Doppler[15] systems were introduced in 1964 with two different configurations, the reference beam as the very first approach and the dual beam mode upon which most modern systems are based upon. With the dual beam method two coherent laser beams are crossed and determine a measurement volume. A particle passing through this volume scatters the light and enables the determination of the velocity by utilization of the Doppler effect. The Doppler effect describes the change in apparent frequency due to a moving emitting source[4]. The advantage of the the dual beam approach is that the Doppler shift does not have to be resolved directly and a difference Doppler frequency f_D can be detected by the receiving system [97].[16]

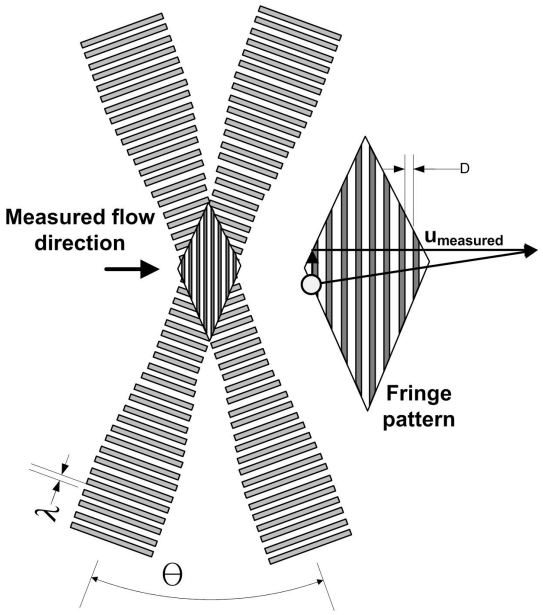

Figure 27: Fringe pattern

$$f_D = \frac{2sin\frac{\theta}{2}}{\lambda_b} u_{p\perp} \qquad (4.1)$$

Lagrangian acceleration measurement is a relatively new development in Laser Doppler Velocimetry (LDV) based systems. In 2001 Czarske et al. [22] introduced a novel two wavelength probe with a diverging fringe spacing. The setup features a high spatial resolution, allowing measurement of position and spatially resolved velocity directly. Lowe [61] describes an experimental approach for fully-resolved turbulence structural measurement and includes

[15] Usually referred to as Laser Doppler Velocimetry (LDV) or Laser Doppler Anemometer (LDA)

[16] More details on Laser Doppler measurement techniques can be found in related textbooks, for example the Springer Handbook of Experimental Fluid Mechanics edited by Tropea et al. [97], Laser Doppler and Phase Doppler Measurement Techniques published by Albrecht et al. [4] or Principles and Practice of Laser-Doppler Anemometry by Durst et al. [28].

new techniques for the direct measurement of particle acceleration and sub-measurement-volume-scale position resolution for 3 component LDV systems. Three component comprehensive LDV measurements therefore allow the direct determination of the Reynolds stress transport, the velocity–pressure gradient, the dissipation rate and the viscous diffusion in turbulent boundary layers and therefore give direct information about the production of turbulent kinetic energy. Lowe and Simpson [62] showed successful application of this technology for a two dimensional constant pressure turbulent boundary layer. From the digitized laser Doppler signal the instantaneous frequency and its change over time can be obtained [71].

The use of a one component LDV, as proposed for this project, simplifies the experimental effort and allows easy alignment for windtunnel entries. In a system with no fringe gradient the acceleration can be directly estimated from the change in frequency, as it has to be proportional to the change in velocity. This principle is shown in Figure 28 for the measurement of a particle through a shock wave.

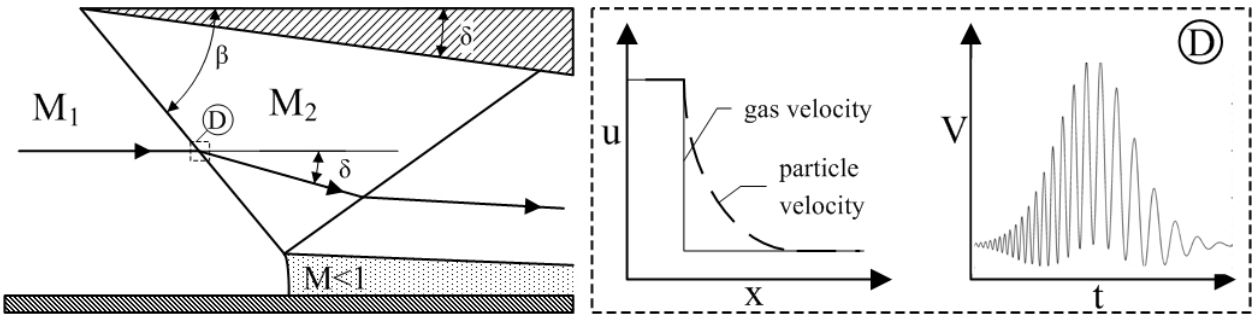

Figure 28: Principle of velocity gradient measurement

The fringe spacing is a function of the laser wavelength and the intersection angle of the beams and given in equation (4.2) [4].

$$d_{fr} = \frac{\lambda_b}{2sin\frac{\theta}{2}} \tag{4.2}$$

The number of fringes can be estimated from the beam waist width, the wave length and the beam intersection angle (compare eq. 4.3).

$$N_{fr} = \frac{4r_w}{\lambda_b} tan\frac{\theta}{2} \tag{4.3}$$

Not only the velocity but also the acceleration can be determined from the Laser Doppler equation.

$$\frac{dv}{dt} = f\frac{Dd_{fr}}{Dt} + d_{fr}\frac{df}{dt} \tag{4.4}$$

This equation in detail is written as:

$$\frac{dv}{dt} = v\,f\,\frac{dd_{fr}}{dx} + f\,\frac{dd_{fr}}{dt} + d_{fr}\,\frac{df}{dt} \tag{4.5}$$

Since the fringe spacing does not vary with time ($d\Delta x/dt = 0$) this equation simplifies to expression 4.6. It can be seen that the acceleration is scaling to the power of two with the flow velocity, but also the fringe spacing, the fringe spacing gradient and the chirp (df/dt) have a dominant influence.

$$\frac{dv}{dt} = v\,f\,\frac{dd_{fr}}{dx} + d_{fr}\,\frac{df}{dt} \tag{4.6}$$

4.1 Signal Model

Signal processing is an essential process for successful Laser Doppler Accelerometer measurements. For velocity measurement it usually involves burst recognition and spectral analysis in order to find the shifted Doppler frequency. Acceleration measurements can be realized with regular of the shelf LDV systems by upgrading to an advanced data reduction system (e.g.. Nobach et al. [71]). Signal processing of such chirped signals is complex and bounded by numerical errors. The Cramer–Rao lower bound (CRLB) is the theoretical minimal bound for signal processing related uncertainties as shown by Lowe and Simpson [62]. Bayer et al. [9] details the development of a signal model for a Laser Doppler profile sensor and explores its numerical boundaries and uncertainties for a Laser Doppler sensor developed at the Technical University Dresden.

In order to analyze the expected Doppler signals for the experimental investigation at hand, two simple signal model were developed and investigated with respect to available data processing techniques and their limitations. They are then also used to estimate the uncertainty of the measurement apparatus.

The signal is generated as a continuous sinoidal wave modulated onto a single carrier wave representing the gaussian burst due to the beam transit. The same gaussian wave is used to generate the beam signal intensity.

$$A(x) = \frac{1}{\sqrt{2\pi\sigma^2}} e^{-\frac{(x-\mu)^2}{2\sigma^2}} \tag{4.7}$$

The signal then can be created as shown in eq. 4.8 and pictured in figure 29. Note that

the beam intensity and carrier signal are a function of the flow coordinate, which with the huge velocity differences across a shock wave can lead to a non gaussian burst envelope. For the simulation purpose beam intensity and signal power is normalized to a magnitude of one.

$$s(t) = 0.5\,\mathrm{x}\left[\underbrace{A(x)}_{Carrier\,Signal}\ \mathrm{x}\ \underbrace{sin(\phi(t))}_{Doppler\,Signal} + \underbrace{A(x)}_{Beam\,Intensity}\right] + noise \tag{4.8}$$

The argument of the sin function is the instantaneous phase, which is directly related to the instantaneous frequency.

$$\phi(t) = 2\pi \int f(t)dt \tag{4.9}$$

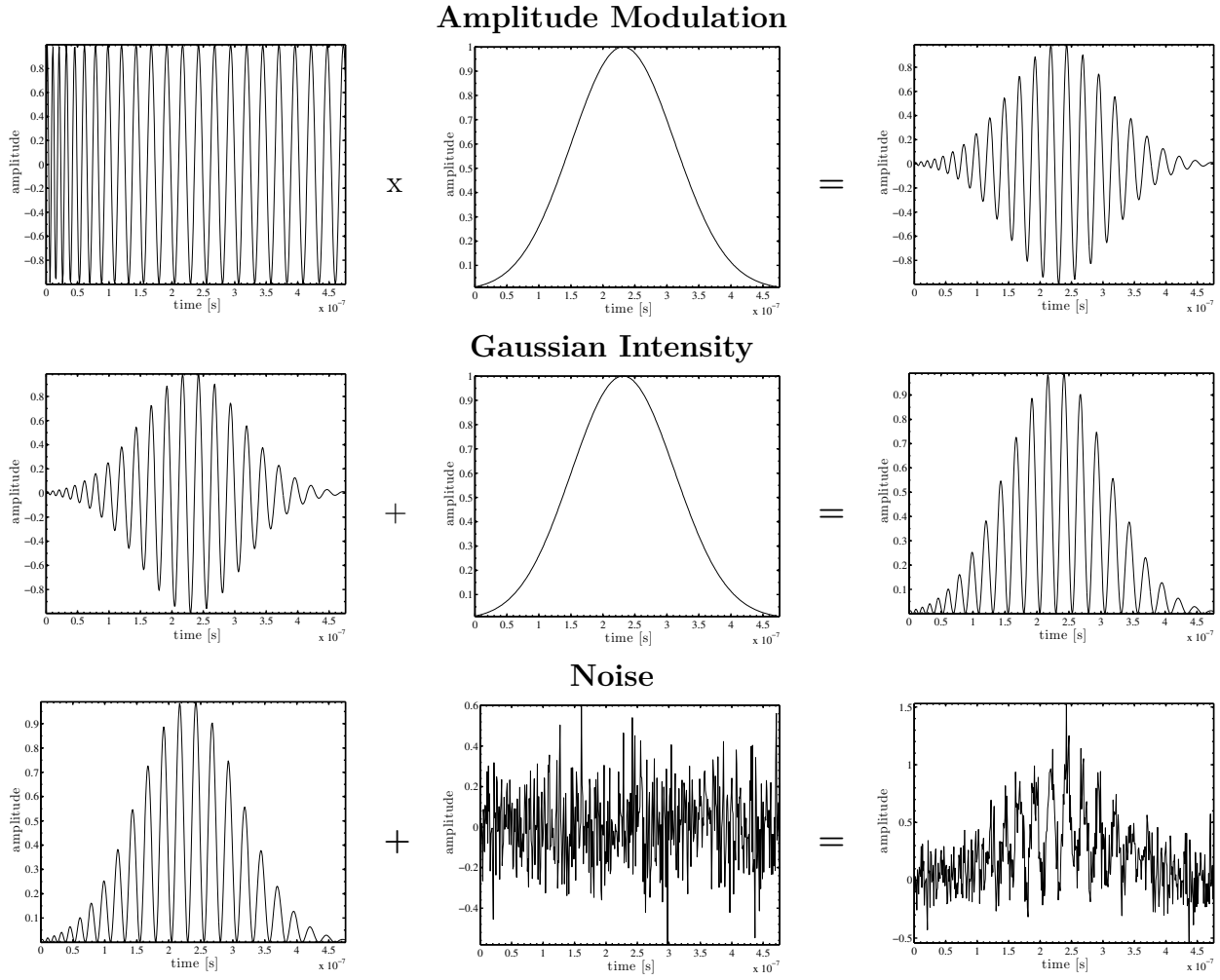

Figure 29: Signal Generation (5 db) for a 200μm probe volume

A very simple model representing a swift frequency change with constant frequency plateaus can be represented by using the atan function. This signal model will be referred to as the "simple" signal model.

$$f(t) = \left[\left(\frac{-atan((t-t_0)D)}{\pi} + 0.5\right)(u_1 - u_2) + u_2\right] d_{fr}^{-1} \tag{4.10}$$

The phase of the signal is the Integral of the the frequency times two pi. It can be obtained analytically for the simple signal model presented.

$$\phi(t) = \frac{t}{d_{fr}\pi}\left[(0.5\pi(u_1 - u_2) + atan(D(-0.5\,t\,u_1 + 0.5\,t\,u_2 + t_0u_1 - t_0u_2)\right] \tag{4.11}$$

Another signal model used was generated by using the Stokes drag model in order to more closely resemble the physics of an actual measurement with regards to signal length and chirp rate.

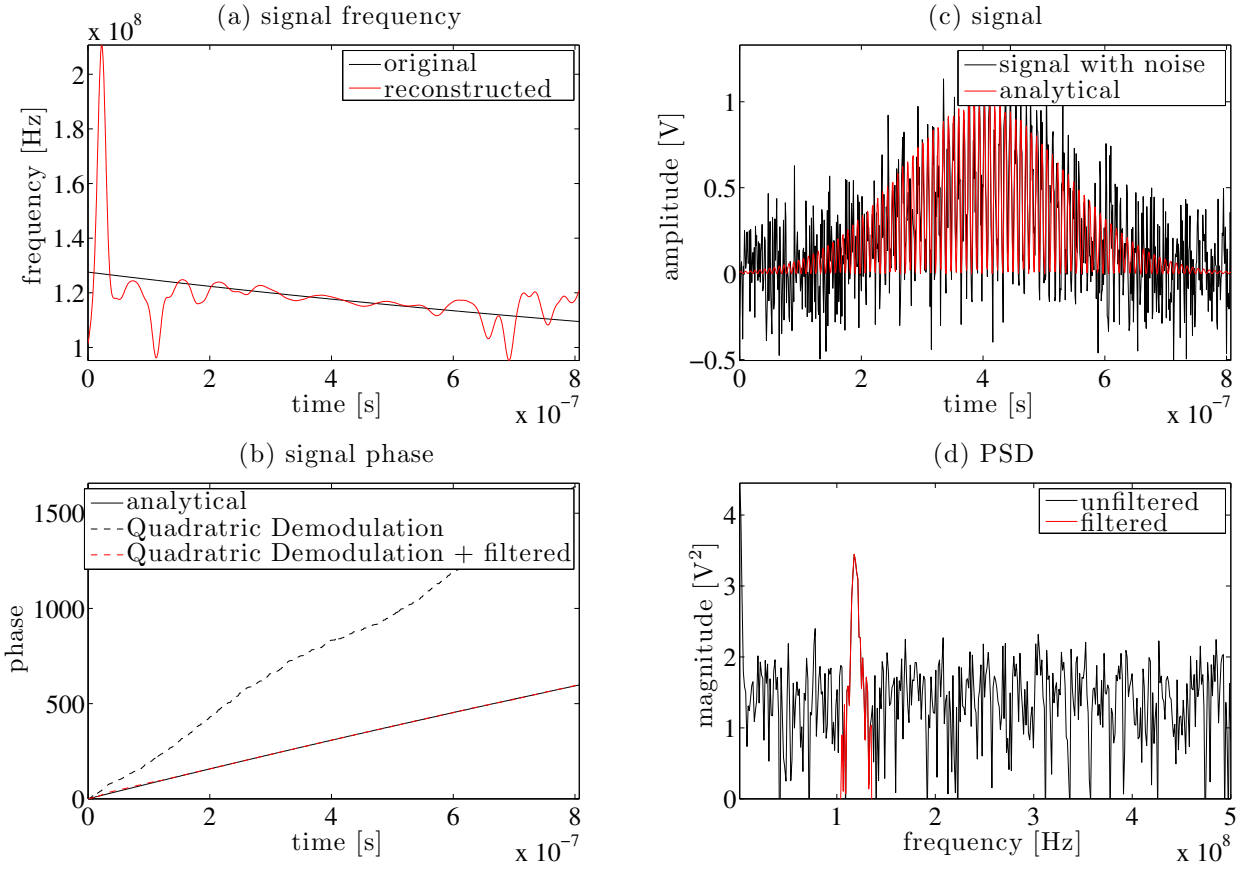

Figure 30: Stokes signal model using a Gaussian window (SNR_{1dB} =20 dB)

A representation of the Stokes model signal, showing the frequency, phase, Power Spectral Density (PSD) and the actual generated signal is found in figure 30. Interesting to note is the plateau in the frequency spectrum off the PSD between the two freestream velocities up and downstream of the shock wave.

4.1.1 Signal to Noise Ratio (SNR)

The ratio of the mean square of the signal to the variance of the noise commonly called "Signal to Noise ratio" (SNR) is used to classify the quality of the measured signal.

$$SNR = \frac{P_{sig}}{P_{noise}} \tag{4.12}$$

and alternatively the SNR in units of "decibel" dB:

$$SNR_{dB} = 10\, log_{10}\left[\frac{P_{sig}}{P_{noise}}\right] \tag{4.13}$$

For unbiased noise, the noise power equals its variance. Samples of model signals for different SNR are found in figure 33. An alternative definition (Shinpaugh et al. [89]) used for the Signal to Noise ratio inhibits the signal bandwidth in the calculation.

$$SNR_{dB1} = 10\, log_{10}\left[N\frac{P_{sig}}{P_{noise}}\right] \tag{4.14}$$

The local Signal to noise ratio is not always easy to estimate as the noise floor and the signal strength is not easily available. One method to employ is described by Tropea et al. [97]. It is based on the autocorrelation of the signal which only for zero time difference includes noise, as it is by definition incoherent and random.

$$A_r = \frac{R(n\Delta\tau)}{cos(2\pi f\, n\Delta\tau)} \tag{4.15}$$

$$\sigma_n^2 = R(0) - A_r \tag{4.16}$$

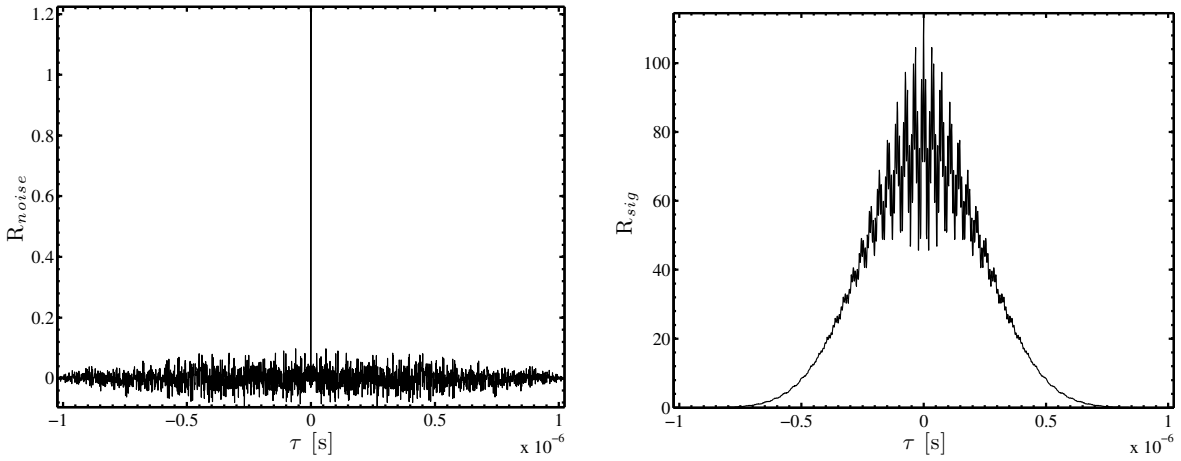

(a) Autocorrelation for Gaussian noise (b) Autocorrelation for a noisy signal

Figure 31: Autocorrelation for SNR estimation

Figure 32 shows the local Signal to Noise ratio of a simulated signal as a function of time and compares the true value to the estimated SNR. A Gaussian window is used as a weight function for the local SNR. The results are consistent and promise reliable SNR prediction which could be used to weight or exclude parts of the signal during signal processing.

$$SNR_{dB} = 10\,log_{10}\left[\frac{A_r}{\sigma_n^2}\right] \tag{4.17}$$

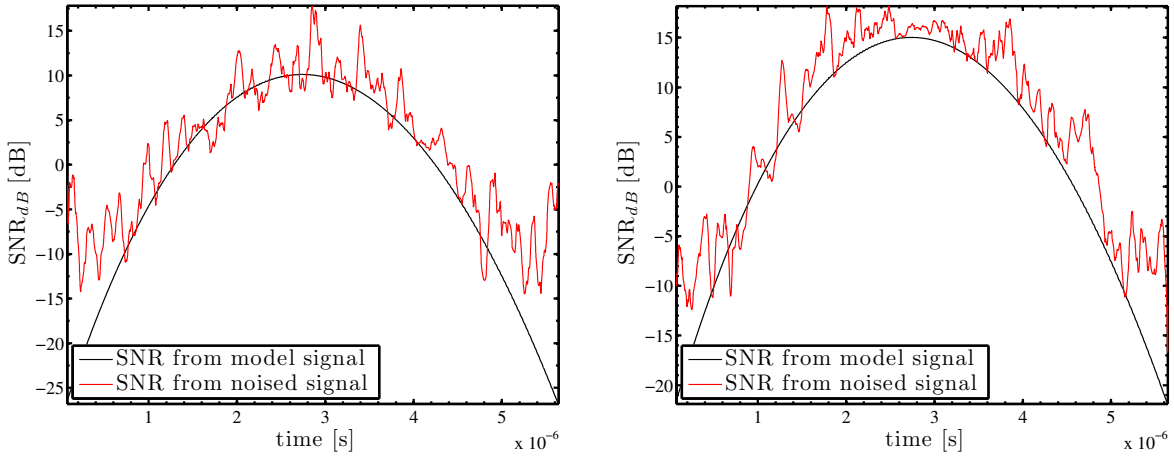

(a) Local SNR for a SNR=5 dB signal (b) Local SNR for a SNR=10 dB signal

Figure 32: Local SNR for two example signals

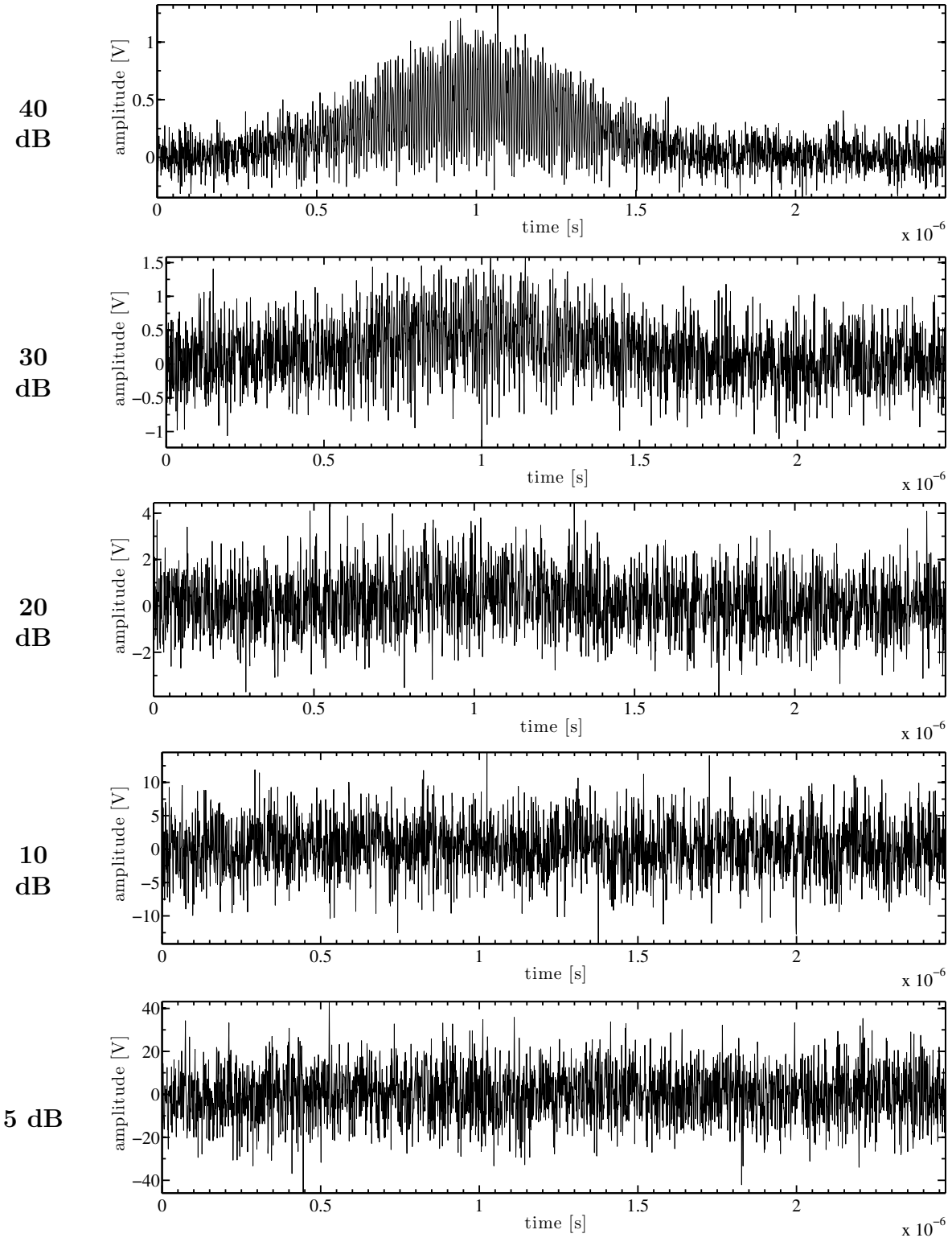

Figure 33: Several simulated bursts with different SNR_{1dB}

4.2 Spectral Distribution of Noise

Most signal models used for uncertainty estimation assume Gaussian noise. The property of Gaussian noise is its bandwidth independent distribution, which means that noise is equally present in all frequencies. Figure 34 shows examples of simulated bursts with Gaussian noise.

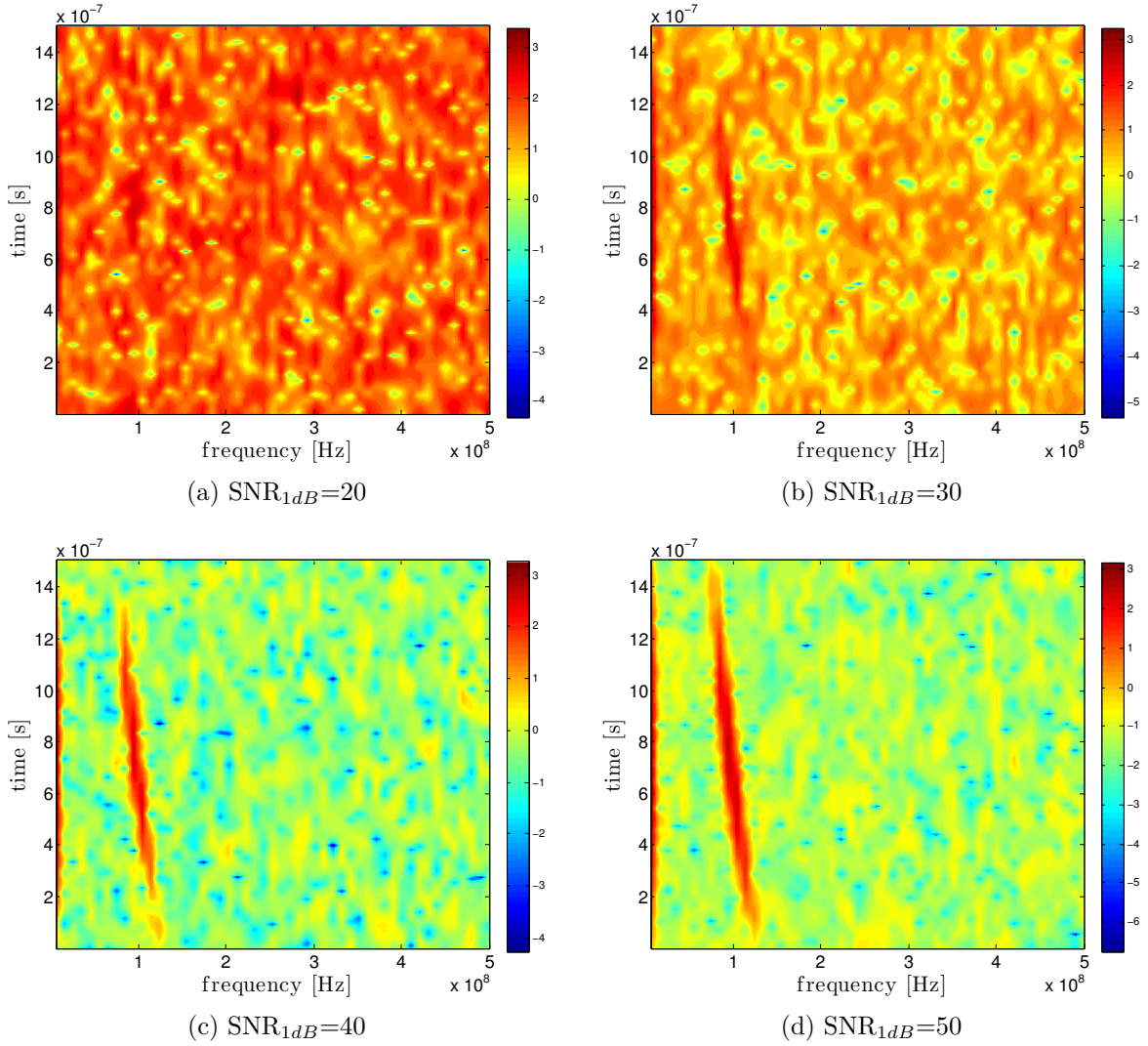

(a) SNR_{1dB}=20 (b) SNR_{1dB}=30

(c) SNR_{1dB}=40 (d) SNR_{1dB}=50

Figure 34: Spectrograms for the Stokes model for several SNR

Lowe [61] showed that signal noise is not necessarily white - white being the “worst case scenario” , but time dependent as is the signal strength. Therefore the effect of alternative noise compositions on the estimation process should be considered and will affect uncertainty estimation. Figure 4.2 shows spectrograms of measured bursts. The non Gaussian distribution, with higher noise energy in the lower frequencies is noticable.

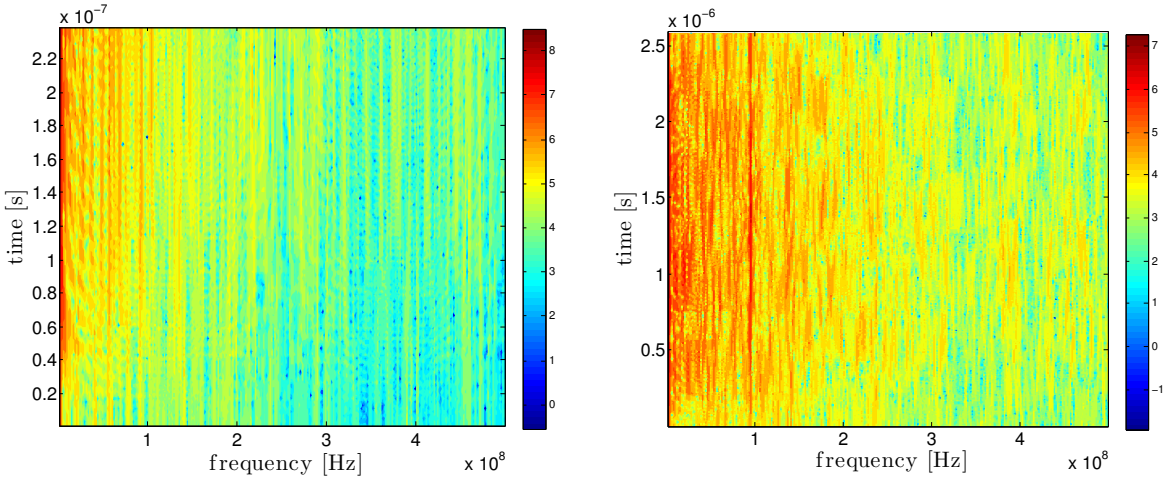

(a) SNR_{1dB}=20 (b) SNR_{1dB}=25

Figure 35: Spectrograms of measured bursts

4.3 Data Reduction Techniques

Several ways to obtain physical quantities from the Laser Doppler signal exist. Commonly used estimation schemes are: the (1) Quadrature Demodulation Technique (QDT) using the (1) Hilbert transform (HT) , (2) signal model based optimization and the (3) sliding fast Fourier Transform (FFT) .

4.3.1 Quadrature Demodulation (QDT)

The quadrature demodulation technique (QDT) was introduced for the processing of chirped Laser Doppler signals by Lading and Andersen [56] and Czarske et al. [21] and has been used and validated in several publications [22, 20, 9, 69] thereafter.

The technique is based on the estimation of the phase angle from the complex signal. The complex signal is hereby denoted as:

$$z(t) = Ae^{j\phi(t)} \tag{4.18}$$

or in terms of in-phase and quadrature phase component as a pair of two real terms for one instant in time [63]:

$$z(t) = A\,sin(\phi(t)) + j\,A\,cos(\phi(t))$$

or as a general expression:

$$z(t) = y(t) + i\,\mathcal{H}(y(t)) \tag{4.19}$$

where $\mathcal{H}$ symbolizes the Hilbert transform, a transformation which can be used to obtain the analytical signal from a real signal.

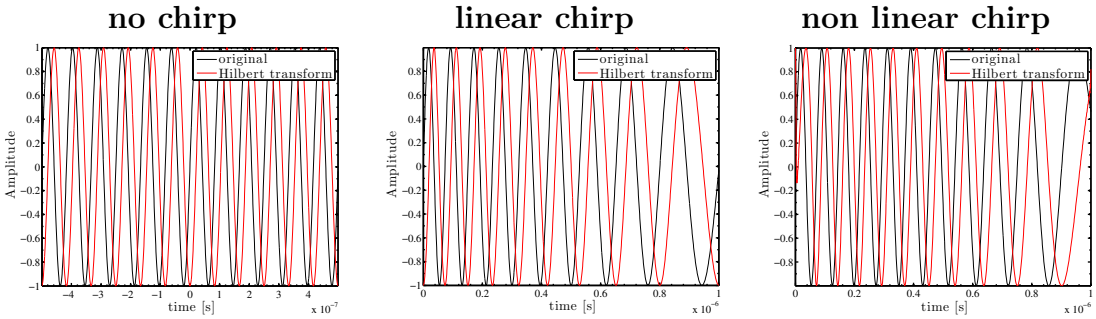

Figure 36: In phase and Quadrature phase components of some signals

The phase angle can then be calculated as the arctan of the imaginary and the real part of the signal. As the arctan function is only defined in the interval of $\pm\pi/2$, the obtained

signal phase must be unwrapped in order to be continuous. The QDT process is described in figure 37.

$$\phi(t) = \arctan\left(\frac{\mathcal{H}(y(t))}{y(t)}\right) \tag{4.20}$$

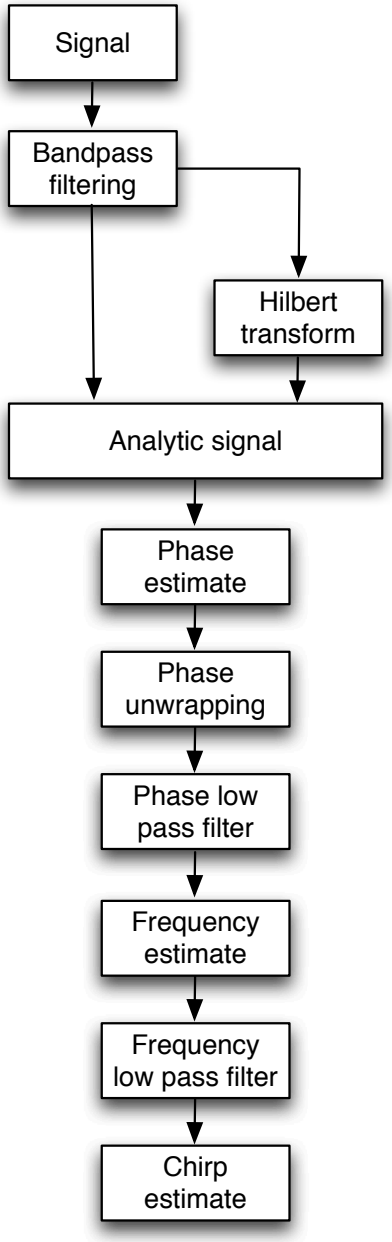

Figure 37: Quadrature Demodulation Technique

The Hilbert transform has several limitations, one of which is described by the Nuttal theorem. The theorem states that the Hilbert transform not always gives the correct quadrature component necessary to obtain unity of signal on the unit circle[17] (Huang and Attoh-Okine [42]). A proposed tool to overcome the Hilbert transforms drawbacks for unsteady and nonlinear signals is the Hilbert-Huang transformation, which is better suited for data interpretation than for data reduction. A small study on commonly encountered sinoidal signals [18] was performed to evaluate the HT's usability. The results are displayed in figure 39. One can see that regions with the highest reconstruction area are the beginning and end of the signal. The nonlinear signal has higher errors compared to the linear chirp signal. Compared to a signal model using the Stokes particle approximation through the shock it can be seen that this last computation has a much lower error. This can be explained by its higher frequency being closer to the Nyquist frequency where the Hilbert transform works the most reliably. Also end effects at the beginning and end of the data sequence due to the nature of the Hilbert transform being based on FFT is noticeable. Therefore longer sequences are favorable when processing using the HT.

Figure 38 iterates on the signal recovery dependance on the sampling rate. It is observant that at least the Nyquist sampling frequency has to be reached in order to allow semi accurate signal recovery, which is consistent with theory. However a sampling frequency at least three times the maximum frequency is required to reach the lowest RMS error.

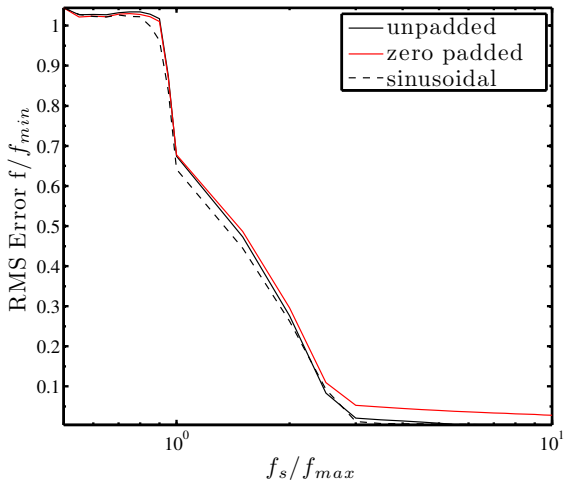

Figure 38: Dependance of signal recovery on sampling rate for a linear chirp

[17] basically the Hilbert transform does not always reach a perfect 90 degree shift
[18] no envelope

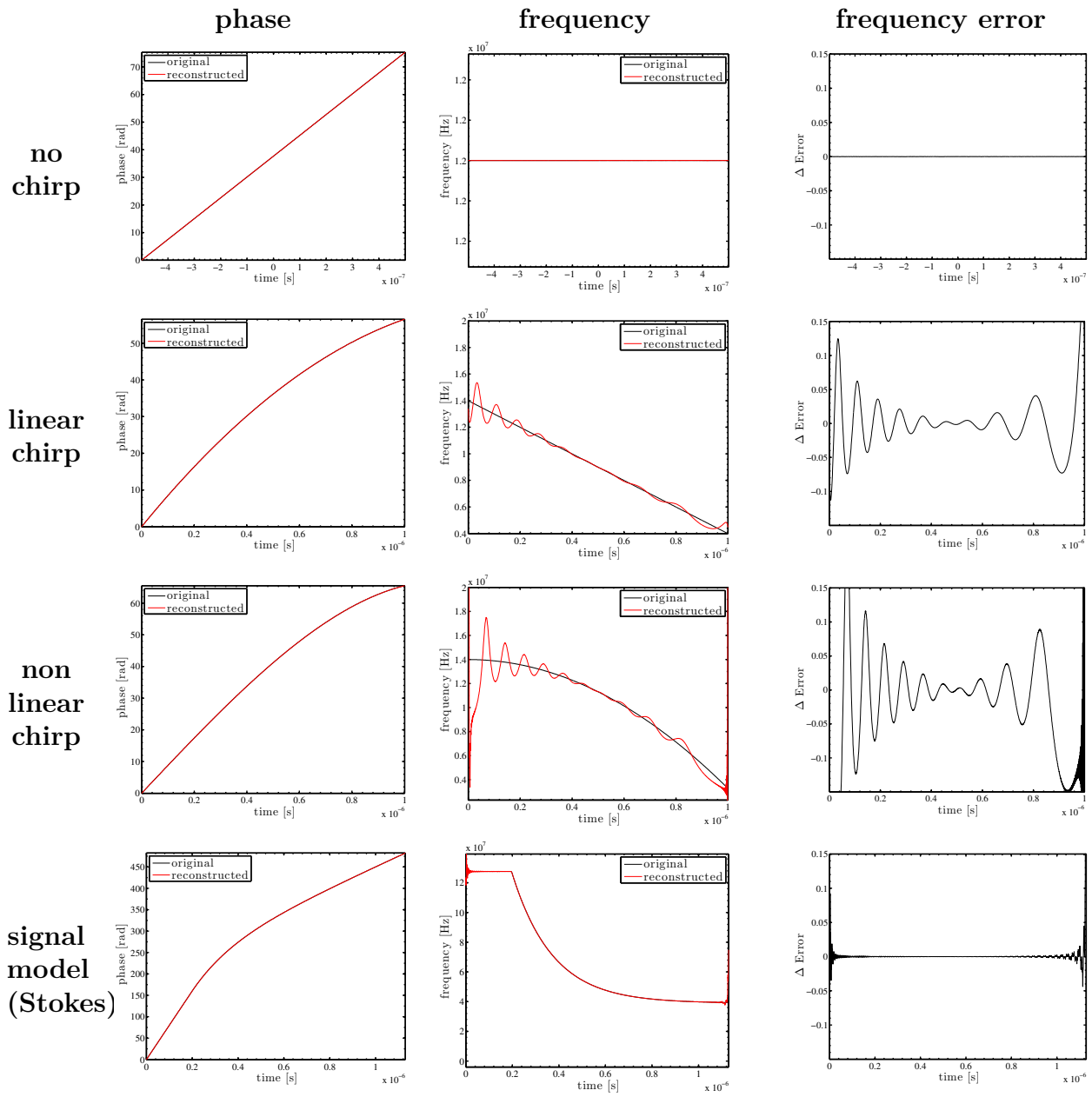

Figure 39: Hilbert Transform (HT) study on various signal types

The local SNR has a strong influence on the success of the recovery of the frequency from the phase information by Quadratic Demodulation. This explains the scatter at the beginning and end of the reconstructed frequency and recommends to define a window of trust based on the local SNR number as described in the previous chapter.

4.3.2 Iterative Optimization of Signal Model

Nobach et al. [71] used a "complex, analytic, harmonic signal of constant amplitude" and correlated it to the signal measured. An optimization algorithm was then used to maximize the correlation and to obtain the frequency and chirp of the signal. Iterative estimation for the strong nonlinear signals expected proved difficult and no successful approach could be implemented. Therefore the focus was shifted towards QDT and Sliding FFT approaches.

4.3.3 Sliding FFT

Fast Fourier transforms are often used in Laser Doppler signal processing. For chirped signals an averaging effect [57] due the sliding signal window is present. Shinpaugh et al. [89] discussed the different interpolation schemes for obtaining the Doppler frequency from the spectrum and concluded that Gaussian interpolation allows to obtain lowest uncertainties close to the CRLB.

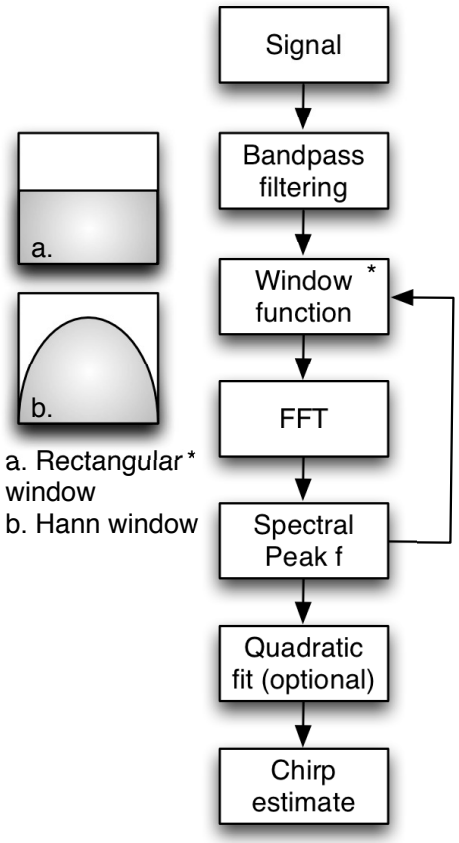

Figure 40: Sliding FFT Process

Therefore in all following comparisons and plots the Gaussian interpolation method is

the method referred to. It may be noted that these uncertainties are for unchirped constant frequency signals whereas the signals discussed here are in general nonlinear and non stationary, leading to higher overall uncertainties.

Figure 40 details the numerical process referred to as sliding FFT. It be taken into account that the sliding process reduces the effective bandwidth dependent Signal-to-Noise ratio and therefore increases the uncertainty of the estimation process. This leads to a tradeoff between uncertainty and dynamic response. Different signal windows can increase the dynamic response as well. The signal is normalized using the amplitude information obtained from the Hilber transform and the signal window applied.

$$SNR_{1dB(effective)} = 10\,log10(10^{\frac{SNR_{1dB}}{10}}\frac{N_{window}}{N})$$

In figure 41 different variants of the FFT (for a nonlinear signal) are compared: FFT with rectangular window, FFT with Hann window[19] . As can be seen clearly, zero padding improves the estimation process clearly once a certain signal to noise ratio is reached (for this type of signal a SNR_1 of at least 50 dB is required to reach CRLB). Only with zero padding all variants discussed reach CRLB. The variant with the quadratic fit gives slightly better results at lower SNR but naturally is outperformed by all other variants at high SNR.

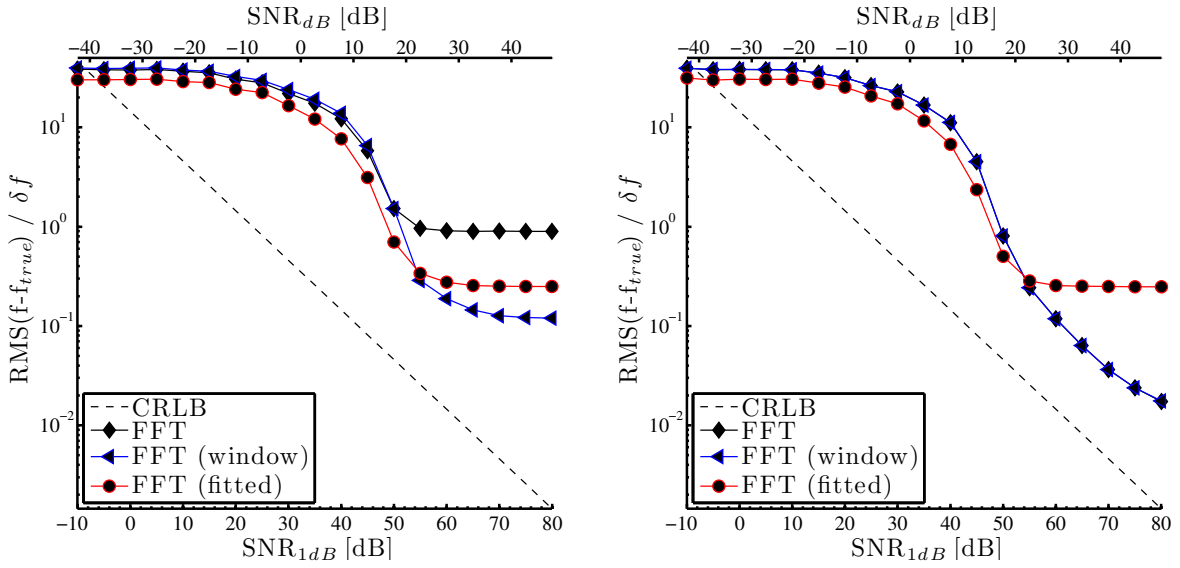

(a) no zero padding (b) with zero-padding (K=800)

Figure 41: Sliding FFT comparison of numerical uncertainty

[19]labeled as FFT (window)

4.4 Uncertainty Analysis

4.4.1 Cramer-Rao Lower Bound (CRLB)

The Cramer-Rao Lower Bound (CRLB) is a measure of the numerical uncertainty [97, 4]. For a "perfect" signal processing code the estimated value equals the true value. However, no numerical algorithm is truly perfect, but always bound by numerical errors and limited by the Signal to Noise ratio (SNR) of the data. The theoretically smallest variance of an unbiased estimator is given by the Cramer-Rao Lower Bound. Comparison of the signal processing estimation for a known signal to the CRLB allows to determine the efficiency of the algorithm and the influence of noise on the signal processing.

The CRLB for a model signal, function of the single parameter a and noise is as follows:

$$\sigma_a^2 \geq \frac{1}{E\left[\left(\frac{\partial \, ln \, p(s,a)}{\partial a}\right)\right]} \tag{4.21}$$

For the case that the signal is dependent on several parameters, the variance can be found by the inverse of the Fisher information matrix J.

$$J_{ij} = E\left(H_{a_i} H_{a_j}\right) = -E(H_{a_i a_j}) \tag{4.22}$$

where $H_{a_i} = \left(\frac{\partial \, ln \, p(s,a_i)}{\partial a_i}\right)$

$$\sigma_a^2 \geq \left(J^{-1}\right)_{ij} \tag{4.23}$$

Assuming uncorrelated,signal independent, Gaussian noise with the power σ_n^2 the Fisher information matrix simplifies to expression eq. 4.24 [97].

$$J_{ij} = \frac{1}{\sigma_n^2} \sum_{k=0}^{N-1} \left(\frac{\partial m_k}{\partial a_i} \frac{\partial m_k}{\partial a_j}\right) \tag{4.24}$$

This expression can be found and solved for its inverse numerically, for both the analytical and numerical model signals. In order to improve the CRLB estimation the signal is first oversampled to obtain more accurate gradients and then down-sampled to the required sampling rate. The resulting CRLB estimate is then compared to the analytically obtained CRLB. The rise in error may be explained by some kind of aliasing due to oversampling. The difference between the analytical and computed is the lowest for a oversampling rate three times higher than the targeted sampling rate.

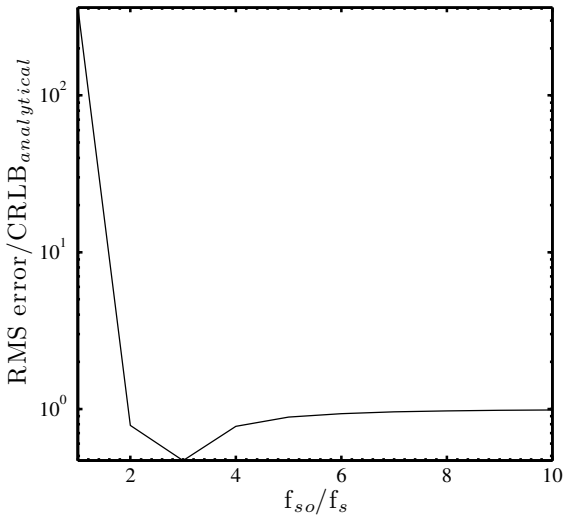

Figure 42: Oversampling-Downsampling technique for CRLB estimation

4.4.2 Estimator Uncertainty

In this study the uncertainty of the estimator is explored. The computed uncertainty of several estimation methods for at least 200 simulated bursts is averaged and compared to the CRLB of the signal. In figure 43 and 44 the uncertainties for a burst of constant frequency are computed as a reference. A more detailed study for frequency estimation of constant frequency signals using several estimator approaches and interpolation schemes is given by Shinpaugh et al. [89].

As can be seen for both figures, the uncertainty for a burst without pedestal reaches lower values (see in comparison examples of burst with pedestal in figure 33 on page 50). The FFT estimator with Gaussian interpolation comes close the CLRB but does not reach it completely as it is reported by Shinpaugh et al. [89] and Lowe [61]. This might be attributed to differences in the signal model used. The QDT technique, which operates in the time domain is much more sensitive to noise and does not come close in uncertainty to the FFT based estimators for practical signal to noise ratios. The uncertainties are given with respect to spectral line width and the true frequency known from the signal model. The estimator uncertainty for processing of Stokes model type of bursts (nonlinear, with strong accelerations present) is shown for frequency estimation and chirp rate estimation in figure 45 and 46 respectively.

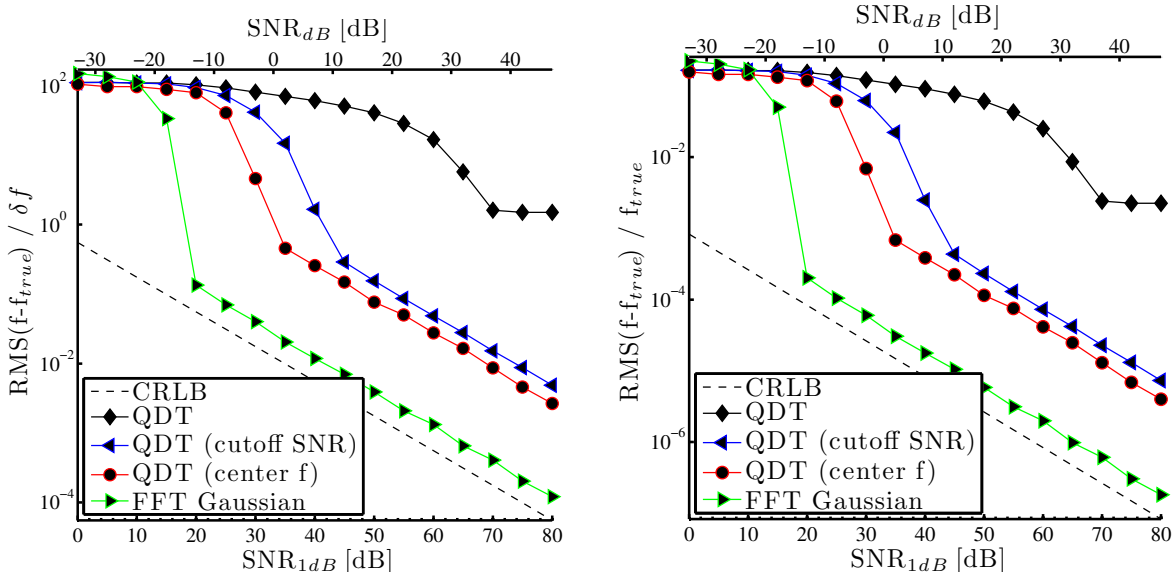

(a) Frequency uncertainty normalized by the spectral line width

(b) Frequency uncertainty normalized by the true frequency

Figure 43: Data processing uncertainty for constant frequency bursts (no pedestal burst)

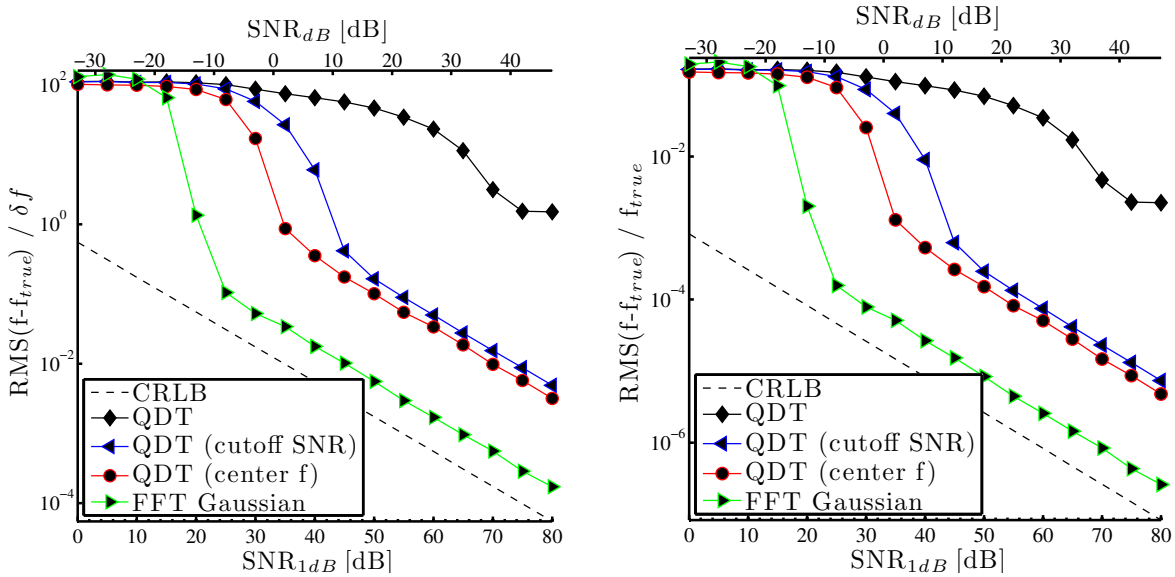

(a) Frequency uncertainty normalized by the spectral line width

(b) Frequency uncertainty normalized by the true frequency

Figure 44: Data processing uncertainty for constant frequency bursts (with pedestal burst)

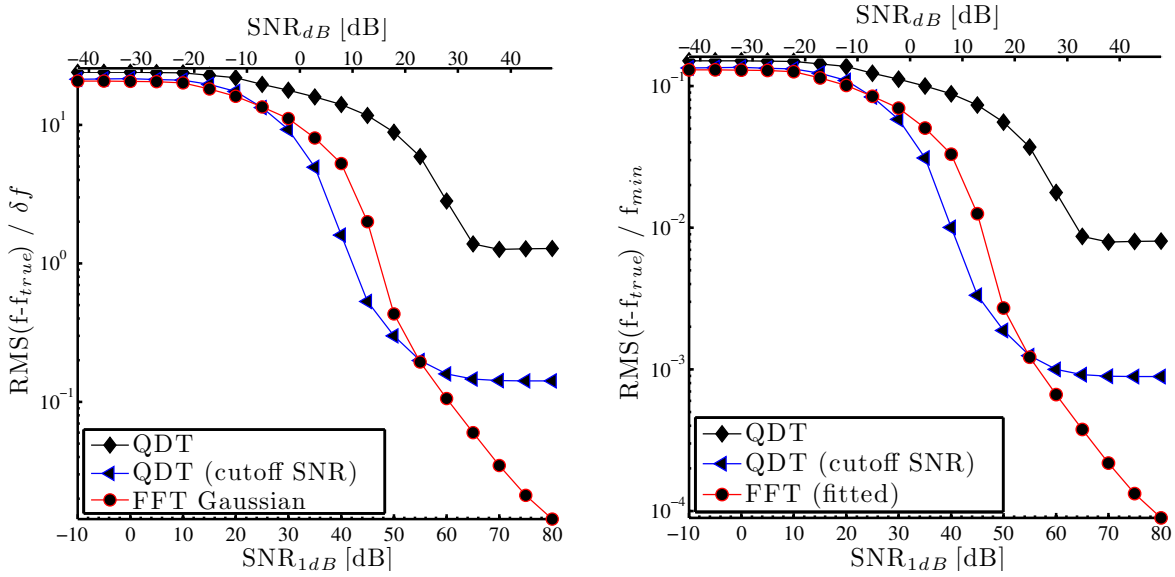

(a) Frequency uncertainty normalized by the spectral line width

(b) Frequency uncertainty normalized by the true frequency

Figure 45: Data processing uncertainty of the frequency estimator for nonlinear bursts

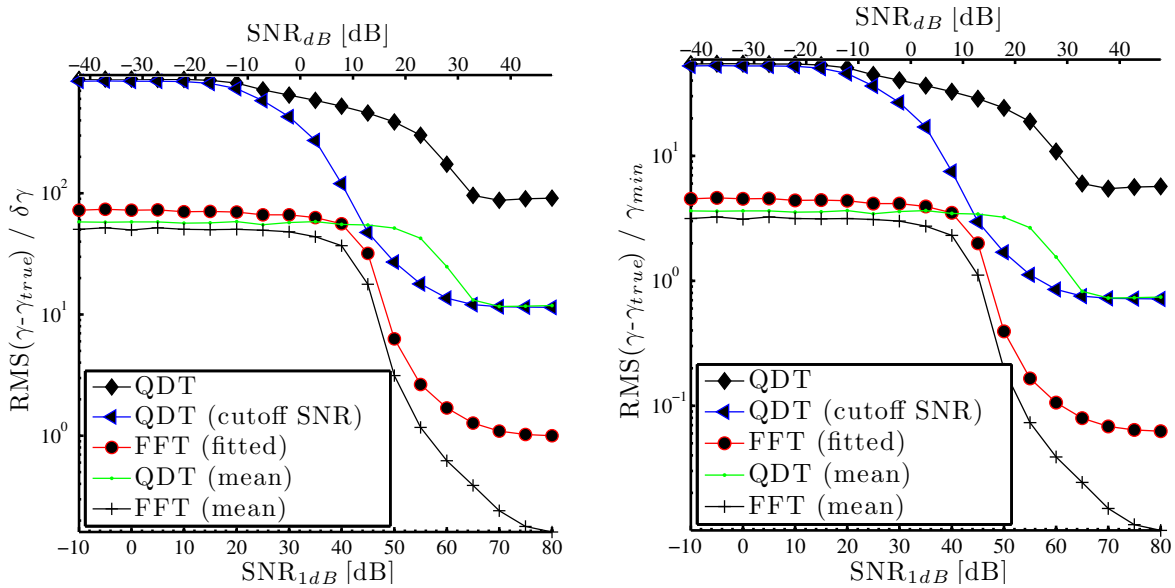

(a) Frequency uncertainty normalized by the spectral line width

(b) Frequency uncertainty normalized by the true frequency

Figure 46: Data processing uncertainty of the chirp estimator for nonlinear bursts

4.4.3 System Uncertainty

An estimate of the uncertainties of a measurement system is not only important for the design but also for interpretation and confidence in the actual measured quantities. If the uncertainties are too high, the design of the instrument or the experiment needs to be modified in order to allow meaningful measurement.

Considering the system as a transfer function $y = f(x_i)$ dependent on i=1,2...,n independent variables, the sensitivity of the system can be described by the sum of linearized Taylor series of the single independent variables [26]. In the case of an uncertainty analysis, this change Δx_i can be considered the uncertainty u_i of a single system component.

$$\Delta y \approx \frac{\partial f}{\partial x_i} \Delta x_i \tag{4.25}$$

The uncertainty of the system can therefore be estimated by equation (4.26) (please note that the indices's follow Einstein's sum notation).

$$\Delta_y \approx \sqrt{\left(\frac{\partial f}{\partial x_i}\delta_i\right)^2} \tag{4.26}$$

This linear approximation can be used to determine appropriate component uncertainties. The method of equal effects considers an equal contribution of each component to the overall uncertainty and allows determination of the desired uncertainty for each single component. If one component does not full-fill this requirement, the desired uncertainty can still be reached by compensating with lower uncertainties of the other components.

$$\mu_{xi} \approx \frac{U_y}{\sqrt{n}\dfrac{\partial f}{\partial x_i}} \tag{4.27}$$

The uncertainty of the velocity therefore is:

$$\Delta_v \approx \sqrt{\left(d_{fr}\,\delta_f\right)^2 + \left(f\,\delta_{d_{fr}}\right)^2} \tag{4.28}$$

Applying this analysis to the case of acceleration (eq. 4.6) measurement, measurements yields following uncertainty:

$$\Delta_a \approx \sqrt{\left(\left(f^2\frac{dd_{fr}}{dx} + \frac{df}{dt}\right)\delta_{d_{fr}}\right)^2 + \left(d_{fr}\,\delta_{df/dt}\right)^2 + \left(d_{fr}\,f^2\delta_{dd_{fr}/dx}\right)^2} \tag{4.29}$$

Parameters

f	$100\text{x}10^6$	Hz
BC	$350\text{x}10^6$	Hz
Gamma	$-4.27\text{x}10^6$	Hz^2
Uncertainty freq. Estimation	1 %	
Uncertainty chirp Estimation	20 %	
Fringe gradient (from freestream calibration)	$-1.0\text{x}10^5$	
Fringe gradient uncertainty	47 %	

Velocity

Bias error	9.7750	m/s	equals	1.97 %
Non Bias error	0.8775	m/s	equals	0.18 %
Total error	9.8143	m/s	equals	1.97 %
Acceleration				
Bias error	$1.3983\text{x}10^5$	m/s^2	equals	2.8 %
Non Bias error	$1.0221\text{x}10^6$	m/s^2	equals	28.3 %
Total error	$1.0316\text{x}10^6$	m/s^2	equals	28.4 %

Table 10: Uncertainty Analysis for realistic sample signal

It can be seen from this equation that for the trivial case of no acceleration the uncertainty does not go to zero. Also the uncertainty is directly dependent on the flow velocity and the (local) chirp, so for higher flow velocities and strong accelerations the measurement uncertainties can be considerably higher. It is also noticeable that the uncertainty of the fringe spacing indirectly goes into this equation by the power of two, so that measurement uncertainties for accelerations measurement must suffer from higher bias uncertainties than velocity measurements. The high acceleration uncertainties are mainly a result of the chirp estimator uncertainties influencing the calibration uncertainties. In table 10, the uncertainties for a signal with a relative high chirp are given. This example is directly applicable to the signal and flow properties of Laser Doppler Accelerometer measurements in this study. For high SNR the acceleration uncertainty can be greatly reduced.

5 Experiment & Instrumentation

The experimental part of this thesis seeks to perform measurement using a new kind of Laser Doppler Accelerometer with an unique spatial range and to obtain low Reynolds number, high Knudsen number acceleration data of particle lag behind a shock wave. This acceleration data is valuable for particle lag estimation in flows with slip and transition effects as they naturally exist in supersonic experimental facilities.

The *in situ* calibration of the fringe spacing and determination of the fringe vector and the beam angle is described in section 5.3.3. The lag measurements were performed far above the influence of the boundary layer in the freestream portion of the shock wave, on the flow direction centerline of the shock generator.

5.1 Experimental Facilities

The goal of this work is to perform a study on commonly used seeding materials for supersonic particle based measurements and to obtain low Reynolds number slip and transition flow drag data using a newly developed instrument. Important considerations for the design of the experimental setup lay in consideration of intended experimental data. If one considers the thermodynamic properties necessary for slip and transition flow regimes around micro particles the need for very low temperatures in the test section becomes clear. Only the hypersonic and supersonic windtunnels have a shielded test section where such conditions can be obtained. Since this study is also intended to prepare for future work on turbulent boundary layer measurements in the supersonic facility, the SSWT is chosen as the experimental site.

A very good description of the facility can be found on the website of the department of Aerospace and Ocean Engineering:

"The Virginia Tech 23 x 23 cm supersonic/transonic wind tunnel was designed and originally constructed at the NASA Langley Research Center. The air pumping system consists of an Ingersoll-Rand Type 4-HHE-4 4-stage reciprocating air compressor driven by a 500 hp, 480V Marathon Electric Co. motor. The compressor can pump the storage system up to 51 atm. A drying and filtering system is provided which includes both drying by cooling and drying by absorption. The settling chamber contains a perforated transition cone, several damping screens, and probes measuring stagnation pressure and temperature [1]."

The nozzle chamber is interchangeable and will be housing the newly designed two-dimensional contoured M=2.0 nozzle block shown in figure 49[20] [12]. The plenum pressure

[20]Design by Dr Byun

typically used for the SSWT experiments is about 25 PSI and the total temperature is, depending on environmental conditions at about 300 K.

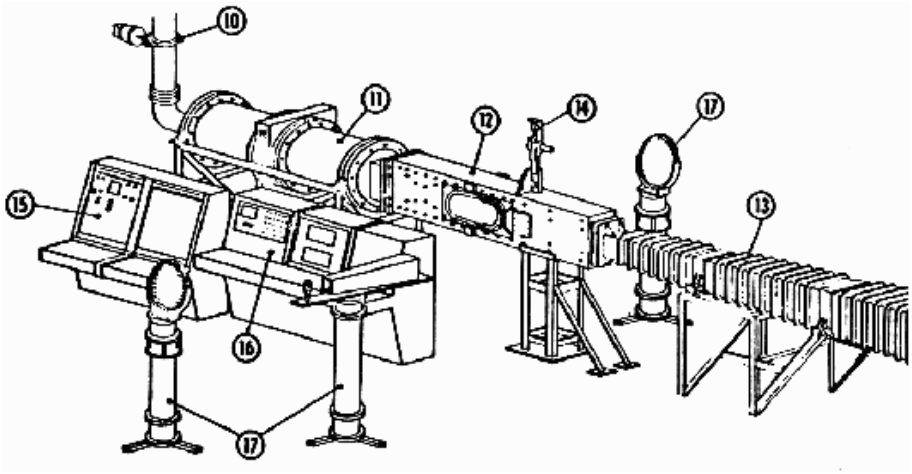

Figure 47: Supersonic Windtunnel layout. 10-Pressure Regulator, 11-Settling Chamber, 12-Test Section, 13-Diffuser, 14-Model Support and Drive System, 15-Tunnel Control Panel, 16-Measurement Panel, 17-Schlieren Apparatus (Virginia Tech AOE information *[1]*)

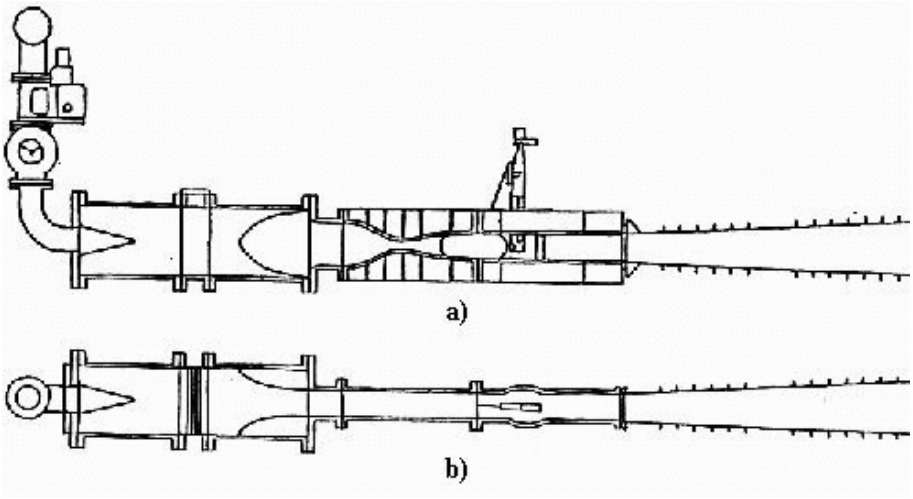

Figure 48: a. side view, b. top view (Virginia Tech AOE information *[1]*)

The shock generator consists of a 30 degree wedge mounted on a rod, fitted into a vertically moveable holding assembly (shown as position 14 in Figure 47) and is inserted from an opening in the top of the windtunnel. 3 different rods allow the change of angle of attack of the wedge and therefore facilitate different shock angles. For the experiment a -5 degree angle of attack rod is chosen to obtain a 10 degree turning angle.

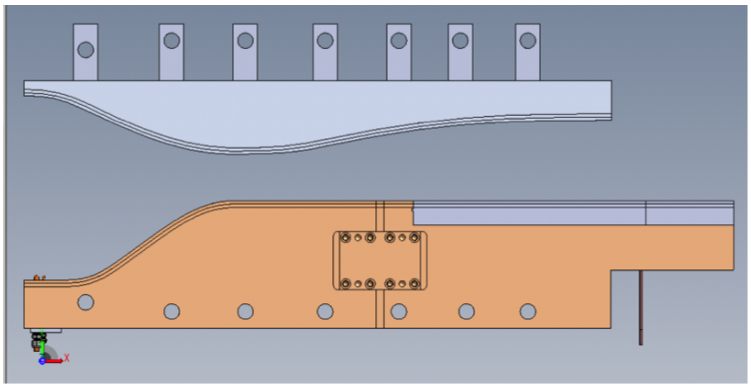

(a) M=2.0 nozzle side view

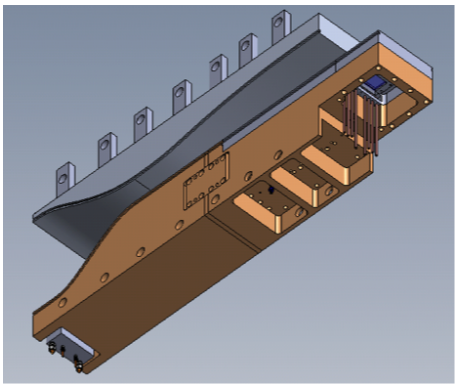

(b) M=2.0 nozzle 3 D view

Figure 49: Nozzle block

5.1.1 Schlieren Photographs

Schlieren photography is a visualization method based on the fluid density, hence refractive index of the fluid.

A simplified equation covering this "density - refractive index" relationship is the Gladstone-Dale equation [97]. It relates the fluid density to the refractive index. or CCD.

$$n - 1 = K\rho \tag{5.1}$$

Essential for the Schlieren method is a knife edge placed in the focal plane of the receiving system, which pictures the the test section on a film negative. As can be seen from eq. 50, which shows the light intensity for a Schlieren picture for gas flows, the recorded light intensity is a function of the density gradient normal to the knife edge aperture used [97].

$$\frac{\Delta I}{I} = \frac{K f_2}{a} \int_{\xi_1}^{\xi_2} \frac{\partial \rho}{\partial x} dz \tag{5.2}$$

Schlieren photographs from the M=1.95 (design Mach number is 2.0) nozzle with the wedge in different angles of attack are shown in Figure 50. Close examination reveals a light parasitic shock in front of the wedge caused by an optical access window in the flooring of the test-section. Also it can be seen that the 15 degree and 20 degree (corner angle) shock constellations seem to be very straight and steady, in opposition to the 25 degree corner angle which features a very curved shock. The shape as well as the pressure ratio of above 2.5 indicate unsteadiness due to boundary layer separation for that largest turn angle. At the downstream edge of the wedge Prandtl-Meyer expansion fans are clearly visible, as well as the reflection of the initial shock from the floor-plate.

α_{AOA}	0°
θ_{top}	15°
θ_{bottom}	15°
M_1	2.0
M_{2top}	1.44
$M_{2bottom}$	1.44

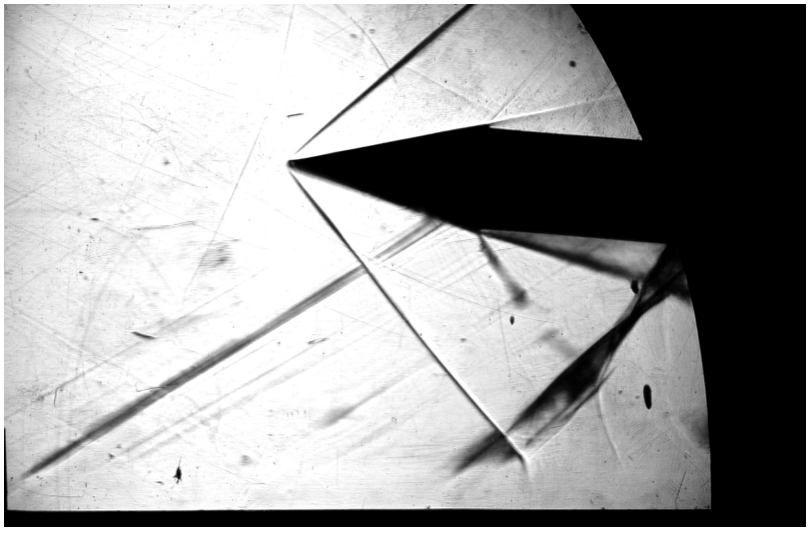

α_{AOA}	5°
θ_{top}	10°
θ_{bottom}	20°
M_1	2.0
M_{2top}	1.64
$M_{2bottom}$	1.21

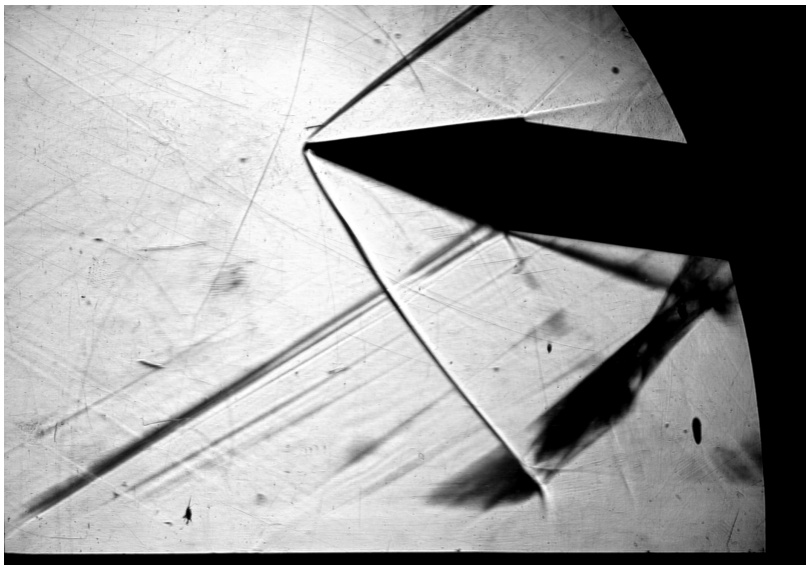

α_{AOA}	10°
θ_{top}	5°
θ_{bottom}	25°
M_1	2.0
M_{2top}	1.82
$M_{2bottom}$	1.73

Figure 50: Schlieren photographs of the SSWT wedge constellations

5.2 Instrumentation & Probe Design

The depth of penetration is determined by the focusing lenses and the intersection angle of the two beams and gives the distance for which the instrument can be used. The depth of penetration is typically dependent on the purpose of the experiment and the optical access possible. Miniature LDVs can be used to measure flow quantities from a very close location inside the object of interest (e.g. boundary layers) or allow optical access to windtunnels with space constraints. The optical access, including window thicknesses or transfer axes need to be taken into account as well.

Because the test section of the supersonic windtunnel ($23\,x\,23\,cm$) is the largest to consider, the depth of penetration is set to a distance in which at least a fourth of the height or width is accessible. Allowing some space for transfer and optical access, a depth of penetration of about $10 - 15\,cm$ is chosen. The final depth of penetration is dependent on the geometric restrictions due to lens sizes that limit the angle of intersection.

In order to estimate the required length of the elongated measurement volume calculations of a relevant seed particle passing through a oblique shock wave were performed. The choice of the length of the measurement volume is basically balancing the trade off of spatial resolution to the signal to noise ratio of the measurement. From particle drag computations performed beforehand it can be seen that a measurement volume length of about 2 mm would be sufficient to cover a big part of the particle trajectories. However if the signal to noise ratio allows, a longer volume would be desirable to cover the complete trajectories of bigger particles.

Design parameter		
Depth of penetration	L	$\geq 10 - 15\,cm$
Fringe spacing	D	$\geq 1.0\,\mu m$
Spatial range	L_V	$\sim 2\,mm$
Angle of intersection	θ	$19.75° \leq$

Table 11: Preliminary design parameters

The fringe spacing is the most essential parameter for the acceleration measurement techniques, as the size and number of fringes directly influence spatial resolution and uncertainty of the instrument. The intersection angle was chosen to give a fringe spacing bigger than the range of particles($0.35\mu m \leq d_p \leq 1.0\mu m$) investigated.

The newly developed design of a one component LDV uses cylindrical lens elements to obtain a non Gaussian beam-shape and an elongated measurement volume in the flow direction. This configuration gives a stream wise measurement volume length of about 2mm

and allows the recording of the particle trajectory as well as the determination of shock location.

5.2.1 Bench-top Design

During the course of this project various designs were developed. However due to time constraints and the need for an effective and cost efficient design for this novel spatial resolution a bench-top design was favored. [21] The designs are shown in figure 54 on page 73. The findings gained from the bench-top design then could be used to obtain a better layout for more specific and specialized experiments.

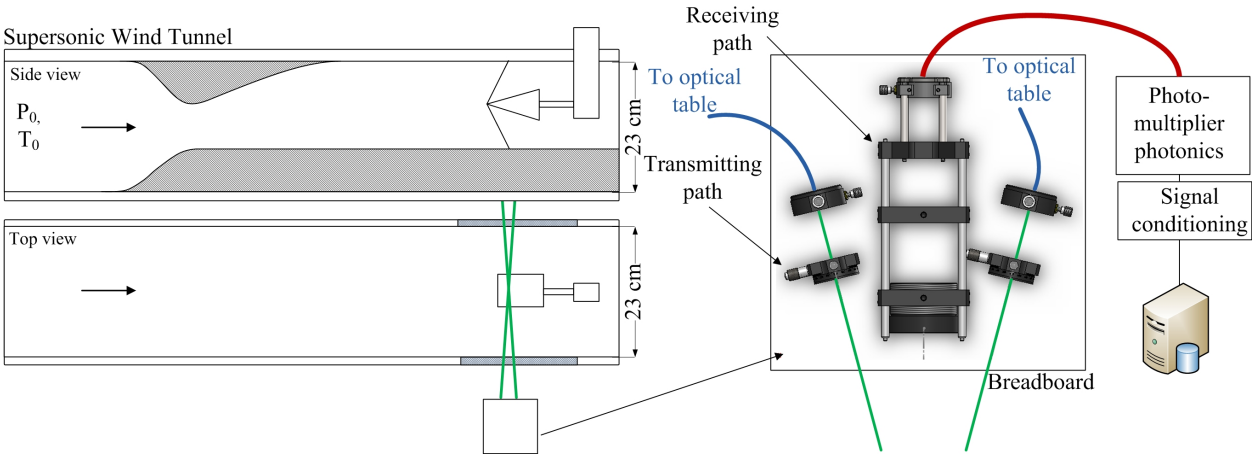

Figure 51: Layout of the one component velocity gradient measurement system

The bench-top design houses all optical components of the probe on a 12 x 12 inch breadboard plate by Thorslabs. It is similar to the 3 design pictured in figure 54, only that it has no custom base plate and instead uses breadboard type parts. The components of the receiving parts, employing a backscatter system are in the center and surrounded by the two transmitting beam assembly groups. The receiving assembly consists of a 60 mm Thorslabs cage system. The cage system holds two 2" spherical lenses, focusing the backscattered light into an 800 μm ST terminated multimode fiber. The focal length of the front lens is 250 mm. The front lens is mounted in a threaded lens holder and can be moved in the z coordinate. The assembly is held by two steel posts and mounted on an axis to allow change in the vertical (y) coordinate. A schematic is pictured in figure 51 and a photograph of the unit is shown in figure 52 on the following page.

[21] The third design already shows these influences in the choice of components

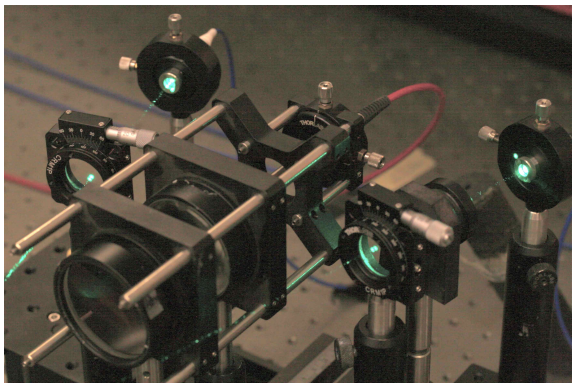

Figure 52: Probe (close up)

Design parameter	
Transmitting Optics	
Focal length Cylindrical lens	300 mm
Receiving Optics	
Focal length Cylindrical lens	250 mm
Effective operation parameters	
Depth of penetration	180 mm
Width	350 mm
Height	350 mm
Fringe spacing	1.17 μm

Table 12: Actual instrument features and dimensions

The transmitting assemblies consist of a Thorslabs rotational lens mount PRM1 and an adjustable focus collimating lens assembly of type Thorslabs CFC. The lens mount holds an 1" cylindrical lens with a focal length of 300 mm. The collimating lens assembly is connected to the optical table by an 12 foot length 8 μm diameter FC terminated single-mode polarization maintaining fiber. Similarly to the receiving assembly, both transmitting assemblies are mounted on steel posts and connected to a z and y stage. This allows adjustment of the probe.

5.2.2 LDV Setup SSWT

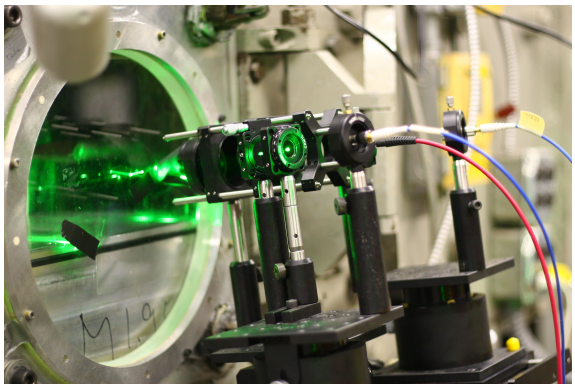

(a) Bench-top design (Photograph)

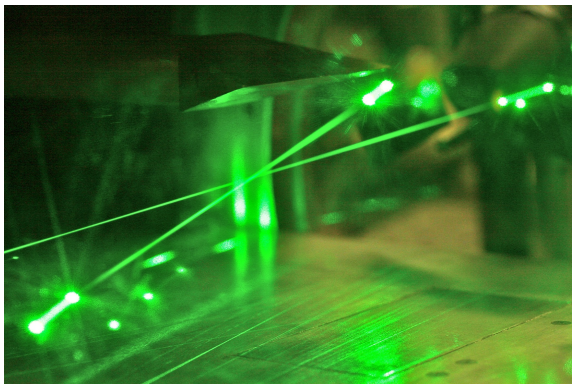

(b) Test section (Photograph)

Figure 53: Photographs of the probe and test section

The complete one component velocity gradient measurement system consists of the optical table, the probe, the receiving probe and the signal processing and data reduction apparatus. The setup on the optical table is relatively simple, it only includes the Coherent Verdi solid state laser set on single mode output at 532 nm with about 1 W power, a rotating polarizer, a set of mirrors and two fiber optic launchers. A 350 MHz Bragg cell is used, to create fringes moving in the flow direction. The advantages of this method are not only a reduction in bandwidth necessary to process the data, but especially a reduction of the chirp uncertainty that scales with the frequency. Figure 53 shows the probe installed and the measurement section in the windtunnel.

5.2.3 Data Processing

For data processing of the SSWT data the following steps are applied: (1) Burst Recognition using a modified and speed optimized variant of the Burst Recognition code[22] developed by Lowe [61]. Then (2) the extracted and frequency filtered burst windows are analyzed using a (3a) FFT based spectral estimator for mean frequency and (3b) sliding FFT and Quadrature Demodulation Techniques.

Examples of recorded bursts from SSWT measurement are shown in figure 55 on page 74 for different SNR. One can see that the typical transit time is about 3 microseconds, which gives an estimate of 1.45 mm for the length of the measurement volume.

[22] no envelope forcing

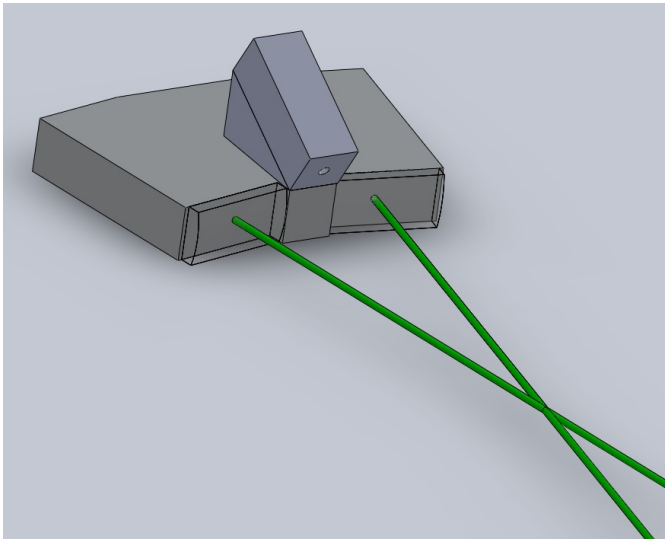

(a) 1. design

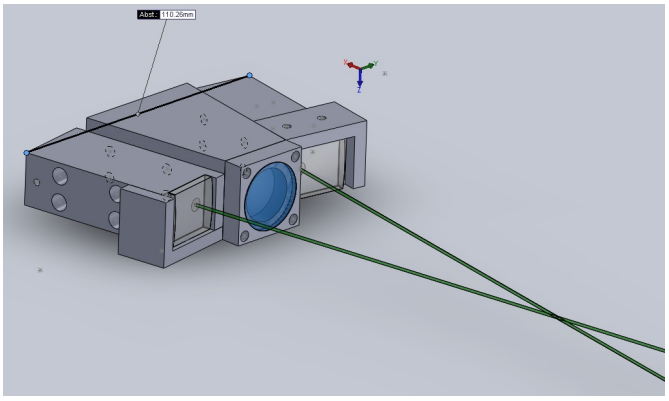

(b) 2. design

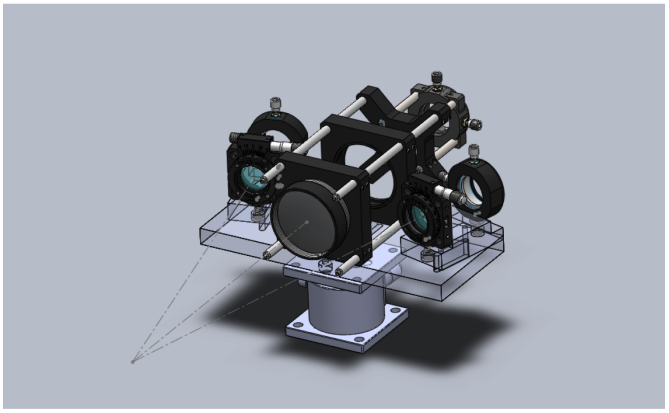

(c) 3. design

Figure 54: CAD designs for optimized setups

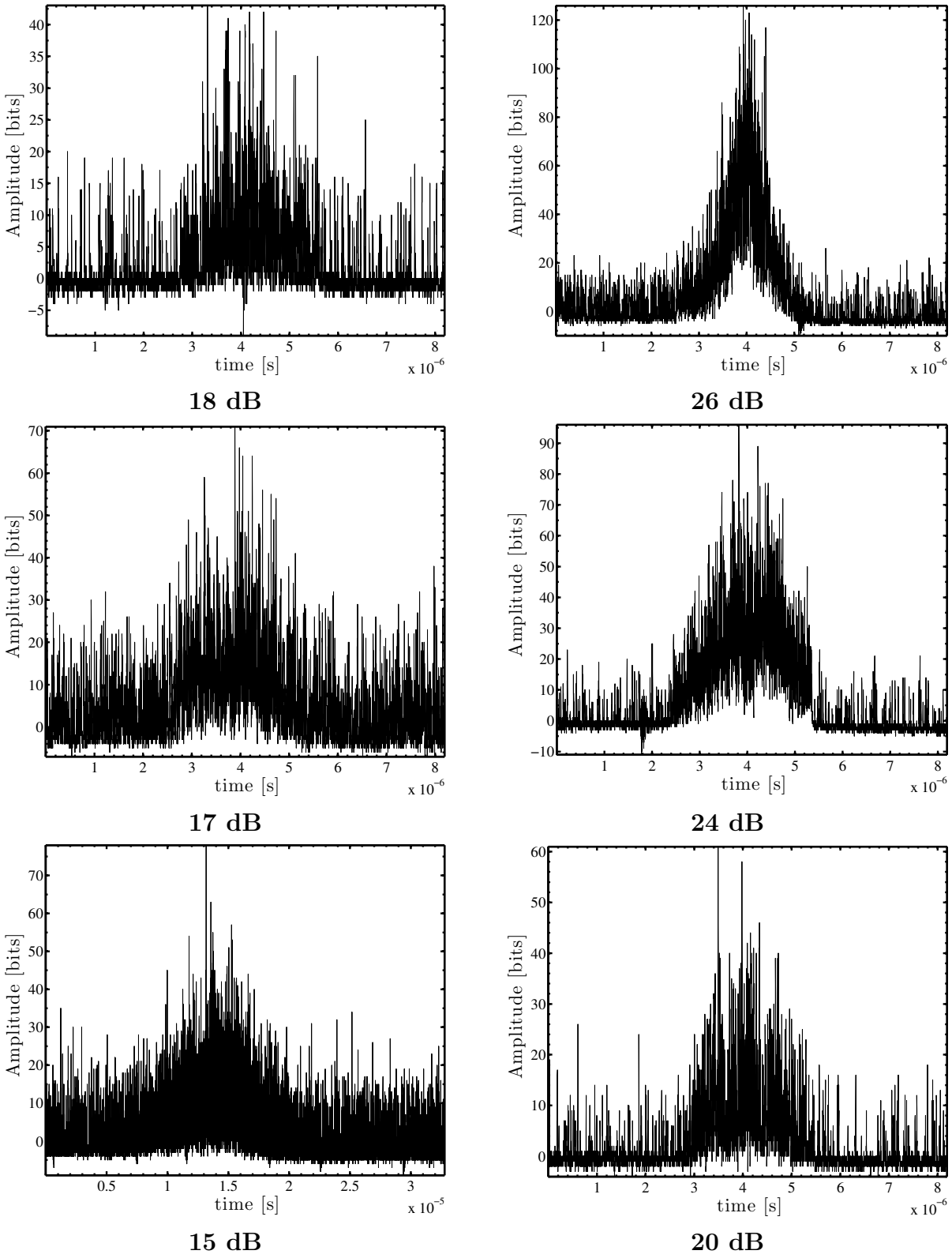

Figure 55: Several measured bursts with different SNR_{1dB}

5.3 Calibration Measurements

5.3.1 Fringe Visualization

The quality of alignment of the beams and the fringe visibility the can be analyzed from fringe visualizations. A microscope lens is used to project the measurement volume onto a screen. From these observations the unique spatial resolution becomes obvious. The fringe spacing was determined to be about 1.17 μm from beam angle geometry. Figure 56 shows two photographs of the fringes observed from the actual measurement setup in the SSWT.

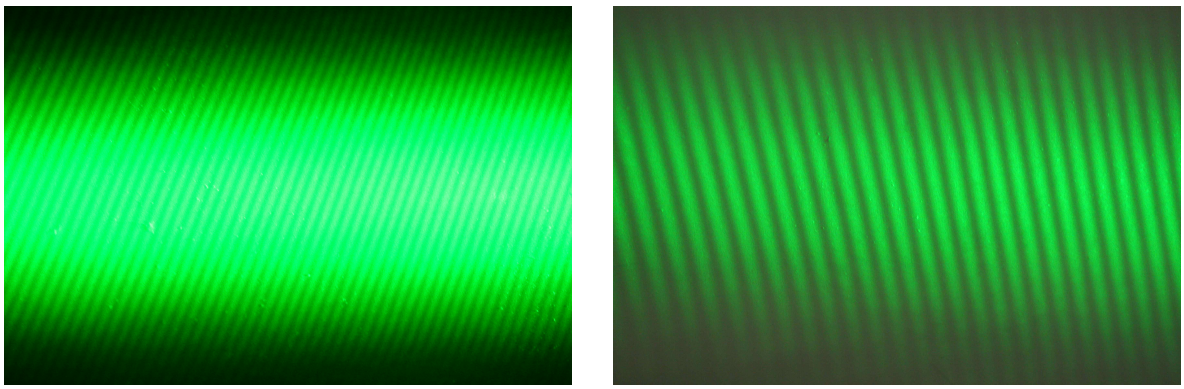

(a) about 10-20% of the theoretical measurement volume fringes

(b) close up

Figure 56: Photograph of the fringe pattern projection

5.3.2 Mean Fringe Spacing

In order to determine the exact fringe spacing the new probe a calibration measurement needs to be performed. Tests were undertaken in a small blow down wind tunnel as shown in Figure 58a on page 78. The tunnel consists of several 4" diameter acrylic tube section powered by shop air. Inlet flow conditioning is achieved using honeycomb style flow alignment tubes and meshes to remove cross-flow velocity gradients, axial velocity gradients and to create more isotropic turbulence.

The optical setup for this bench-top experiment is displayed in Figure 57. The setup on the optical table is simple, it includes one Coherent Innova 90 Arg+ laser set on single mode output at 514.5nm, a 40MHz Bragg cell, several sets of mirrors and two fiber optic launchers. An etalon is used to obtain a longer coherence length. The Laser output power is about 0.6 W. The fiber launchers focus the beams into 9.0 μm (9/125) diameter single mode polarization-preserving fibers which transmit the light to the probe optics mounted on a 12" x 12" breadboard. More on the optical layout can be found in section 5.2.1 on page 70.

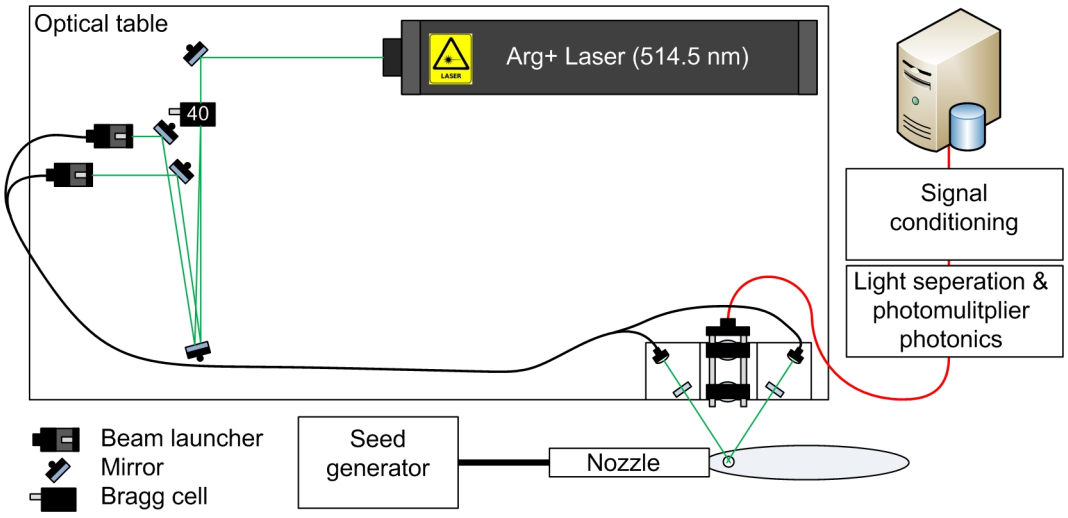

Figure 57: Optical setup calibration

The receiving multimode fiber is 800 μm in diameter and connects the receiving system to the photomultiplier. The fringe spacing for this particular setup is determined from geometrical parameters and is about 1.1 μm. To obtain a reading of the calibration velocity a small pitot probe is placed in the potential flow core of the jet. The dynamic pressure is measured with a differential Dwyer® Durablock® Series 250-AF gauge which has an uncertainty of ± 1.0% of the full scale. A barometer is used to measure the atmospheric pressure with an uncertainty of ± 0.05 mbar. The temperature is measured with a Mastech MS8229 multimeter (uncertainty of ± 5.0% of reading or ± 3°C) and a K thermocouple, to allow calculation of the flow velocity from the dynamic pressure measured by the pitot probe.

$$u_f = \sqrt{\frac{2\,p_{dyn}}{\rho_f}}$$

where the fluid density can be obtained from the universal gas law:

$$\rho = \frac{p_{stat}}{RT} \tag{5.3}$$

The measurement uncertainty of the calibration velocity is therefore:

$$U_y \approx \sqrt{\left(\frac{\partial f}{\partial p_{stat}} u_{p_{stat}}\right)^2 + \left(\frac{\partial f}{\partial p_{dyn}} u_{p_{dyn}}\right)^2 + \left(\frac{\partial f}{\partial T} u_T\right)^2} \tag{5.4}$$

Substituting the respective derivatives one obtains following equation for the measurement uncertainty:

$$U_y \approx \sqrt{\left(0.5\,\frac{p_{dyn}\,R\,T}{p_{stat}^3} u_{p_{stat}}^2\right) + \left(0.5\,\frac{R\,T}{p_{dyn}\,p_{stat}} u_{p_{dyn}}^2\right) + \left(0.5\,\frac{p_{dyn}\,R}{T\,p_{stat}} u_T^2\right)} \tag{5.5}$$

To evaluate the nozzle performance and its characteristics the nozzle velocity for different shop air pressures is measured. As can be seen from Figure 58b the relationship between pressure and velocity is relatively linear. The measurement uncertainty decreases with rising pressure as the term containing the dynamics pressure derivative has the biggest influence as can be seen from order comparison ($p_{stat} > p_{dyn}$). Therefore calibration measurements at highest nozzle speeds are desirable.

Limiting factor is the particle seeding required for the calibration measurement. First a pressurized pot with an array of 5 medical nebulizers and a PSL/Alcohol/Water mixture is tried. Unfortunately this setup did not produce enough burst necessary for successful measurement. Instead a Laskin nozzle atomizing Olive-oil is used for particle generation, high pressure air was bypassed to generate higher fluid velocities.

The preliminary data of 30,000 bursts is analyzed using an advanced burst recognition code developed by Lowe [61]. The frequency data was filtered leaving a data bandwidth ranging from 20-40 MHz. The dynamic pressure measured with the Pitot probe was 117.055 N/m^2, the static pressure was 0.94845 $10^5 N/m^2$ and the temperature was 21 degree C.

The mean velocity resulting from this pressure measurement is 14.4317 $\pm$ 0.3081 m/s. The data has a nearly Gaussian distribution, a mean frequency is 26.58 MHz and a standard deviation of 1.77 MHz. The mean fringe spacing can be determined to be 1.0754 $\pm$ 0.023 μm, which is in close agreement to the geometrical determined fringe spacing of 1.1 μm. This simplified experimental setup without fringe scanning is pictured in Figure 58a.

Because the first preliminary measurement suffered from a poor sample size of good Laser Doppler Signals and low power of the signals, several methods are used to improve the experimental setup: (1) The path length is optimized in order to give a better coherency length, (2) the Polarization of the two beams is optimized using a rotatable polarizer, (3) the optical alignment is checked and improved. The particles for this second preliminary experiment are generated using a Laskin nozzle, atomizing DOP. These measures greatly improved the sample size of valid bursts, also the signal power of the bursts was improved.

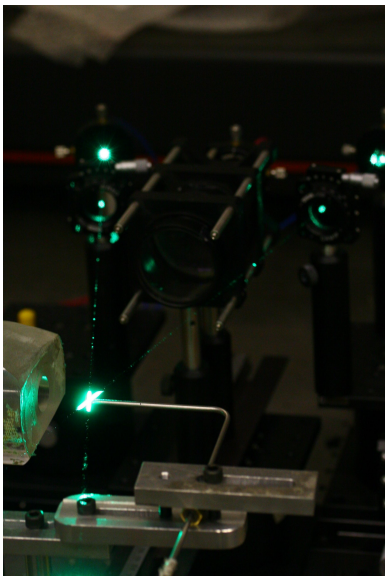

(a) Calibration nozzle with pitot probe and instrument probe

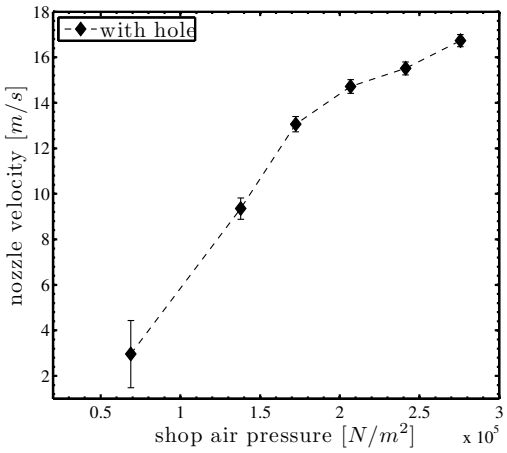

(b) Performance of the calibration nozzle

Figure 58: Calibration nozzle

The mean frequency from this measurement is 54.851 MHz, the mean fringe spacing is 1.1784 ± 0.017 μm. The change from the first measurement can be explained by the much higher sample size and the change in alignment which could lead to larger fringes.

It is assumed that the back-scattering and therefore the signal power level is roughly dependent on particle sizes. Therefore the frequency distribution for several ranges of power levels are compared. It is seen that the the mean frequency virtually is independent of power level, from this is concluded that the frequency is independent of particle size and no velocity lag due to inertial effects is present. Therefore the nozzle flow is sufficient for calibration measurements.

5.3.3 Freestream Calibration in the SSWT

In order to allow the freestream calibration in the SSWT, first the beam angles have to be determined after probe adjustment. For this purpose the distance of the incoming and outgoing beam spots

from a reference position in the test section is measured. From these vectors the angle between the two beams as well as the fringe vector, which indicates the alignment of the probe with the windtunnel coordinate system can be found easily. The beam vector is given as $\overrightarrow{b_i}$, where i denotes beam one or two.

$$\overrightarrow{b_i} = \begin{pmatrix} b_{i1} \\ b_{i2} \\ b_{i3} \end{pmatrix}, i = 1, 2$$

The angle between the two beams can be found from following expression:

$$\theta = acos\left(\frac{\overrightarrow{b}_1 \cdot \overrightarrow{b}_2}{|\overrightarrow{b}_2||\overrightarrow{b}_2|}\right) \tag{5.6}$$

The fringe vector is defined as the vector perpendicular to the fringes of a beam pair. For a perfectly aligned system the normalized fringe vector would be equivalent to the unit vector of axis parallel to the flow direction measured.

$$\overrightarrow{f} = \left(\frac{\left(\overrightarrow{b}_1 \times \overrightarrow{b}_2\right) \times \overrightarrow{b}_2 + \left(\overrightarrow{b}_1 \times \overrightarrow{b}_2\right) \times \overrightarrow{b}_1}{|\left(\overrightarrow{b}_1 \times \overrightarrow{b}_2\right) \times \overrightarrow{b}_2 + \left(\overrightarrow{b}_1 \times \overrightarrow{b}_2\right) \times \overrightarrow{b}_1|}\right) \tag{5.7}$$

The parameters are used to determine fringe spacing and to correct for flow alignment of the probe. For the final alignment used in all SSWT measurements the beam angle was determined to be about 26.11 degree and is resulting in a fringe spacing of 1.1774 μm. The correction that has to be applied to the velocity vector for geometrical misalignment with the mean flow direction is 1.006.

To account for fringe gradient effects, an in-situ freestream calibration method is performed in order to determine the average virtual acceleration caused by the fringe gradient. For this purpose measurements in the potential flow with no acceleration present are made. For the freestream the Laser Doppler Acceleration equation eq. 4.6 simplifies to eq. 5.8. This is a valid assumption as there is assumed to be no acceleration so far downstream of the nozzle throat and upstream of the shock.

$$0 = v\, f\, \frac{dd_{fr}}{dx} + d_{fr}\, \frac{df}{dt} \tag{5.8}$$

Therefore the portion of this equation that will be a pure bias due to a fringe spacing gradient can be determined. This calibration is only dependent on chirp and frequency.

$$\frac{dd_{fr}}{dx} = -f^{-2}\, \frac{df}{dt} \tag{5.9}$$

This method's uncertainty greatly benefits from the high flow velocities in the supersonic facility. The high fringe gradient uncertainties are mainly a result of the chirp estimator

uncertainties. For low SNR the chirp estimator reaches up to 30 %, causing the main uncertainty of this type of calibration.

$$\Delta_{\frac{dd_{fr}}{dx}} = \sqrt{\left(f^{-3}\frac{df}{dt}\delta_f\right)^2 + \left(-f^{-2}\delta_{df/dt}\right)^2}$$

6 Experimental Results

Following types of seeding are used in the experiments: (1) DOP seeding using a Laskin nozzle seeder, (2) TiO_2 seeding using a cyclone seeder and (3) PSL seeding. The matrix of desired experiments is shown as table 13.

Case No	Material	Seeding device	nominal d[µm]	Regime
I	TiO_2	Cyclone Seeder	0.20	Subsonic transition flow
II	DOP	Laskin nozzle	0.60	Subsonic slip flow
III a	PSL	Spray nozzle, Seegmiller nozzle, Laskin nozzle, Ultrasonic nozzle	0.5	Subsonic slip flow
III b			0.83	Subsonic slip flow

Table 13: Test matrix

Dioctyl Phthalate (DOP) is a commonly used seeding approach for windtunnel applications. The DOP particle size is about 0.65 μm diameter, details on the measurements using a TSI particle sizer can be found in figure 24b on page 36. The particles are generated by a Laskin nozzle and dispersed in the flow through an angled hole in the windtunnel plenum. Despite its disadvantages the DOP seeding proved to be a robust seeding approach.

To introduce the Polystyrene Latex sphere, several common methods were tried, (a) an industrial spray nozzle type, (b) a custom made Seegmiller style nozzle, (c) an industrial spray nozzle connected to a heated pipe, (d) a Laskin nozzle and (e) an ultrasonic nozzle connected to a heated plenum.

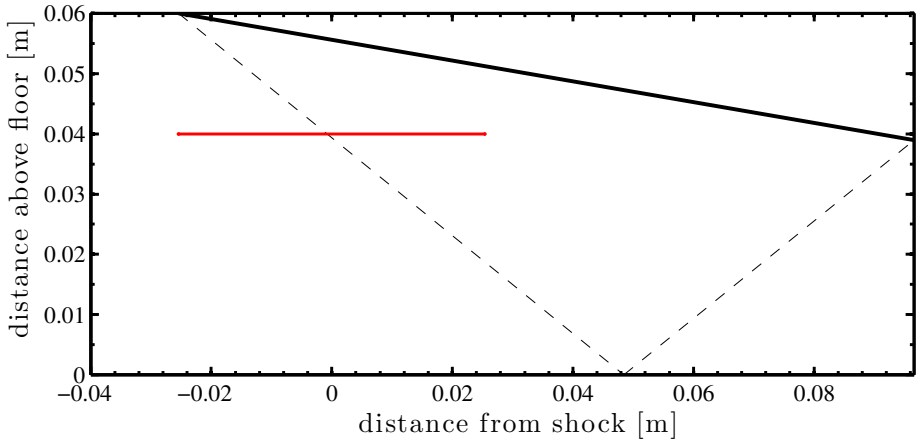

Figure 59: Measurement location/plane (red) relative to the 10 degree shock generator

All but the ultrasonic nozzle produced an unsatisfactory wet seed not usable for measurements, therefore all future references are on the Ultrasonic nozzle. More on PSL seeding in general and with respect to the SSWT application can be found in section 3.1.3 on page 31. The experiments were performed using the 15 degree shock generator with a -5 degree angle of attack resulting in an effective turning angle of 10 degrees.

6.1 Seeding Observations

As explained in detail in section 3.1.3 the evaporation of the carrier fluid is one of the most challenging and important to control parameters in a PSL seeding setup.

The moisture in the air flowing through a converging diverging nozzle in a supersonic windtunnel can cause the development of a condensation zone in the supersonic part. This condensation process does not only add the condensation heat to the flow [33]but also leads to nucleation of particles in the flow which can cause particle flow interaction and hinders optical measurements in the facility. In difference to low flow velocity expansion the condensation process after the isentropic expansion to the point where condensation temperature and pressure are reached does not follow the isentrope in a equilibrium condensation. Instead experiments show that the expansion process does not lead to condensation but to supercooling of the flow and therefore to a unstable supersaturated state. Sudden condensation is then triggered by homogeneous nucleation, which is dominating over any pre existent micro scale particle nuclei condensation according to Hill [38]. The homogeneous condensation proceeds with a time scale of the same order as a general chemical reaction rate and starts spontaneous when the necessary energy barrier is crossed [5]. However the small time scale in high speed flows does not allow for a sufficient big surface area of preexisting particles in the flow to be present and therefore cause heterogeneous condensation Hill [38].

When first measurements using PSL seeding revealed the presence of large particles in the flow, either non evaporated water droplets or recondensated ice and water particles a preliminary study with the pure alcohol/water mixture was undertaken. As the focus is on high SNR_1, number of samples in this table are given for bursts equal and higher than 20 dB.

It is observed that the impact of the carrier fluid on the amount of samples recorded is drastic. Reduction of fluid pressure decreases the amount of large fluid samples present, which in case of the freestream velocity (at x=-25.4 mm) leads to an increase in observed frequency (proportional to the fluid velocity). This might be to a slight lag after the parasitic shock, which can be seen on the Schlieren images in figure 50. Improvement can be observed by reducing the fluid pressure and increasing the Laser Power. However for no seeding

configuration complete evaporation could be reached with the Ultrasonic seeding nozzle at hand. Even at considerable distances from the shock significant particle lag is observed and separation into different particle sizes not easily possible. An exact correlation between particle velocity and signal amplitude could not be recognized. The use of a pure alcohol solution shows similar results (compare figure 60), indicating that no evaporation of the carrier fluid could be reached at the windtunnel conditions and PSL distribution methods at hand.

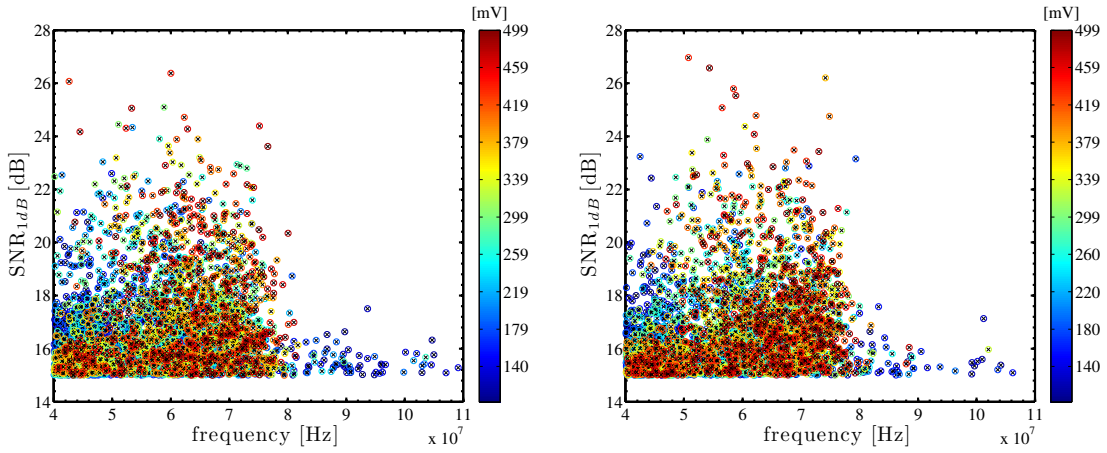

(a) PSL/Water/Alcohol mixture (b) pure Alcohol

Figure 60: Comparison of PSL mixture and pure Alcohol at x=0.0254 m after the shock

Interesting to note in all measurements performed is a sudden drop in number of samples close to the shock wave. There are two possible explanations for this effect: (1) the inhomogenity of the optical properties due to the three dimensionality of the shock or (2) agglomeration of seeding particles in the shear layer of boundary layer separation due to the shock. This effect is observed for all seeding approaches and independent of the evaporation and agglomeration effects. This phenomena comes along with a drop in Signal-to-Noise ratio.

6.2 Mean Velocity across the Shock

In this section the mean velocity of the particles across the shock are compared and conclusions about the state of the particles are drawn. From the experimental results displayed in figure 61a, it can be clearly seen that the Titanium Oxide seeding suffers greatly from agglomeration. The numerical curves displayed in this plot are for a 0.7 μm diameter particle and give an estimate on the agglomerated particle size being much larger than the nominal size of the powder particle. This observation is consistent with values reported e.g by Hum-

ble et al. [44]. Further literature and information on metal powder seeding can be found in section 3.1.1.

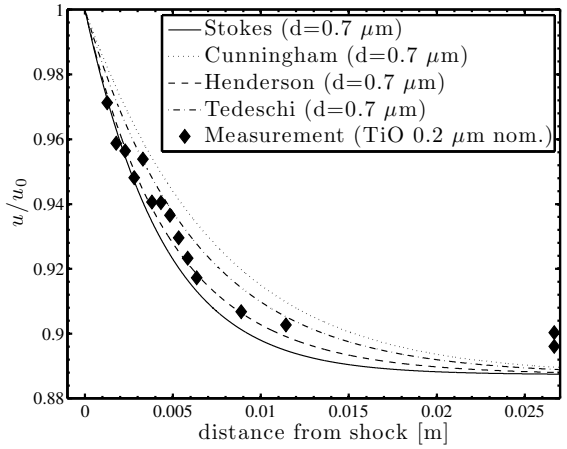

(a) Mean velocity profile of 0.2 nominal diameter μm TiO powder across a 10 degree turning angle shock

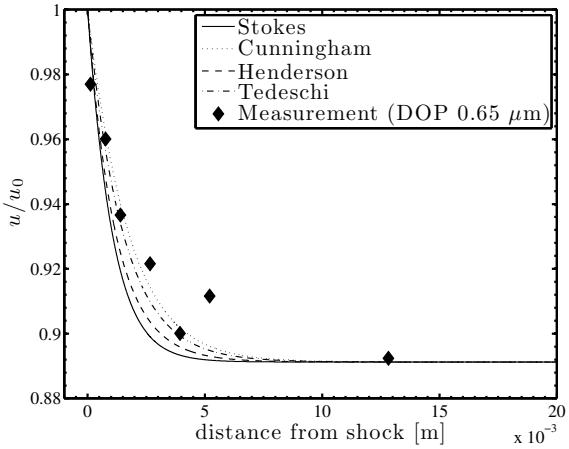

(b) Mean velocity profile of 0.65 μm DOP particles across a 10 degree turning angle shock

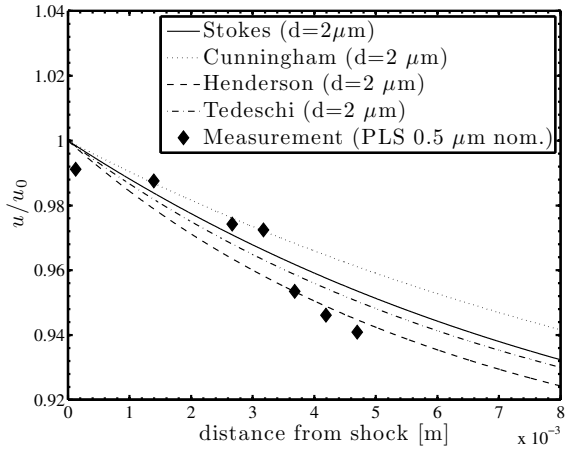

(c) Mean velocity profile of 0.5 nominal diameter μm PSL particle across a 10 degree turning angle shock

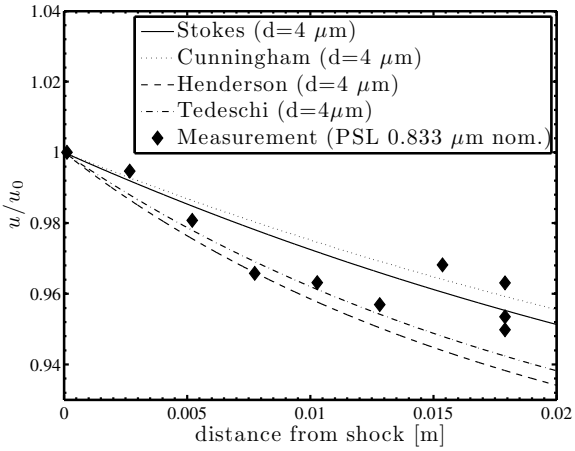

(d) Mean velocity profile of 0.833 μm PSL particles across a 10 degree turning angle shock

Figure 61: Mean velocity across the shock for different types of particles

The DOP particles generated with a 48 nozzle Laskin nozzle do not suffer from this drawback. Compared to particle size measurements obtained earlier in this facility (figure 24b) the DOP particles give coherent results. Comparison with numerical estimates give similar consistent results. The DOP particles have a much lower density than the metal particles and therefore a better dynamic response.

Even though the Ultrasonic nozzle seemed to perform much better than all previously

tried injection methods, the experimental investigation proved no evaporation of the carrier fluid for both Polystyrene Latex Sphere particle sizes. The velocity profile across the shock revealed huge micrometer sized particles. As concluded in the previous chapter this phenomena is caused by incomplete evaporation or even re-condensation after the nozzle throat. Using this seeding approach in a crucial experimental investigation would decrease its dynamic response by an order of magnitude at least (compare chapter 2.4). The numerical models displayed with this data is only an estimate for an average true particle size present in the flow. From figure 60 it can be seen that even at far distances from the shock particle lag is present. While high environmental temperatures (up to 40 C) and humidity (75-90%) during the windtunnel experiment might have contributed to this result, measurements without any seeding proved it to be a result to the seeding apparatus and the harsh supersonic windtunnel conditions.

Amplitude information did not allow separation of the different particles, but also model based velocity filtering would only result in biased data and not allow to extract transparent and usable information.

6.3 Particle Acceleration

6.3.1 Instantaneous Velocity and Acceleration

The unique spatial resolution allows to obtain instantaneous velocity as a function of time (the timeframe is of order of about two microseconds - which is about 1.5 mm in spatial extend) for high SNR bursts.

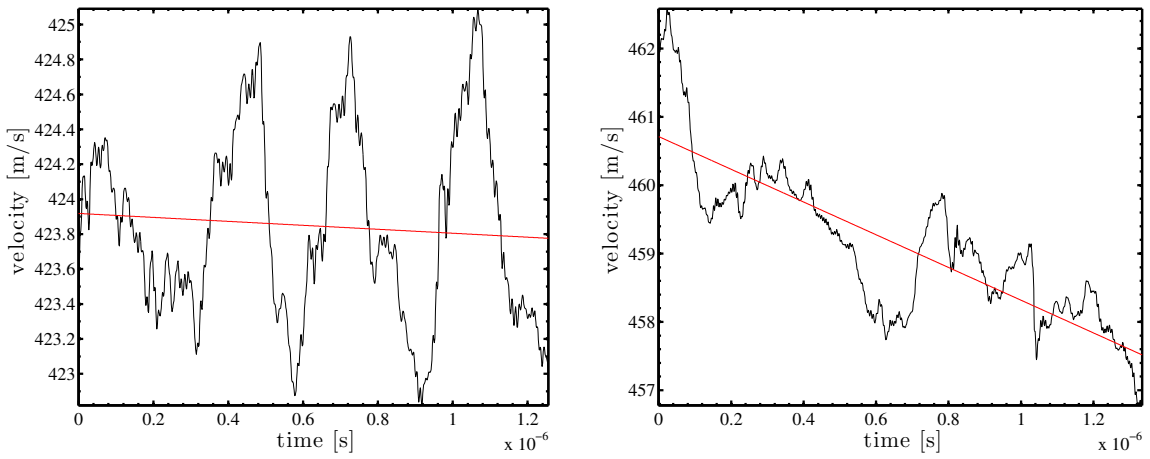

(a) Downstream particle trace

(b) Trace after the shock at x=0.002 m

Figure 62: Single measurements

The sliding FFT technique proves to be more robust at low SNR whereas the QDT technique is very sensitive to noise - also due to the differentiation process involved. Additionally the nonlinearity increases the difficulty of the phase recovery and therefore of the estimation process.

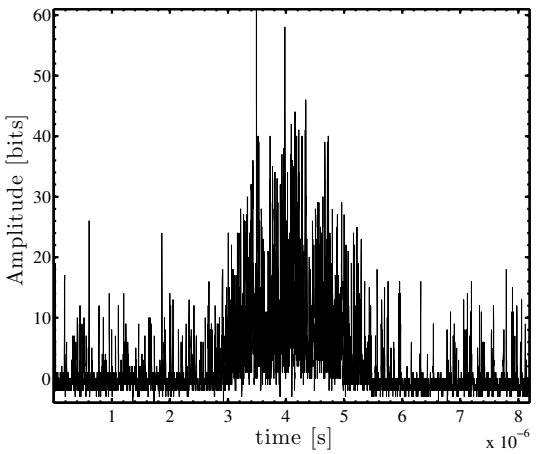

(a) SNR_{1db} = 20dB burst

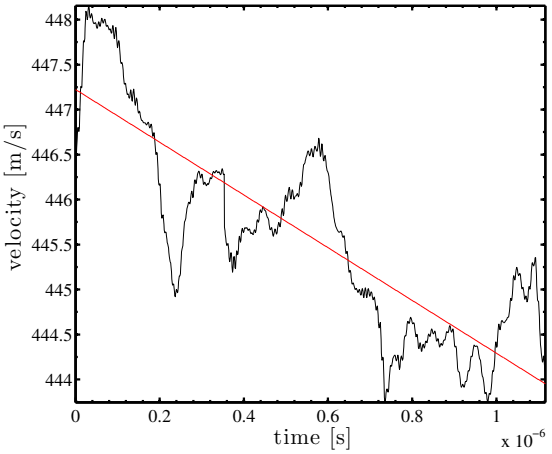

(b) frequency chirp

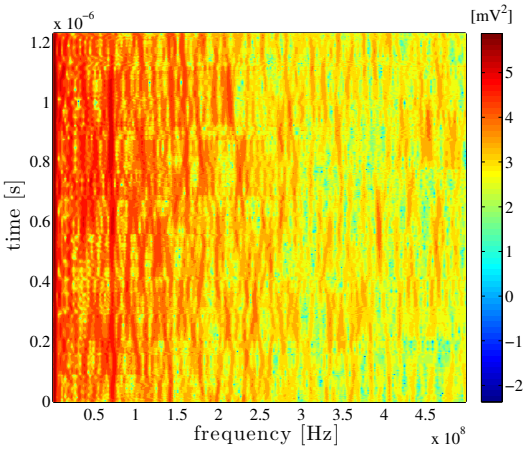

(c) Spectrogram

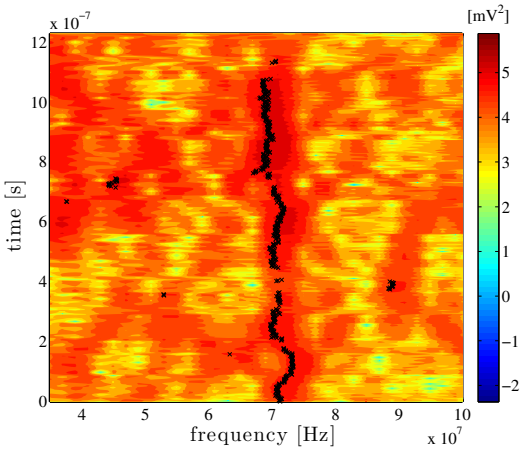

(d) Spectrogram (Detail) with max power indication

Figure 63: Instantaneous burst properties (Sliding FFT) of a DOP trace at x=0.003 m after the shock

In figure 63 an example for one particle trace downstream of the shock is given. Both a Spectrogram and a Sliding FFT plot of the particle velocity as a function of time are given. Interesting to note is a periodic velocity change which cannot be attributed to numerical uncertainties as they are estimated to be less than 1 %[23] for one point in a burst and less

[23] Assuming SNR of 22 db and above, the sliding FFT while effectively reducing the bandwidth dependent

than 20 % for a complete burst with Gaussian shape and noise distribution.

6.3.2 Mean Acceleration

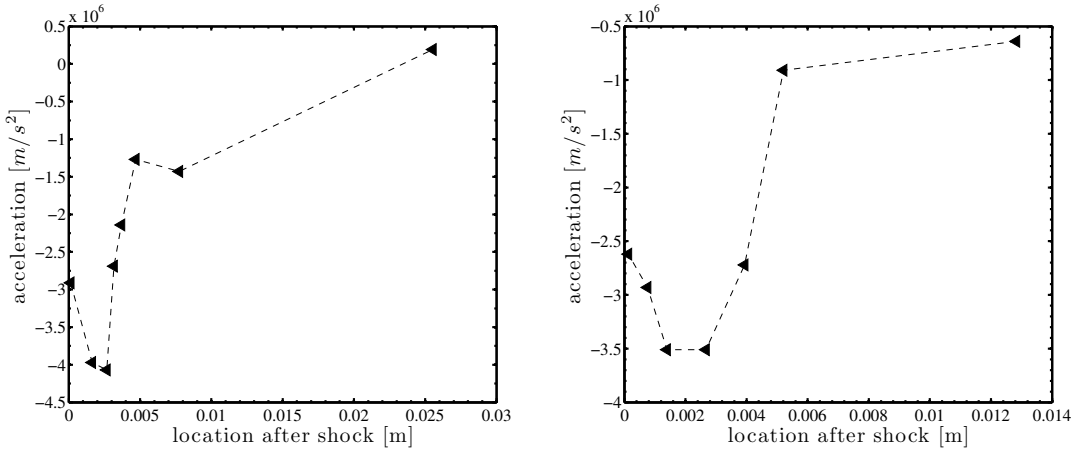

(a) Mean acceleration profile of 0.2 (nominal) μm TiO_2 particles (estimated to be have a aerodynamic diameter of about 0.7 μm) across a 10 degree turning angle shock

(b) Mean acceleration profile of 0.65 μm DOP particles across a 10 degree turning angle shock

Figure 64: Mean acceleration for TiO_2 and DOP particles across the shock

The mean acceleration of the particle flow in the vicinity of the shock is determined by averaging the mean acceleration obtained from the sliding FFT for all bursts at a certain location. Figure 64 displays the mean acceleration for TiO_2 and DOP particles. It is observed that the deceleration first increases and then decreases, this is consistent with the physical phenomena present. Simple one dimensional models that assume the shock to be similar to a step function do not show this behavior as they assume the shock to be infinitely small, whereas in truth the shock has a thickness of several mean free paths, so that the fluid first has to decelerate from the equilibrium condition in front of the shock and then finally accelerate to reach equilibrium conditions after the shock. High uncertainties are mainly due to chirp estimator uncertainties and in the range of about 28%.

SNR still maintains a frequency estimator uncertainty of about 1 %

7 Conclusions

In this thesis a fundamental investigation of particle dynamics with respect to windtunnel application and non continuum effects is carried out. The theoretical basics are described and applied to computationally describe particle lag effects across a shock wave. Available data in the literature is analyzed using simple one dimensional models as well as CFD implementations. It crystallized that a improved data basis on drag measurements in slip and transition flow regimes is required to successfully evaluate the drag models available. Such measurements can be provided by the application of a novel Laser Doppler Accelerometry probe. It is shown that non continuum effects can have a significant effect on the required particle sizes for turbulence measurements. Even though none of the present models is perfect in prediction of the drag coefficient in all regimes for all situations, they are more reliable than the Stokes model typically used. The common practice to assume Stokes flow as done for the case of subsonic continuum flow is not valid for application in supersonic windtunnels and should therefore not be used as a tool to determine cut off frequencies or particle parameters. The presented analysis, based on the work done by Melling [66] and Tedeschi et al. [94, 95] gives a more justified tool for the practical determination of particle tracking requirements in trans and subsonic windtunnels. It can be concluded that well directed heating of the windtunnel flow might reduce slip effects around the particles which leads to higher cut off frequencies for turbulence measurements.

Available seeding methods for particle based measurement methods are reviewed in detail and supplemented with relevant references of experimental application. Three different types of particles (TiO_2,DOP and PSL) , four different particle sizes and many different ways of flow injection were tested. Intensive application shows that experience from subsonic facilities cannot simply be transferred to a supersonic windtunnel.

A nonlinear Laser Doppler burst model is introduced to analyze currently used estimation techniques and processing uncertainty as well as to support creation of all data processing codes needed for experimental data. The Cramer Rao Lower Bound (CRLB) of the model signal is numerically approximated. The Quadrature Demodulation Technique (QDT) and the Sliding FFT technique are investigated for signal processing and their estimation uncertainty compared to the CRLB. Both methods come close to the CRLB for frequency estimation for high SNR_1, but fail to reach the CRLB for chirp estimation. The Sliding FFT proved to be more robust for measured signals. The estimation uncertainty is estimated to be about 0.2 %[24] for velocity, but up to 28 % for accelerations.

[24] unbiased error, bias error is about 2%

To conclude the investigation, a novel 1 component Laser Doppler sensor is proposed, built and applied to particle lag experiments in the super sonic facility. This sensor uses cylindrical lenses to create a measurement volume with an unique spatial width and resolution in order to allow particle velocity and acceleration measurements. Three different types of particles with four different sizes are experimentally investigated in more than 150 windtunnel runs. The experimental data provides mean velocity as a function of distance from the shock and reveals significant agglomeration and evaporation problems with Titanium Oxide and Polystyrene Latex spheres. These problems greatly influence mean velocity, turbulence spectral as well as stress statistics of any experimental investigation these particles are used for and therefore are an issue one has to account for. Additionally, particle acceleration measurements are presented, proving the unique concept of the new Laser Doppler probe. Mean and instantaneous accleration data is extracted from high SNR signals. The high SNR requirement and sample size constraints due to windtunnel runtime reduce the available data compared to regular velocity measurements. Acceleration uncertainties are as expected very high for low SNR and in the range up to 28%. This is mainly due to high chirp estimator uncertainty and the insitu calibration. For high SNR or an improved calibration process these uncertainties can be much lower. The acceleration data obtained is consistent in magnitude and trend with the pysical phenomena expected and shows the feasability of the new instrument.

References

[1] Department of aerospace and ocean engineering, virginia tech. URL www.aoe.vt.edu.

[2] Wikipedia, public domain. URL http://en.wikipedia.org/wiki/File:ObliqueShockAngleRelation.png.

[3] *ANSYS FLUENT 12.0/12.1 User Documentation*, 2010.

[4] H. E. Albrecht, M. Borys, N. Damaschke, and C. Tropea. *Laser Doppler and Phase Doppler Measurement Techniques*. Springer, 1 edition, December 2002.

[5] S.-C. Baek, S.-B. Kwon, T. Setoguehi, T. Setoguehi, and H.-D. Kim. Time-dependent characteristics of the nonequilibrium condensation in subsonic flows. *KSME International Journal*, 16(11):1511–1521, 2002.

[6] A. B. Bailey. Sphere drag coefficient for subsonic speeds in continuum and free-molecule flows. *Journal of Fluid Mechanics*, 65(02):401–410, 1974.

[7] A. B. Bailey and J. Hiatt. Free-flight measurements of sphere drag at subsonic, transonic, supersonic, and hypersonic speeds for continuum, transition, and near-free-molecular flow condition. Technical report, Arnodl Engineering Developement Center (AEDC), 1970.

[8] R. W. Barber and D. R. Emerson. Analytical solution of low reynolds number slip flow past a sphere. *Council for the Central Laboratory of the Research Councils, DL-TR-2000-001 (2000)*, 2000.

[9] C. Bayer, K. Shirai, L. Büttner, and J. Czarske. Measurement of acceleration and multiple velocity components using a laser doppler velocity profile sensor. *Measurement Science and Technology*, 19, 2007.

[10] R. N. Berglund and B. Y. H. Liu. Generation of monodisperse aerosol standards. *Environ. Sci. Technol.*, 7(2), 1973.

[11] R. Budwig. Refractive index matching methods for liquid flow investigations. *Experiments in Fluids*, 17:350–355, 1994. ISSN 0723-4864. 10.1007/BF01874416.

[12] G. Byun, R. L. Simpson, T. Ecker, and K. T. Lowe. Flow structure of supersonic rough wall turbulent boundary layers. In *AFOSR Meeting*, July 2010.

[13] B. T. Chao. Turbulent transport behaviour of small particles in dilute suspension. *Österreichisches Ingenieur-Archiv.*, pages p.7–21, 1964.

[14] C. J. Chesnakas. *Experimental Studies in a Supersonic Through-Flow Fan Blade Cascade*. PhD thesis, Virginia Polytechnic Institute and State University, 1991.

[15] C. J. Chesnakas and W. F. Ng. Supersonic through-flow fan blade cascade studies. *Journal of Fluids Engineering*, 125(5):796–805, 2003.

[16] C. T. Crowe. *Multiphase Flow Handbook*. CRC - Taylor and Francis, 2005.

[17] C. T. Crowe, J. A. Nicholls, and R. B. Morrison. Drag coefficients of inert and burning particles accelerating in gas streams. *Symposium (International) on Combustion*, 9(1): 395 – 406, 1963. ISSN 0082-0784.

[18] C. T. Crowe, W. R. Babcock, P. G. Willoughby, and R. L. Carlson;. Measurement of particle drag coefficients in flow regimes encountered by particles in a rocket nozzle. Technical report, Ft. Belvoir : Defense Technical Information Center, 1968.

[19] E. Cunningham. On the velocity of steady fall of spherical particles through fluid medium. *Proceedings of the Royal Society of London. Series A, Containing Papers of a Mathematical and Physical Character*, 83(563):357–365, 1910.

[20] J. W. Czarske. Statistical frequency measuring error of the quadrature demodulation technique for noisy single-tone pulse signals. *Measurement Science and Technology*, 12 (5), 2001.

[21] J. W. Czarske, F. Hock, and H. Mueller. Quadrature demodulation: a new ldv burst-signal frequency estimator. volume 2052, pages 79–86, Koningshof, Veldhoven, Netherlands, August 1993. SPIE.

[22] J. W. Czarske, L. Buettner, T. Razik, and H. Welling. Measurement of velocity gradients in boundary layers by a spatially resolving laser doppler sensor. In C. R. Mercer, S. S. Cha, and G. Shen, editors, *Optical Diagnostics for Fluids, Solids, and Combustion*, volume 4448, pages 60–71, San Diego, CA, USA, 11 2001. SPIE.

[23] C. J. DeLapp and M. F. Reeder. Clean seeding material for particle image velocimetry measurements. *25th AIAA Aerodynamic Measurement Technology and Ground Testing Conference*, 2006.

[24] R. E. DeOtte, G. L. Morrison, D. L. Panak, and G. H. Nail. 3-d laser doppler anemometry measurements of the axisymmetric flow field near an orifice plate. *Flow Meas. Instrum.*, 2:115–123, April 1991.

[25] C. Devals, G. Jourdan, J.-L. Estivalezes, E. Meshkov, and L. Houas. Shock tube spherical particle accelerating study for drag coefficient determination. *Shock Waves*, 12:325–331, 2003. ISSN 0938-1287. 10.1007/s00193-002-0172-z.

[26] E. Doebelin. *Measurement systems: application and design*. McGraw-Hill series in mechanical and industrial engineering. McGraw-Hill, 2004. ISBN 9780072438864.

[27] D. Durox, S. Ducruix, and F. Lacas. Flow seeding with an air nebulizer. *Experiements in Fluids*, 1999.

[28] F. Durst, A. Melling, and J. H. Whitelaw. *Principles and Practice Laser-Doppler Anemomtry*. Academic Press, 1981.

[29] W. H. Echols and J. A. Young. Studies of portable air operated aerosol generators [nrf report 5929]. Technical report, Naval Research Laboratory, 1963.

[30] T. Ecker, J. Wehrstedt, and R. Simpson. Modeling of particle response through an oblique shock. In *8th FZD and Ansys Short Course and Workshop on Multiphase Flows: Simulation, Experiment and Application*. Forschungszentrum Rossendorf & ANSYS Germany, June 2010.

[31] U. Fey, R. Konrath, T. Kirmse, T. Ahlefeldt, J. Kompenhans, and Y. Egami. Advanced measurement techniques for high reynolds number testing in cryogenic wind tunnels. *48th AIAA Aerospace Sciences Meeting Including the New Horizons Forum and Aerospace Exposition*, 2010.

[32] F.L.Crosswy. Particle size distribution of several commonly used seeding aerosols. *Wind Tunnel Seeding Systems for Laser Velocimeters, NASA Workshop*, 1985.

[33] W. Frank. Condensation phenomena in supersonic nozzles. *ACTA Mechanica, Springer Verlag*, 54:135–156, 1985.

[34] U. Ghi, S. Bayyuk, S. Habch, C. Roy, T. Shi, T. Conlis, C. Hirsch, and J. M. Power. The aiaa code verification project - test cases for cfd code verification. *AIAA-2010-125 48th AIAA Aerospace Sciences Meeting Including the New Horizons Forum and Aerospace Exposition, Orlando, Florida*, Jan 2010.

[35] R. Granger. *Fluid Mechanics*. Dover Publications, 1985.

[36] M. Havermann, J. Haertig, C. Rey, and A. George. Application of particle image velocimetry to high-speed supersonic flows in a shock tunnel. In *11th International Symposium on Application of Laser Techiques to Fluid Mechanics*, 2002.

[37] C. B. Henderson. Drag coefficients of spheres in continuum and rarefied flows. *AIAA Journal*, 14(6), June 1976.

[38] P. G. Hill. Condensation of water vapour during supersonic expansion in nozzles. *J. Fluid Mech.*, 25(25):593–620, 1966.

[39] A. Hjelmfelt and L. Mockros. Motion of discrete particles in a turbulent fluid. *Applied Scientific Research*, 16:149–161, 1966. ISSN 0003-6994. 10.1007/BF00384062.

[40] A. Hoelzer and M. Sommerfeldh. New simple correlation formula for the drag coefficient of non-spherical particles. *Powder Technology*, 184(3):361–365, June 2008.

[41] A. Hopkins. *Fluid Dynamics and Surface Pressure Fluctuations of Two-Dimensional Turbulent Boundary Layers Over Densely Distributed Surface Roughness*. Phd dissertation, Virginia Polytechnic Institute and State University, 2010.

[42] N. E. Huang and N. O. Attoh-Okine. *The Hilbert-Huang Transform in Engineering*. CRC - Taylor and Francis, 2005.

[43] R. Humble, F. Scarano, B. van Oudheusden, and M. Tuinstra. Piv measurements of a shock wave/turbulent boundary layer interaction. *3th Int. Symp. on Applications of Laser Techniques to Fluid Mechanics Lisbon, Portugal,*, 2006.

[44] R. Humble, F. Scarano, and B. van Oudheusden. Particle image velocimetry measurements of a shock wave/turbulent boundary layer interaction. *Experiments in Fluids*, 43:173–183, 2007. ISSN 0723-4864. 10.1007/s00348-007-0337-8.

[45] O. Igra and K. Takayama. Shock tube study of the drag coefficient of a sphere in a non-stationary flow. *Proceedings: Mathematical and Physical Sciences*, 442(1915):pp. 231–247, 1993. ISSN 09628444.

[46] D. A. Japuntich, J. I. T. Stenhouse, and B. Y. H. Liu. Conditions for monodispersity of heterogeneous condensation aerosols using dimensionless groups. *Journal of Colloid and Interface Science*, 136(2):393 – 400, 1990. ISSN 0021-9797.

[47] S. Jennings. The mean free path in air. *Journal of Aerosol Science*, 19(2), 1988.

[48] J.Lepicovsky and R.J.Bruckner. Seeding for laser velocimetry in confined supersonic flows with shocks. NASA Technical Memorandum 107265, NASA, 1996.

[49] Z. Jun, G. Zhenghong, Z. Hao, and B. Junqiang. A high-speed nature laminar flow airfoil and its experimental study in wind tunnel with nonintrusive measurement technique. *Chinese Journal of Aeronautics*, 22(3):225 – 229, 2009. ISSN 1000-9361.

[50] R. D. Keane and R. J. Adrian. Optimization of particle image velocimeters. i. double pulsed systems. *Meas. Sci. Technol*, 1:1202–1215, 1990.

[51] M. J. Kenney, R. J. Sarjant, and M. W. Thring. The viscosity of mixtures of gases at high temperatures. *British Journal of Applied Physics*, 1956.

[52] J. Kestin and J. Whitelaw. The viscosity of dry and humid air. *International Journal of Heat and Mass Transfer*, 7(11):1245 – 1255, 1964. ISSN 0017-9310.

[53] J. H. Kim, G. W. Mulholland, S. R. Kukuck, and D. Y. H. Pui. Slip correction measurements of certified psl nanoparticles using a nanometer differential mobility analyzer (nano-dma) for knudsen number from 0.5 to 83. *Journal of Research of the National Institute of Standards and Technology*, 10(1), 2005.

[54] M. Klaas, W. Schroeder, and W. Althaus. Experimental investigation of slender streamwise vortices and oblique shock–vortex interaction. *35th AIAA Fluid Dynamics Conference and Exhibit*, 2005.

[55] C. Köhler, B. Sammler, and J. Kompenhans. Generation and control of tracer particles for optical flow investigations in air. *Experiments in Fluids*, 33, 2002.

[56] L. Lading and K. Andersen. Estimating frequency and phase for velocity and size measurements [laser anemometry]. In *International Congress on Instrumentation in Aerospace Simulation Facilities*, pages 274 –290, September 1989. doi: 10.1109/ICIASF.1989.77681.

[57] B. Lehmann, H. Nobach, and C. Tropea. Measurement of acceleration using the laser doppler technique. *Measurement Science and Technology*, 13(9):1367, 2002.

[58] J. Lepicovsky, E. Braunscheidel, R. Bruckner, and D. Tweedt. Laser velocimeter measurements of axial velocity filed in the nasa supersonic fan rotor. In *Proceedings of*

ASME Turbo Expo 2001: Land, Sea and AIr, New Orleans, Louisiana, USA, June 2001. ASME.

[59] C.-T. Li, K.-C. Chang, and M.-R. Wang. Piv measurements of turbulent flow in planar mixing layer. *Experimental Thermal and Fluid Science*, 33:527–537, 2008.

[60] J. Loschmidt. On the size of the air molecules. *Journal of Chemical Education*, 72(10): 870, 1995.

[61] K. T. Lowe. *Design and application of a novel Laser-Doppler Velocimeter for turbulence structural measurements in turbulent boundary layers*. Phd dissertation, Virginia Polytechnic Institute and State University, 2006.

[62] K. T. Lowe and R. L. Simpson. Measurements of velocity-acceleration statistics in turbulent boundary layers. *International Journal of Heat and Fluid Flow*, 27(4):558 – 565, 2006. ISSN 0142-727X. Special Issue of The Fourth International Symposium on Turbulence and Shear Flow Phenomena - 2005.

[63] K. Martin. Complex signal processing is not complex. *Circuits and Systems I: Regular Papers, IEEE Transactions on*, 51(9):1823 – 1836, September 2004. doi: 10.1109/TCSI.2004.834522.

[64] T. Maxworthy. Accurate measurements of sphere drag at low reynolds numbers. *Journal of Fluid Mechanics*, 23:369–372, 1965.

[65] M. K. Mazumder, B. D. Hoyle, and K. J. Kirsch. Fluid dynamic studies on scattering aerosol and its generation for application as tracer particles in supersonic flow measurements utilizing laser doppler velocimeter. Technical report, Nasa, 1974.

[66] A. Melling. Tracer particles and seeding for particle image velocimetry. *Meas. Sci. Technol.*, 1997.

[67] J. F. Meyers. Generation of particles and seeding. Technical report, Generation of Particles and Seeding, 1991.

[68] E. E. Michaelides. Hydrodynamic force and heat/mass transfer from particles, bubbles, and drops - the freeman scholar lecture. *Journal of Fluids Engineering*, 125:209–238, 2003.

[69] H. Mueller, V. Strunck, and D. Dopheide. The application of quadrature demodulation techniques for the investigation of flows. *Flow Measurement and Instrumentation*, 7 (3-4), 1996.

[70] H. L. Nichols. Calculation of particle dynamics effects on laser doppler velocimetry. *Wind Tunnel Seeding Systems for Laser Velocimeters, NASA Workshop*, 1985.

[71] H. Nobach, M. Kinzel, R. Zimmermann, C. Tropea, and E. Bodenschatz. Measurement of particle accelerations with the laser doppler technique. In M. Deville, T.-H. Lê, and P. Sagaut, editors, *Turbulence and Interactions*, volume 110 of *Notes on Numerical Fluid Mechanics and Multidisciplinary Design*, pages 271–278. Springer Berlin / Heidelberg, 2010.

[72] H. Oertle. *Stroemungsmechanik*. 4 edition, 1999.

[73] F. Onofri, T. Girasole, G. Gréhan, G. Gouesbet, G. Brenn, J. Domnick, T.-H. Xu, and C. Tropea. Phase-doppler anemometry with the dual burst technique for measurement of refractive index and absorption coefficient simultaneously with size and velocity. *Particle and Particle Systems Characterization*, 13(2):112–124, 1996. ISSN 1521-4117. doi: 10.1002/ppsc.19960130209.

[74] W. P. Patrick and R. W. Paterson. Seeding technique for laser doppler velocimetry in measurements in strongly accelerated nozzle flowfields. In *AIAA 14th Fluid and Plasma Dynamics Conference*, Palo Alto, CA, June 1981.

[75] W. Pilacinski, K. W. Szewczyk, M. Lehtimaeki, and K. Willeke. Characteristics of a double-orifice nebulizer. *Journal of Aerosol Science*, 21(7):977 – 982, 1990. ISSN 0021-8502.

[76] J. Poggie, P. J. Erbland, A. J. Smits, and R. B. Miles. Quantitative visualization of compressible turbulent shear flows using condensate-enhanced rayleigh scattering. *Experiments in Fluids*, 37:438–454, 2004. ISSN 0723-4864. 10.1007/s00348-004-0828-9.

[77] A. K. Prasad. Particle image velocimetry. *Current Science*, 70(1):51–60, July 2000.

[78] D. Rabe and K. Sabroske. Laskin nozzle performance for laser flow measurement seeding. *32nd Aerospace Sciences Meeting & Exhibit*, 1994.

[79] D. C. Rabe and C. L. Dancey. Comparison of laser transit and laser doppler anemometer measurements in fundamental flows. *AIAA/ASME/SAE/ASEE 22nd Joint Propulsion Conference*, 1986.

[80] D. Ragni, F. Schrijer, B. van Oudheusden, and F. Scarano. Particle tracer response across shocks measured by piv. *Experiments in Fluids*, pages 1–12, 2010. ISSN 0723-4864. 10.1007/s00348-010-0892-2.

[81] M. F. Reeder, J. W. Crafton, J. Estevadeordan, J. DeLapp, C. McNiel, D. Peltier, and T. Reynolds. Clean seeding for flow visualization and velocimetry measurements. *Experiements in Fluids*, 2009.

[82] C. Roth, J. Gebhart, and W. Reisert. The production of high-concentrated monodisperse aerosols with variable size distributions. *Journal of Aerosol Science*, 23:185–188, 1992.

[83] K. R. Sabroske. Seeding materials for use in laser anemometry. In *31 st Aerospace Sciences Meeting & Exhibit*, number AIAA 93-0006, Reno, NV, January 1993.

[84] F. Scarano. *Overview of PIV in Supersonic Flows*. Springer, 2008. Fulvio Scarano.

[85] F. Scarano and B. W. van Oudheusden. Planar velocity measurements of a two-dimensional compressible wake. *Experiments in Fluids*, 34:430–441, 2003. ISSN 0723-4864. 10.1007/s00348-002-0581-x.

[86] S. A. Schaaf and P. L. Chambre. *Flow of rarefied gases*. Princeton: Princeton University Press, princeton aeronautical paperbacks. edition, 1961.

[87] H. L. Seegmiller. Seeding subsonic transonic and supersonic flows with 0.5 micron polystrene spheres. *Wind Tunnel Seeding Systems for Laser Velocimeters, NASA Workshop*, 1985.

[88] H. L. Seegmiller, J. G. Marvin, and L. L. Levy. Steady and unsteady transonic flow. *AIAA 16th Aerospace Sciences Meeting*, 16, 1978.

[89] K. A. Shinpaugh, R. L. Simpson, A. L. Wicks, S. M. Ha, and J. L. Fleming. Signal-processing techniques for low signal-to-noise ratio laser doppler velocimetry signals. *Experiments in Fluids*, 12:319–328, 1992. ISSN 0723-4864. doi: 10.1007/BF00187310.

[90] M. Smith, A. Smits, and R. Miles. Compressible boundary-layer density cross sections by uv rayleigh scattering. *Optics Letters*, 14:916–919, 1989.

[91] P. R. Spalart and S. R. Allmaras. A one-equation turbulence model for aerodynamic flows. *AIAA Paper 92-0439*, 1992.

[92] Staff. Naca 1135 - equations, tables and charts for compressible flow. Technical report, NACA, 1953.

[93] H. K. Tanna and P. J. Morris. In-flight simulation experiments on turbulent jet mixing noise. *Journal of Sound and Vibration*, 53, 1977.

[94] G. Tedeschi, M. Elena, and H. Gouin. Particle motion through an oblique shock wave. *Proc. SPIE*, 2052, 273:273–278, 1993.

[95] G. Tedeschi, H. Gouin, and M. Elena. Motion of tracer particles in supersonic flows. *Experiments in Fluids*, 26:288–296, June 1999.

[96] M. Tillery, G. Wood, and H. J. Ettinger. Generation and characterization of aerosols and vapors for inhalation experiments. *Environmental Health Perspectives*, 16:25–40, 1976.

[97] C. Tropea, A. Yarin, and J. Foss, editors. *Springer Handbook of Experimental Fluid Mechanic*. Springer Verlag Berlin-Heidelberg, 2007.

[98] TSI. Tsi - seed particles for ldv and piv. online.

[99] W. D. Urban and M. G. Mungal. Planar velocity measurements in compressible mixing layers. *35th Aerospace Sciences Meeting, Reno, NV*, 1997.

[100] W. D. Urban and M. G. Mungal. Planar velocity measurements in compressible mixing layers. *Journal of Fluid Mechanics*, 431(-1):189–222, 2001.

[101] M. Vlajinac and E. E. Covert. Sting-free measurements of sphere drag in laminar flow. *Journal of Fluid Mechanics*, 54:385–392, 1972.

[102] M. J. Walsh. Drag coefficient equations for small particles in high speed flows. *AIAA Journal*, 13:1526–1528, Nov. 1975.

[103] M. J. Walsh. Influence of particle drag coefficient on particle motion in high-speed flow with typical laser velocimeter applications. Technical Report L-10258; NASA-TN-D-8120, NASA Langley Research Center, Feb 1976.

[104] C. A. Wasserbauer and M. D. Hathaway. Development of the seeding system used for laser velocimeter surveys of the nasa low-speed centrifugal compressor flow field. *18th AlAA Aerospace Ground Testing Conference*, 1994.

[105] P. P. Wegener and H. Ashkenas. Wind tunnel measurements of sphere drag at supersonic speeds and low reynolds numbers. *Journal of Fluid Mechanics*, 10:550–560, 1961.

[106] M. P. Wernet, M. M. Bright, and G. J. Skoch. An investigation of surge in a high-speed centrifugal compressor using digital piv. *Journal of Turbomachinery*, 123(2):418–428, 04 2001.

[107] W. H. Whitlock, W. R. Weltmer, and J. Clark. Apparatus and method for removing minute particles from a substrate. *US Patent 4,806,171*, 1989.

[108] C. Willert, M. Raffel, J. Kompenhans, B. Stasicki, and C. Koehler. Recent applications of particle image velocimetry in aerodynamic research. *Flow Measurement and Instrumentation*, 7(3-4):247 – 256, 1996. ISSN 0955-5986. Optical Methods in Flow Measurement.

Appendix A User Defined Function Fluent

Algorithm 1 User Defined Function for Fluent - Henderson Drag Law

```
/**********************************************************************
UDF for computing particle drag coefficient Henderson 1.0
based on Charles B. Henderson,Drag Coefficients of Spheres in Continuum
and Rarefied Flows, AIAA Journal, 1976
kappa and R still need to be extracted from fluent
**********************************************************************/
#include "udf.h"
#include "math.h"
#include "dpm.h"
DEFINE_DPM_DRAG(particle_drag_force,Re,p)
{
/* get the current cell tand thread the particle is in */ c
ell_t c = RP_CELL(&((p)->cCell));
Thread *t = RP_THREAD(&((p)->cCell));
/* Define variables*/
real drag_force, M, T, Tw, mu, roh, d, u_rel, a, R, kappa, C_D, S; R=287;
/* get cell and particle values */
T=C_ T(c, t);
Tw=P_ T(p);
d=P_DIAM(p);
roh=C_R(c, t);
mu=C_MU_L(c, t);
u_rel=Re*mu/(d*roh);
a=(1.4*R*T);
/* calculate Mach number */
M=u_rel/a;
/* Calculate molecular speed ratio */
S=u_rel/powf((2*R*T),0.5);
/* Calculate drag coefficent */
C_D=24*powf((Re+S*(4. 33+((3. 65-1. 53* Tw/ T)/(1+0. 353* Tw/ T))
*exp(-0. 247*Re/S))), -1)+exp(-0. 5*M/powf(Re, 0. 5))*((4. 5+0. 38
*(0. 03*Re+0. 48*powf(Re, 0. 5)))/(1+0. 03*Re+0. 48*powf(Re, 0. 5))
+0. 1*powf(M, 2)+0. 2*powf (M, 8))+(1-exp(-M/Re))*0. 6*S;
drag_force=18 * C_D * Re / 24;
return (drag_force);
```